On the stability of the gravity-driven viscous channel flow

Von der Fakultät für Ingenieurwissenschaften
der Universität Bayreuth
zur Erlangung der Würde eines
Doktor-Ingenieur (Dr.-Ing.)
genehmigte Dissertation

von

Armin Georg Kögel, M.Sc.

aus

Schongau

Erstgutachter:	Prof. Dr. N. Aksel
Zweitgutachter:	Prof. Dr. A. Wierschem
Tag der mündlichen Prüfung:	6. August 2020

Lehrstuhl für Technische Mechanik und Strömungsmechanik
Universität Bayreuth
2020

Abstract

Gravity-driven viscous film flow is a classic problem in fluid mechanics. It represents a simplified model for a variety of technical and natural systems. In the simplest example, the plane film flow over an inclined plane of infinite extent, both the stationary solution—known as *Nusselt flow*—and the primary instability can be determined by simple means from the Navier–Stokes equations.

The Nusselt flow with its parabolic velocity profile offers a good estimate of flow behavior in real systems, i.e. it is possible to predict both the stationary flow and its instability. The latter is often of great interest, particularly for technical systems, since surface waves caused by the instability are usually undesirable. A prominent example are coating processes that require a film of constant thickness.

Research on film flows has surpassed these simple model in recent decades for two main reasons:

1) Simplified models are not sophisticated enough to represent real systems. The surfaces in technical and natural systems are often not perfectly smooth but rough, either accidentally or intentionally. In addition, a real flow cannot be infinitely extended. It must be limited, for example, by side walls. To describe these complex multidimensional flows, refined models and further experimental investigations are necessary.

2) Since particularly for many technical systems the formation of surface waves should be suppressed, control of the primary instability is crucial. This can be achieved by varying the substrate, but also by appropriate use of sidewall effects.

This thesis deals mainly with the influence of side walls on film flows over flat surfaces, i.e. the difference between channel flow and plane film flow. For this purpose, the stationary flow, the primary instability and the shape of the resulting waves were investigated with different experimental methods and compared with the numerically obtained results for the plane film flow.

In a first step, the equations needed to calculate the primary instability of the plane film flow—namingly the Orr–Sommerfeld equation and the corresponding boundary conditions—are derived. These equations can only be solved analytically in the limit of very long waves, but with numerical methods the whole parameter space is accessible.

Furthermore, it must be ensured that all measurements of steady-state flow and stability are not influenced by inflow effects of the channel. For this purpose, the inflow area was characterized by the measurement of the film thickness and surface velocity along the channel. The measurement

positions for all further measurements were chosen in such a way that all inflow effects have decayed to this point.

It will be shown that side walls have a stabilizing effect on film flow and the stabilization increases significantly with decreasing channel width. This can be explained by the influence of side walls on the stationary flow: In close vicinity of the sidewalls the flow is slowed down. In this "disturbed" area, surface waves are damped and the flow is thus stabilized. The narrower the channel, the greater the percentage of the fluid disturbed by the side walls and thus the stronger the stabilizing effect. If the side walls are not flat, but periodically corrugated in the direction of the flow, the range of the disturbance increases significantly. This is also reflected in a correspondingly stronger stabilization. However, the influence of corrugations disappears if its periodicity is very large or very small, as in both cases the corrugated wall transitions to a flat wall.

An unexpected influence of sidewalls on the stability of film flows can be seen in the fragmentation of the neutral curve. It will be shown that in channel flows, waves of a certain wavelength range are damped considerably, which may lead to a splitting of the unstable area of the stability map into two separate unstable isles. The wavelength of this selective damping depends almost exclusively on the channel width. The wider the channel, the longer the waves that are damped. A fragmentation of the neutral curve has so far only been observed in systems with undulated substrates, but not in systems with a flat substrate and flat sidewalls. Therefore the question arises how the channel width—i.e. a characteristic length transverse to the flow direction—can have such a significant influence on the damping wavelength—a characteristic length in flow direction.

An attempt on explanation for this question can be provided by the shape of the surface waves that are artificially generated to measure stability: Friction on the sidewalls causes the wave crest to be curved. The curvature of the wave generally depends strongly on the wavelength, but also on the channel width. At small wavelengths (compared to the channel width) the shape of the wave is dominated by the interaction of subsequent waves, whereas the channel width has no influence. However, if the wavelengths are very large, the influence of adjacent waves vanishes and the curvature depends exclusively on the channel width. In the transition region between the two regimes, i.e. at wavelengths similar to the channel width, an unexpected but distinct maximum in curvature was measured. This maximum of curvature is approximately at the wavelengths where selective damping occurs. However, the wavelength of the maximum curvature is always slightly smaller than the damping wavelength. Based on these observations, it can only be speculated that there is a relationship between the curvature and the damping of a wave in a channel flow. However, the exact interaction between the shape of a wave and the stability of the underlying stationary flow as well as the physical background of both phenomena are highly complex and require further investigations.

The damping effects presented in this thesis could be suitable for technical applications that require an undisturbed film. A stabilization of the flow can be achieved by adding side walls. This effect is further enhanced by the use of corrugated walls. Moreover, it is possible to achieve selective damping for a certain wavelength range up to arbitrarily high Reynolds numbers—at least within the measurement range of the experiments presented in this thesis. Finally, the damping wavelength can be tuned over a wide range by appropriate use of the side walls.

Zusammenfassung

Die schwerkraftgetriebene viskose Filmströmung ist ein klassisches Problem der Strömungsmechanik. Sie stellt ein vereinfachtes Modell für eine Vielzahl technischer und natürlicher Systeme dar. Im einfachsten Beispiel, der ebenen Filmströmung über eine unendlich ausgedehnte geneigte Ebene, lässt sich sowohl die stationäre Lösung – bekannt als *Nusselt-Strömung* – als auch die primäre Instabilität mit einfachen Mitteln aus den Navier-Stokes-Gleichungen bestimmen.

Die Nusselt-Strömung mit ihrem parabolischen Geschwindigkeitsprofil bietet eine gute Abschätzung für das Strömungsverhalten in realen Systemen, das heißt es lässt sich neben der stationären Strömung auch die Instabilität voraussagen. Letztere ist gerade für technische Systeme häufig von großer Bedeutung, denn in der Regel sind die durch die Instabilität verursachten Oberflächenwellen nicht erwünscht. Als prominentes Beispiel seien hier Beschichtungsvorgänge genannt, bei denen ein Film konstanter Dicke benötigt wird.

Es gibt zwei wesentliche Gründe, warum sich die Forschung zu Filmströmungen in den letzten Jahrzehnten weit über dieses einfache Modell hinaus entwickelt hat:

1) Das vereinfachte Modell kann reale Systeme nicht exakt abbilden. Die Untergründe in technischen und natürlichen Systemen sind häufig nicht perfekt glatt sondern rau, sei es zufällig oder beabsichtigt. Außerdem kann eine reale Strömung nicht unendlich ausgedehnt sein, sie muss beispielsweise durch Seitenwände begrenzt sein. Um diese komplexen mehrdimensionalen Strömungen zu beschreiben, sind verfeinerte Modelle und weiterführende experimentelle Untersuchungen nötig.

2) Gerade für technische Systeme ist es oft von wesentlichem Interesse, die Wellenbildung auf der Oberfläche der Filme zu unterdrücken. Durch die Variation der Bodenbeschaffenheit, aber auch durch geschickte Nutzung von Seitenwandeffekten ergibt sich die Möglichkeit, die primäre Instabilität des Films und damit die Entstehung von Oberflächenwellen zu kontrollieren.

Diese Dissertation beschäftigt sich vornehmlich mit dem Einfluss von Seitenwänden auf Filmströmungen über glattem Untergrund, also dem Unterschied zwischen Kanalströmung und ebener Filmströmung. Dazu wurden sowohl die stationäre Strömung, die primäre Instabilität und die Form der dabei entstehenden Wellen mit verschiedenen experimentellen Methoden untersucht und mit den numerisch bestimmbaren Ergebnissen für die ebene Filmströmung verglichen.

In einem ersten Schritt werden die für die Berechnung der primären Instabilität der ebenen Filmströmung benötigten Gleichungen – die Orr-Sommerfeld-Gleichung und die entsprechenden Randbedingungen – hergeleitet. Diese Gleichungen können nur im Grenzfall sehr langer

Wellen analytisch gelöst werden, mit numerischen Methoden ist jedoch der ganze Parameterraum zugänglich.

Des Weiteren muss sichergestellt werden, dass sämtliche Messungen der stationären Strömung und der Stabilität nicht von Einlaufeffekten des Kanals beeinflusst werden. Dazu wurde der Einlaufbereich durch Messung der Filmdicke und Oberflächengeschwindigkeit entlang des Kanals charakterisiert. Die Messpositionen für alle weiteren Messungen wurden so gewählt, dass alle Einlaufeffekte bis dorthin abgeklungen sind.

Es wird gezeigt, dass Seitenwände einen stabilisierenden Effekt auf Filmströmung haben, der mit abnehmender Kanalbreite signifikant zunimmt. Dies lässt sich durch den Einfluss der Seitenwände auf die stationäre Strömung erklären: In der unmittelbaren Umgebung der Seitenwände wird die Strömung verlangsamt. In diesem „gestörten“ Bereich werden Oberflächenwellen gedämpft und die Strömung somit stabilisiert. Je schmäler der Kanal ist, desto größer ist der prozentuale Anteil der von den Seitenwänden gestörten Flüssigkeit und demnach auch die stabilisierende Wirkung. Sind die Seitenwände nicht glatt, sondern in Strömungsrichtung periodisch unduliert, so vergrößert sich die Reichweite der Störung deutlich. Das spiegelt sich auch in einer entsprechend stärkeren Stabilisierung wider. Allerdings verschwinden die Einflüsse der Undulation, wenn deren Periodizität sehr groß oder sehr klein ist, da sich in beiden Fällen die undulierte Wand einer glatten Wand annähert.

Ein unerwarteter Einfluss von Seitenwänden auf die Stabilität von Filmströmungen zeigt sich in der Fragmentierung der neutralen Kurve. Es wird gezeigt, dass in Kanalströmungen Wellen in einem bestimmten Wellenlängenbereich erheblich gedämpft werden, was zu einer Aufspaltung des instabilen Bereichs der Stabilitätskarte in zwei getrennte instabile Inseln führen kann. Die Wellenlänge dieser selektiven Dämpfung hängt fast ausschließlich von der Kanalbreite ab. Mit steigender Kanalbreite werden längere Wellen gedämpft. Eine Fragmentierung der neutralen Kurve ist bisher nur in Systemen mit unduliertem Boden, jedoch nicht in Systemen mit glattem Boden und glatten Seitenwänden beobachtet worden. Daher stellt sich die Frage, wie die Kanalbreite – also eine charakteristische Länge quer zur Strömungsrichtung – einen so deutlichen Einfluss auf die Wellenlänge der Dämpfung – eine charakteristische Länge in Strömungsrichtung – nehmen kann.

Einen Erklärungsansatz für diese Frage liefert die Form der Oberflächenwellen, die zur Messung der Stabilität künstlich erzeugt werden: Durch Reibung an den Seitenwänden ist die Wellenfront gekrümmt. Die Krümmung der Welle hängt im allgemeinen stark von der Wellenlänge, aber auch der Kanalbreite ab. Bei kleinen Wellenlängen (im Vergleich zur Kanalbreite) wird die Form der Welle durch die Interaktion benachbarter Wellenzüge dominiert, die Kanalbreite hat hierbei keinen Einfluss. Sind die Wellenlängen jedoch sehr groß, verschwindet der Einfluss benachbarter Wellen und die Krümmung hängt ausschließlich von der Kanalbreite ab. Im Übergangsbereich zwischen den beiden Regimes, also bei Wellenlängen im Bereich der Kanalbreite, wurde ein unerwartetes, aber deutliches Maximum in der Krümmung gemessen. Dieses Maximum der Krümmung liegt annähernd bei den Wellenlängen, bei denen die selektive Dämpfung auftritt. Die Wellenlänge der maximalen Krümmung ist jedoch immer etwas kleiner als die Wellenlänge der Dämpfung. Auf der Grundlage dieser Beobachtungen kann nur spekuliert werden, dass es einen Zusammenhang zwischen der Krümmung und der Dämpfung einer Welle in einer Kanalströmung gibt. Die genaue Wechselwirkung zwischen der Form einer Welle und der Stabilität der ihr zugrunde liegenden stationären Strömung sowie der physikalische Hintergrund beider Phänomene sind jedoch sehr komplex und erfordern weitere Untersuchungen.

Die in dieser Dissertation vorgestellten Dämpfungseffekte könnten für technische Anwendungen geeignet sein, die einen ungestörten Film erfordern. Eine Stabilisierung der Strömung kann durch das Hinzufügen von Seitenwänden erreicht werden. Dieser Effekt wird durch den Einsatz undulierter Wände noch zusätzlich verstärkt. Darüberhinaus ist es möglich, eine selektive Dämpfung für einen bestimmten Wellenlängenbereich bis zu beliebig hohen Reynolds-Zahlen zu erreichen – zumindest innerhalb des Messbereichs der in dieser Arbeit vorgestellten Experimente. Durch geeigneten Einsatz der Seitenwände kann schließlich die Wellenlänge der Dämpfung über einen großen Bereich hin variiert werden.

Contents

1 Introduction

Viscous thin film flows are present in a large number of artificial and natural systems. They appear among others in coating [1–3] and heat exchanging applications [4, 5]. In the natural environment viscous films can be found in glaciers [6], avalanches [7] and debris flows [8] as well as in biofilms [9] and tear films [10]. It is of special interest to understand the stability phenomena of film flows and in particular the means of modifying the stability against free surface perturbations.

1.1 The basic flow

1.1.1 Basic flow over flat substrates

The first to unveil the parabolic profile of the fully developed gravity-driven film flow was Nusselt [11] in 1916. The assumption of an unidirectional steady state flow over a perfectly flat surface of infinite extent is suitable for many applications. However, since in natural and technical systems these assumptions in general do not apply, refined models and experiments were needed. The impact of side walls on the film flow was analytically investigated by Scholle and Aksel [12] and later experimentally proven by Haas et al. [13]. They found a reduction of the flow velocity in the vicinity of the side walls due to the no-slip condition. Additionally, there is capillary elevation of the fluid surface near the walls which leads to a locally higher film thickness and therefore to a higher flow velocity at the surface. Depending on other system parameters, these two competing effects may lead to an velocity overshoot at a certain distance to the side walls. The overshoot vanishes if the film thickness is large enough. On the other hand, for very thin films, where the capillary elevation plays a major role, this effect is dominant. The special case of the thin film limit and the film rupture which leads to a corner flow is discussed in [14].

1.1.2 Basic flow over undulated substrates

The assumption of a flat substrate may be valid for some special technical applications but particularly in natural systems substrates are never perfectly flat. A simple model for corrugated substrates was made by Wang [15] who analytically investigated the effect of a small sinusoidal undulation of the bottom profile on the two dimensional film flow. He found the free surface to be strongly deformed depending on the substrate and the surface tension.

If the corrugations are sufficiently large, eddies can appear in the bottoms of the troughs [16]. Furthermore, if the corrugations are steep enough, even multiple eddies can occur. The analytical calculations by Scholle et al. [17] and the numerical results of Nguyen and Bontozoglou [18] match the experimental findings of Wierschem et al. [16]. Scholle et al. [19] found out that eddies in the troughs of the corrugation act like fluidic roller bearings that cause a slight drag reduction. If the fluid's inertia is taken into account, the eddies are no longer symmetrical but tilted [20, 21] and eventually might even break up [20]. Moreover, eddies may be suppressed within a certain range of the Reynolds number if the system parameters are suitable [22–24]. When leaving the constraint of sinusoidal corrugations more phenomena can be found: Pak and Hu [24] found eddies not only in the troughs of rectangular substrates but also at the free surface of the fluid.

The free surface is significantly affected by strong corrugated substrates. Linear as well as nonlinear resonance effects occur which lead to an amplification of the standing free surface waves compared to the amplitude of the corrugations [25–28]. Also more complex structures like surface rollers or hydraulic jumps may appear [23, 29].

1.2 The linear stability of the basic flow

1.2.1 Linear stability of the plane flow over flat substrates

Since in natural and technical systems ambient noise is inevitable, the stability of film flows has been an important field of research in recent decades. Kapitza and Kapitza [30, 31] were the first to report on spontaneously emerging waves in film flows. The waves appear if the volume flux (respectively the Reynolds number) exceeds a certain value. These groundbreaking results were taken up by Benjamin [32] and Yih [33] who applied a linear perturbation approach to the Navier–Stokes equation and obtained the Orr–Sommerfeld equation [34–36] with the corresponding boundary conditions. They were able to analytically solve the equations in the limit of long waves and found a convective instability of the long-wave type at the critical Reynolds number $\mathrm{Re}_{\mathrm{crit}} = (5/4)\cot\alpha$, depending on the inclination angle α. Higher order long wave approximations can be found in the book of Chang and Demekhin [37]. The analytical findings, which were restricted to the limit of long waves, were experimentally confirmed by Liu et al. [38] who also extended the stability charts for short waves.

1.2.2 Linear stability of the plane flow over undulated substrates

In natural and technical systems, substrates are generally not perfectly flat, but corrugated. Therefore, a major task in the studies of film flows is to understand the effects of undulated substrates on the stability of the system. Analytical and experimental studies were carried out for weakly undulated substrates. It was found that they have a slightly stabilizing effect [39, 40]. For strongly undulated substrates there are stabilizing as well as destabilizing effects [41]. An important fact is that undulated substrates do not only shift the neutral curve, but can change the entire shape of the linear stability chart. A fragmentation of the neutral curve and a

formation of an unstable isle was first described theoretically by Heining and Aksel [42]. Their prediction was experimentally confirmed by Pollak and Aksel [43], who reported on crucial flow stabilization and multiple instability branches in the linear stability chart of gravity-driven viscous films flowing down a wavy incline of sinusoidal shape. It is possible to switch between different types of stability charts by varying system parameters, e.g. the inclination angle, the viscosity or the corrugation's periodicity [44]. The exact shape of the corrugation, however, has no considerable influence on the stability chart [45]. New findings show that there are only a few different patterns of stability charts. Schörner [46] unveiled a universal pathway along which the stability charts evolve when the system parameters are changed. A detailed discussion of the effects of undulated substrates on the stability of film flows as well as the steady state flow can be found in the review of Aksel and Schörner [47].

1.2.3 Effect of side walls on the stability of the flow

The problem of instability of channel flows has been known for decades, but could not be sufficiently explained so far. Fulford [48, 49] published a first comprehensive review of experimental and theoretical investigations of film flows in a rectangular channel. The focus of these investigations was on the stability and the influence of the contact angle at the side walls on the velocity distribution in the channel, as previously observed by Hopf [50].

The effect of side walls on the critical Reynolds number of film flows over flat substrates was experimentally studied by Vlachogiannis et al. [51]. They used a conductive measurement technique to obtain the time series of the film thickness at different positions along the channel. The measurements of the marginal stability was performed at a very low excitation frequency so that there is practically no difference to the critical Reynolds number at zero frequency. For large channel widths the measured value of $\mathrm{Re}_{\mathrm{crit}}$ matches the theoretical value for the two-dimensional case very well whereas a significant increase of $\mathrm{Re}_{\mathrm{crit}}$ was found for decreasing channel widths. This effect becomes less pronounced for larger inclination angles.

The surface tension was found to play a considerable role for the stability of channel flows as well. Georgantaki et al. [52] found a significant increase in the critical Reynolds number when increasing the surface tension of the fluid.

A transition from long wave to short wave instability in the vicinity of the side walls was described by Pollak et al. [53]. Also the contact angle between the fluid and the side wall was found to play a considerable role for the stability of the flow whereas the qualitative structure of the neutral curve remains the same.

A special case of three-dimensional flow over corrugated substrates is discussed in the work of Kuehner et al. [54]. They investigated the gravity-driven flow through an inclined corrugated circular pipe which is partly filled with fluid. The behavior of the static free surface is similar to the two-dimensional case of undulated substrates. They did not perform a measurement of the primary instability. Yet, spontaneously emerging free surface waves were observed whose wavelength and frequency were nearly independent of the inclination angle and the flow rate.

1.2.4 Effect of side walls on the shape of the waves

The influence of the side walls on the surface waves is not only visible in the stability of the flow, but also in the shape of the emerging waves. Leontidis et al. [55] observed a parabolic crest line whose curvature depends on several system parameters. It was found that narrow channels cause strongly curved waves whereas the curvature of the crest line tends to zero for wide channels. This matches the case of infinite wide channels which corresponds to the two-dimensional case where only plane waves occur (at least when ignoring secondary instabilities). An increase in the Reynolds number also leads to a reduction of the wave's curvature. Leontidis et al. [55] measured wave properties for two different excitation frequencies. They found that—at least within the measurement range—waves with higher frequency have a significantly lower curvature.

1.3 Inflow effects

In many hydrodynamic models—and in particular in the stability analysis presented in this thesis—a fully developed flow is considered. Yet, in experimental systems inflow and outflow effects are inevitable since the geometric dimensions of experimental setups are finite. Moreover, in technical systems it is often desired to have limited extent and so inflow effects have to be considered.

Schiller [56] investigated the inflow of a circular pipe where a constant velocity profile at the inlet was assumed. He used boundary layer equations that were suggested by Prandtl. The growing boundary layers at the walls finally merge in the center of the pipe after a certain distance, called the *inflow length*. Schiller found that the dimensionless inflow length is proportional to the Reynolds number. This relation, which appears in many other models presented in the following, is a fundamental result of the boundary layer equations. Only the prefactor differs according to the chosen model.

Lynn [57] investigated the transition from the gravity-driven Poiseuille flow to the Nusselt flow. At the inlet of the channel the fluid is covered by a lid so that the parabolic Poiseuille profile develops. Downstream of the inlet the fluid has a free surface and the Poiseuille flow transitions to a Nusselt flow. The measurement of the accelerating surface velocity was in great agreement with the analytical results of parabolic boundary layer equations, except for a small region close to the inlet where the boundary layer equations are not valid. Further boundary layer approaches including numerical calculations can be found in [58–60]. Cerro and Whitaker [61] used three different numerical approaches to examine the transition from the gravity-driven Poiseuille flow to the Nusselt flow: First, a simple parabolic equation (boundary layer) approach where the film thickness is assumed constant. Second, an elliptical equation approach where the downstream boundary condition matches a parabolic equation. And third, a parabolic equation approach using the von Mises transformation that allows a variable film thickness. They compared their numerical calculations to the experimental data of Lynn [57] and found that the simple parabolic boundary layer equations adequately describe the full inflow area, except for a small region close to the inlet.

1.4 Scope of this thesis

The present thesis deals with the influence of side walls on gravity-driven viscous film flows. Various measurement techniques were used to characterize the steady state flow as well as the primary instability of the flow. New phenomena concerning the stability of film flows confined by flat or corrugated side walls were discovered. In addition, the properties of the excited waves were measured and associated with the measured stability charts. Finally, the inflow area of the channel was characterized to ensure that the stability measurements were performed in the fully developed flow.

The thesis has the following structure: Chapter 2 contains the derivation of the Orr–Sommerfeld equation with its corresponding boundary conditions, which describe the linear stability of the two dimensional film flow. The analytical solution of the equation is shown using the long wave approximation, whereas the numerical solution covers the full parameter space. The experimental system and measurement techniques are presented in chapter 3. The findings of this thesis can be found in chapter 4, which is divided into four parts: Section 4.1 deals with the characterization of the inflow area of the channel to ensure that all following measurements take place in an area of fully developed flow. In section 4.2 the influence of the side walls on the basic flow is examined. The effect of the side walls on the stability of the flow and particularly the difference to the two dimensional case is presented in section 4.3. Finally, section 4.4 deals with the properties of the emerging waves and their relation to the stability of the flow. The summary of this thesis is given in chapter 5.

2 Stability of the two-dimensional film flow

The main topic of this thesis is to investigate the influence of side walls on the stability of gravity-driven viscous film flows. To this end channel flows with finite width will be compared to plane flows of infinite extent. Since in the experimental setup side walls are inevitable the stability of the plane flow is experimentally inaccessible. Therefore a two-dimensional theoretical calculation—without any side walls—will be used to characterize the stability of the plane flow.

First, the basic two-dimensional flow will be derived in section 2.1. Afterwards the Orr–Sommerfeld equation with corresponding boundary conditions will be derived in section 2.2. In section 2.3 the analytical long-wave solution will be presented, whereas the numerical solution for the whole parameter space is given in section 2.4.

2.1 Steady state solution

Fig. 2.1 shows a sketch of the two dimensional steady state film flow over a flat substrate tilted by an angle α to the horizontal. The incompressible fluid with film thickness H has a density ρ and a dynamic viscosity η. It is driven by the gravitational acceleration g. The layer of air above the fluid is assumed inviscid with zero pressure. For the undisturbed flow, denoted by capital letters, the velocity field is assumed unidirectional: $\vec{u} = U(y)\vec{e}_x$. For this assumption the continuity is already fulfilled and the Navier–Stokes equations reduce to

$$x: \qquad 0 = \partial_x P + \rho g \sin\alpha + \eta \partial_y^2 U\,, \tag{2.1}$$

$$y: \qquad 0 = \partial_y P + \rho g \cos\alpha\,. \tag{2.2}$$

Eq. (2.2) can be solved for the pressure P by using the boundary condition $P = 0$ at the fluid surface $y = H$:

$$P(y) = \rho g \cos\alpha\, H \left(1 - \frac{y}{H}\right)\,. \tag{2.3}$$

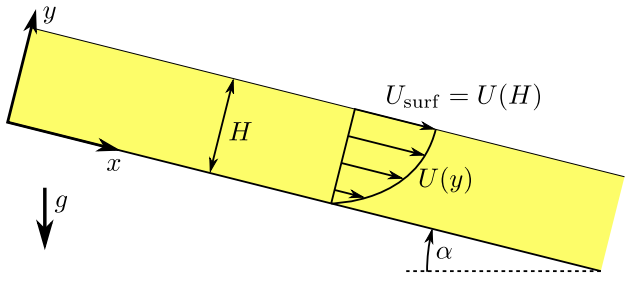

Figure 2.1: Two dimensional steady state film flow.

The pressure therefore does not depend on the x-coordinate. Thus eq. (2.1) can be solved with the two boundary conditions for the velocity: $U = 0$ at $y = 0$ (no-slip condition at the bottom) and $\partial_y U = 0$ at $y = H$ (vanishing shear stress at the interface to the inviscid air). The kinematic viscosity is introduced as $\nu = \eta/\rho$.

$$U(y) = \frac{g \sin\alpha}{2\nu} H^2 \left(2 - \frac{y}{H}\right) \frac{y}{H} \,. \tag{2.4}$$

The flow velocity at the surface is given by

$$U_{\text{surf}} = U(H) = \frac{g \sin\alpha}{2\nu} H^2 \,. \tag{2.5}$$

In the following sections all calculations will be done with dimensionless quantities. The characteristic quantities of the Nusselt flow are the film thickness H and the surface velocity U_{surf}. The dimensionless quantities, marked by the superscript *, for the time t, the length y, the velocity U and the pressure P are

$$t^* = \frac{t U_{\text{surf}}}{H} \,, \tag{2.6}$$

$$y^* = \frac{y}{H} \,, \tag{2.7}$$

$$U^* = \frac{U}{U_{\text{surf}}} \,, \tag{2.8}$$

$$P^* = \frac{P}{\rho U_{\text{surf}}^2} \,. \tag{2.9}$$

Other lengths and velocities will be nondimensioned analogous to eqs. (2.7) and (2.8). Other occurring pressures, but also stresses, will be nondimensionised by eq. (2.9). With the definition of the Reynolds number

$$\text{Re} = \frac{U_{\text{surf}} H}{\nu} \,, \tag{2.10}$$

the dimensionless steady state solution (eqs. (2.4) and (2.3)) of the film flow now is

$$U^* = 2y^* - y^{*\,2} \,, \tag{2.11}$$

$$P^* = \frac{2}{\text{Re} \tan\alpha} (1 - y^*) \,. \tag{2.12}$$

2.2 Linear stability: derivation of the Orr–Sommerfeld equation and its corresponding boundary conditions

The equations in the section above describe a stationary solution of the Navier–Stokes equation, but they give no information whether this solution is stable or unstable. For the stability analysis one has to consider an instationary flow and omit the simplifications made above. But since the full Navier–Stokes equations can not be solved analytically, one has to accept certain constraints. In this section a linear stability analysis will be presented. For this case the waves are considered as infinitesimal small perturbations of the basic flow. This leads to the fact that the resulting equations can be linearized and eventually even solved analytically. The upcoming calculations follow in large parts the works of Yih [33] and Chang and Demekhin [37], who derived the Orr–Sommerfeld equation [34–36] with corresponding boundary conditions.

Orr–Sommerfeld equation

To obtain the Orr–Sommerfeld equation, infinitesimal small wavelike perturbations (see fig. 2.2(a)) are added to both velocity components U^* and $V^* = 0$ as well as the pressure P^* and the film thickness $H^* = 1$ of the basic flow:

$$u^* = U^* + \varepsilon\hat{u} \qquad \text{with} \qquad \hat{u} = \hat{u}_0(y^*)\mathrm{e}^{\mathrm{i}k^*(x^*-c^*t^*)}\,, \tag{2.13}$$

$$v^* = \varepsilon\hat{v} \qquad\qquad \hat{v} = \hat{v}_0(y^*)\mathrm{e}^{\mathrm{i}k^*(x^*-c^*t^*)}\,, \tag{2.14}$$

$$p^* = P^* + \varepsilon\hat{p} \qquad \hat{p} = \hat{p}_0(y^*)\mathrm{e}^{\mathrm{i}k^*(x^*-c^*t^*)}\,, \tag{2.15}$$

$$h^* = 1 + \varepsilon\hat{h} \qquad \hat{h} = \hat{h}_0(y^*)\mathrm{e}^{\mathrm{i}k^*(x^*-c^*t^*)}\,. \tag{2.16}$$

The prefactor $\varepsilon \ll 1$ is used, so that the perturbations ($\hat{u}, \hat{v}, \hat{p}$ and $\hat{h}$) are of the same order of magnitude as the corresponding quantities of the basic flow. Quantities with hat and index 0 are the complex amplitudes of the perturbations and depend only on the coordinate y^*. The wavenumber and the phase velocity of the perturbations are denoted as k^* and c^*.

Eqs. (2.13) trough (2.16) are now substituted into the full two-dimensional incompressible Navier–Stokes equations. In the resulting equations all terms of order ε^0 cancel out since they

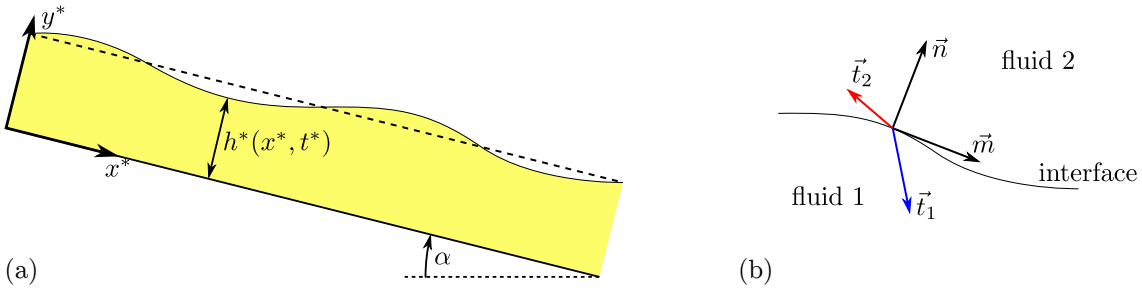

Figure 2.2: (a) Sketch of the perturbed flow. The dashed line shows the undisturbed surface at $y^* = 1$. (b) General example of the normal vector $\vec{n}$, tangential vector $\vec{m}$ and stress vectors $\vec{t}_1, \vec{t}_2$ (with regard to $\vec{n}$) at an interface between two fluids.

describe the basic flow that is already a solution of the Navier–Stokes equations. The equations are now linearized by omitting all terms of order ε^2 and higher. The remaining terms of the Navier–Stokes equations and the continuity equation are

$$x^*: \qquad \mathrm{i}k^*\hat{u}(U^*-c^*)+\hat{v}U^{*\prime}=-\mathrm{i}k^*\hat{p}+\frac{1}{\mathrm{Re}}(\hat{u}''-k^{*2}\hat{u})\,, \tag{2.17}$$

$$y^*: \qquad \mathrm{i}k^*\hat{v}(U^*-c^*)=-\hat{p}'+\frac{1}{\mathrm{Re}}(\hat{v}''-k^{*2}\hat{v})\,, \tag{2.18}$$

$$\text{continuity equation}: \qquad \mathrm{i}k^*\hat{u}+\hat{v}'=0\,. \tag{2.19}$$

The derivative to y^* is denoted by prime, the derivative to x^* and t^* can be executed and result in the prefactor $\mathrm{i}k^*$ and $-\mathrm{i}k^*c^*$, respectively.

The pressure p^* can be eliminated by differentiating eq. (2.17) by y^* and subtracting it from eq. (2.18), multiplied by $\mathrm{i}k^*$. Afterwards the continuity equation (2.19) is used to define the complex stream function $\hat{\psi}$ of the perturbation:

$$\hat{u}=\partial_{y^*}\hat{\psi}=\hat{\psi}'\,, \qquad \hat{v}=-\partial_{x^*}\hat{\psi}=-\mathrm{i}k^*\hat{\psi}\,. \tag{2.20}$$

This now leads to the Orr–Sommerfeld equation

$$\hat{\psi}''''-2k^{*2}\hat{\psi}''+k^{*4}\hat{\psi}=\mathrm{i}k^*\mathrm{Re}\left[(U^*-c^*)\left(\hat{\psi}''-k^{*2}\hat{\psi}\right)-U^{*\prime\prime}\hat{\psi}\right]\,. \tag{2.21}$$

The Orr–Sommerfeld equation is a fourth order ordinary differential equation which needs four corresponding boundary conditions. These are given by the kinematic and dynamic boundary condition at the bottom and at the free surface. In the following, these four conditions will be formulated and rewritten in terms of $\hat{\psi}$ so that they are suitable for the solution of eq. (2.21).

Boundary conditions at the bottom

The boundary conditions at the bottom are given by the no-slip condition ($u^*=v^*=0$):

$$y^*=0: \qquad \hat{\psi}=0\,, \tag{2.22}$$

$$\hat{\psi}'=0\,. \tag{2.23}$$

Boundary conditions at the free surface

The boundary conditions at the free surface are more complex since the position of the surface itself varies with time and space. From the kinematic boundary condition it is possible to obtain a relation between the position of the free surface and the stream function. The two boundary conditions for the stream function then can be obtained from the dynamic boundary condition, i.e. the normal and the tangential stress balance at the free surface.

Kinematic boundary condition:
The kinematic boundary condition at the free surface is given by

$$y^* = h^* : \qquad \partial_{t^*} h^* + u^* \partial_{x^*} h^* = v^* \,. \tag{2.24}$$

Since the position of the free surface h^* is unknown, the equation above is not useful. The boundary condition has to be transferred from $y^* = h^*$ to $y^* = 1$. The transfer of the single terms in eq. (2.24) can be found in the appendix A.1. In this case, however, the transfer has no impact on the equation:

$$y^* = 1 : \qquad \partial_{t^*} h^* + u^* \partial_{x^*} h^* = v^* \,. \tag{2.25}$$

After carrying out the derivatives the equation can be written as

$$y^* = 1 : \qquad -\mathrm{i}k^* c^* \varepsilon \hat{h} + U^* \mathrm{i}k^* \varepsilon \hat{h} = \varepsilon \hat{v} + \mathcal{O}\left(\varepsilon^2\right) \,. \tag{2.26}$$

Now a relation between the film thickness and the velocity respectively the stream function (see eq. (2.20)) is given:

$$y^* = 1 : \qquad \hat{h} = \frac{\hat{v}}{\mathrm{i}k^*(U^* - c^*)} = \frac{-\hat{\psi}}{U^* - c^*} \,. \tag{2.27}$$

Dynamic boundary condition:
The dynamic boundary condition is given in general by the Young–Laplace equation, here in its dimensionless form (see figure 2.2(b))

$$y^* = h^* : \qquad \vec{t}_1^{\,*} + \vec{t}_2^{\,*} = \frac{\kappa^*}{\mathrm{We}} \vec{n} \,, \tag{2.28}$$

with $\vec{t}_1$ and $\vec{t}_2$ being the dimensionless stress vectors of fluid 1 and fluid 2, κ^* being the dimensionless curvature of the interface and $\vec{n}$ its normal vector. The Weber number is

$$\mathrm{We} = \frac{\rho U_{\mathrm{surf}}^2 H}{\sigma} \,, \tag{2.29}$$

where σ is the surface tension. In the given system the stress vector $\vec{t}_2^{\,*}$ equals zero since fluid 2 (air) has no viscosity in this model and the pressure is zero. The remaining stress vector is written without subscript: $\vec{t}_1^{\,*} =: \vec{t}^*$. Eq. (2.28) can be split into its normal and tangential component:

$$y^* = h^* : \qquad \vec{t}^* \cdot \vec{m} = t_t^* = 0 \,, \tag{2.30}$$

$$\vec{t}^* \cdot \vec{n} = t_n^* = \frac{\kappa^*}{\mathrm{We}} \,. \tag{2.31}$$

The tangential vector is denoted as $\vec{m}$ (see fig. 2.2(b)). These equations show that at the surface of the fluid the shear stress vanishes but the normal stress exceeds a jump caused by the curved surface.

The dimensionless stress vector is given by

$$\vec{t}^* = \frac{2}{\mathrm{Re}} E^* \cdot \vec{n} - p^* \vec{n} \tag{2.32}$$

with the dimensionless strain rate tensor

$$E^* = \frac{1}{2}\left[\nabla^*\vec{u}^* + (\nabla^*\vec{u}^*)^\mathsf{T}\right] . \tag{2.33}$$

Please see appendix A.2 for the nondimensionalization of the stress vector. The tangential and normal vectors are given by

$$\vec{m} = \vec{e}_{x^*} + \partial_{x^*} h^* \vec{e}_{y^*} , \tag{2.34}$$

$$\vec{n} = -\partial_{x^*} h^* \vec{e}_{x^*} + \vec{e}_{y^*} . \tag{2.35}$$

The length of the vectors is $1 + \mathcal{O}(\varepsilon^2)$, therefore no normalization is needed. The surface curvature can be written as

$$\kappa^* = \frac{\partial^2_{x^*} h^*}{\left(1 + (\partial_{x^*} h^*)^2\right)^{\frac{3}{2}}} = \varepsilon \partial^2_{x^*} \hat{h} + \mathcal{O}(\varepsilon^2) . \tag{2.36}$$

Now eqs. (2.13) through (2.16), (2.34) and (2.35) are substituted in eq. (2.32) to obtain the components of the stress vector:

$$y^* = h^* : \qquad t_t^* = \frac{1}{\mathrm{Re}}\left(\partial_{y^*} U^* + \varepsilon \partial_{y^*} \hat{u} + \varepsilon \partial_{x^*} \hat{v}\right) + \mathcal{O}(\varepsilon^2) , \tag{2.37}$$

$$t_n^* = \frac{1}{\mathrm{Re}}\left(-2\varepsilon(\partial_{y^*} U^*)(\partial_{x^*} \hat{h}) + 2\varepsilon \partial_{y^*} \hat{v}\right) - P^* - \varepsilon \hat{p} + \mathcal{O}(\varepsilon^2) . \tag{2.38}$$

These two components of the stress vector and the dimensionless curvature (eq. (2.36)) are substituted in the dynamic boundary condition (eqs. (2.30) and (2.31)):

$$y^* = h^* : \qquad \frac{1}{\mathrm{Re}}\left(\partial_{y^*} U^* + \varepsilon \partial_{y^*} \hat{u} + \varepsilon \partial_{x^*} \hat{v}\right) = 0 , \tag{2.39}$$

$$\frac{1}{\mathrm{Re}}\left(-2\varepsilon(\partial_{y^*} U^*)(\partial_{x^*} \hat{h}) + 2\varepsilon \partial_{y^*} \hat{v}\right) - P^* - \varepsilon \hat{p} = \frac{\varepsilon \partial^2_{x^*} \hat{h}}{\mathrm{We}} . \tag{2.40}$$

Eqs. (2.39) and (2.40) are now transferred from $y^* = h^*$ to $y^* = 1$ (see appendix A.1):

$$y^* = 1 : \qquad \hat{h} \partial^2_{y^*} U^* + \partial_{y^*} \hat{u} + \partial_{x^*} \hat{v} = 0 , \tag{2.41}$$

$$\frac{2}{\mathrm{Re}} \partial_{y^*} \hat{v} - \hat{h} \partial_{y^*} P^* - \hat{p} = \frac{\partial^2_{x^*} \hat{h}}{\mathrm{We}} . \tag{2.42}$$

After substituting $\partial^2_{y^*} U^* = -2$ and $\partial_{y^*} P^* = -2/(\mathrm{Re} \tan\alpha)$ one obtains the equations

$$y^* = 1 : \qquad -2\hat{h} + \partial_{y^*} \hat{u} + \partial_{x^*} \hat{v} = 0 , \tag{2.43}$$

$$\frac{2}{\mathrm{Re}}\left(\partial_{y^*} \hat{v} + \frac{\hat{h}}{\tan\alpha}\right) - \hat{p} = \frac{\partial^2_{x^*} \hat{h}}{\mathrm{We}} . \tag{2.44}$$

Eq. (2.43) can finally be rewritten by using the definition of the stream function (2.20), using the kinematic boundary condition (2.27) and carrying out the derivatives:

$$y^* = 1: \qquad \hat{\psi}'' + \left(k^{*2} + \frac{2}{1-c^*}\right)\hat{\psi} = 0\,. \tag{2.45}$$

In eq. (2.44) the pressure $\hat{p}$ has to be eliminated. Therefore it is solved by $\hat{p}$ and substituted in the x^*-component of the Navier–Stokes equation (2.17). Then—after substituting the stream function (2.20)—using the kinematic boundary condition (2.27) and carrying out the derivatives, one obtains the equation

$$y^* = 1: \qquad \hat{\psi}''' + \left[-3k^{*2} - \mathrm{i}k^*\mathrm{Re}\,(1-c^*)\right]\hat{\psi}' = -\frac{\mathrm{i}k^*}{1-c^*}\left(\frac{2}{\tan\alpha} + k^{*2}\frac{\mathrm{Re}}{\mathrm{We}}\right)\hat{\psi}\,. \tag{2.46}$$

The use of the Weber number (see eq. (2.29)) is not suitable for solving this system, because it contains quantities of the basic flow like the film thickness and the surface velocity. Instead the use of the Kapitza number

$$\mathrm{Ka} = \frac{\sigma}{\rho g^{\frac{1}{3}}\nu^{\frac{4}{3}}} \tag{2.47}$$

is preferred, since it only contains fluid properties and is therefore independent of the basic flow. The Weber number can be replaced by

$$\frac{1}{\mathrm{We}} = \mathrm{Ka}\left(\frac{2}{\mathrm{Re}^5\sin\alpha}\right)^{\frac{1}{3}}\,. \tag{2.48}$$

The Reynolds number now is the only quantity containing information of the basic flow.

The final differential equation (eq. (2.21)) with its boundary conditions (eqs. (2.22), (2.23), (2.45) and (2.46)) is given by

$$0 \le y^* \le 1: \qquad \hat{\psi}'''' - 2k^{*2}\hat{\psi}'' + k^{*4}\hat{\psi} = \mathrm{i}k^*\mathrm{Re}\left[(U^*-c^*)\left(\hat{\psi}'' - k^{*2}\hat{\psi}\right) - U^{*\prime\prime}\hat{\psi}\right]\,, \tag{2.49}$$

$$y^* = 0: \qquad \hat{\psi} = 0\,, \tag{2.50}$$

$$\hat{\psi}' = 0\,, \tag{2.51}$$

$$y^* = 1: \qquad \hat{\psi}'' = -\left(k^{*2} + \frac{2}{1-c^*}\right)\hat{\psi}\,, \tag{2.52}$$

$$\hat{\psi}''' = \left(3k^{*2} + \mathrm{i}k^*\mathrm{Re}\,(1-c^*)\right)\hat{\psi}' - \frac{\mathrm{i}k^*}{1-c^*}\left[\frac{2}{\tan\alpha} + k^{*2}\mathrm{Ka}\left(\frac{2}{\mathrm{Re}^2\sin\alpha}\right)^{\frac{1}{3}}\right]\hat{\psi}\,. \tag{2.53}$$

The steady state solution is given by $U^* = 2y^* - y^{*2}$ (see eq. (2.11)). This is a fourth order ordinary linear homogeneous differential equation with linear and homogeneous boundary conditions that constitutes an eigenvalue problem. The solution $\hat{\psi}$, that is a superposition of

the four fundamental solutions, can only be determined except for the prefactor. To solve the equation, one of the occurring quantities has to be considered as eigenvalue. The choice of the eigenvalue depends on the type of instability that is assumed.

In case of a *temporal instability* it is assumed that the perturbations grow exponentially in time. The wave number k^* has to be real and the phase velocity $c^* = c_\mathrm{r}^* + \mathrm{i}c_\mathrm{i}^*$ has to be complex. For example the perturbation of the surface (eq. (2.16))

$$\hat{h} = \hat{h}_0 \mathrm{e}^{\mathrm{i}k^*(x^*-c^*t^*)} = \hat{h}_0 \mathrm{e}^{k^*c_\mathrm{i}^*t^*} \mathrm{e}^{\mathrm{i}k^*(x^*-c_\mathrm{r}^*t^*)} = \hat{h}_0 \mathrm{e}^{b_\mathrm{t}^*t^*} \mathrm{e}^{\mathrm{i}k^*(x^*-c_\mathrm{r}^*t^*)} \tag{2.54}$$

has a periodic term with constant amplitude and an exponential term with the *temporal growth rate* $b_\mathrm{t}^* = k^*c_\mathrm{i}^*$. In this case the wave number k^* is given and the phase velocity c^* is the eigenvalue of the problem. The temporal growth rate b_t^* that depends directly on the phase velocity c^* determines the stability of the system. For $b_\mathrm{t}^* < 0$ the perturbations decay and the system is stable. On the other hand, for $b_\mathrm{t}^* > 0$ the perturbations grow exponentially in time and the system in unstable. For $b_\mathrm{t}^* = 0$ the amplitude of the perturbations remains constant.

In case of a *spatial instability* it is assumed that the perturbations grow exponentially in space. Here, the phase velocity is rewritten as $c^* = \omega^*/k^*$ with the dimensionless angular frequency ω^*. The angular frequency ω^* has to be real and the wave number $k^* = k_\mathrm{r}^* + \mathrm{i}k_\mathrm{i}^*$ has to be complex. The perturbation of the surface now is

$$\hat{h} = \hat{h}_0 \mathrm{e}^{\mathrm{i}k^*(x^*-c^*t^*)} = \hat{h}_0 \mathrm{e}^{\mathrm{i}(k^*x^*-\omega^*t^*)} = \hat{h}_0 \mathrm{e}^{-k_\mathrm{i}^*x^*} \mathrm{e}^{\mathrm{i}(k_\mathrm{r}^*x^*-\omega^*t^*)} = \hat{h}_0 \mathrm{e}^{b_\mathrm{s}^*x^*} \mathrm{e}^{\mathrm{i}(k_\mathrm{r}^*x^*-\omega^*t^*)} \,. \tag{2.55}$$

The perturbation grows (decays) in space with the *spatial growth rate* $b_\mathrm{s}^* = -k_\mathrm{i}^*$. In this case the eigenvalue of the system is the complex wave number k^* whereas the angular frequency ω^* is given.

2.3 Analytical solutions for long waves

The Orr–Sommerfeld equation with the corresponding boundary conditions (eqs. (2.49) through (2.53)) cannot be solved analytically for the whole parameter space. However, for the case of the temporal instability some approximations can be done. For small values of k^* the equations can be simplified. In the following section the eigenvalue problem will be solved for small values of k^* in zeroth and in first order.

Long wave approximation (zeroth order)

If in the set of equations (2.49) through (2.53) all terms of order k^* and higher are omitted, one gets the following equations:

$$0 \leq y^* \leq 1: \qquad \hat{\psi}'''' = 0\,, \tag{2.56}$$

$$y^* = 0: \qquad \hat{\psi} = 0\,, \tag{2.57}$$

$$\hat{\psi}' = 0\,, \tag{2.58}$$

$$y^* = 1: \qquad \hat{\psi}'' = -\frac{2}{1-c^*}\hat{\psi}\,, \tag{2.59}$$

$$\hat{\psi}''' = 0\,. \tag{2.60}$$

In general, terms $\propto \mathrm{Re}$ and $\propto \mathrm{Ka}$ must not be omitted when no information about the Reynolds number and the Kapitza number is given. If they were sufficiently large or even infinite, the corresponding terms must be taken into account in the equations. However, since in the present experiments both quantities were finite, they were also assumed finite in the calculations and the terms $\propto \mathrm{Re}$ and $\propto \mathrm{Ka}$ could be omitted.

The only non-trivial solution of this problem is $\hat{\psi}_0 = y^{*2}$. As mentioned above, the prefactor cannot be determined and is therefore omitted. The corresponding eigenvalue is $c_0^* = 2$. One can see that the phase velocity has no imaginary part and thus the perturbation neither growths nor decays. The temporal growth rate is $b_\mathrm{t}^* = 0$. This result can be interpreted physically: In the case of $k^* \to 0$, the system is perturbed by infinite long waves. These waves cannot grow (nor decay) since this would lead to an infinite volume flux between the wave crest and the wave trough, which is physically not possible.

The real part of c_0^*, however, shows that the dimensioned phase velocity of infinite long waves is two times the surface velocity:

$$c(k \to 0) = 2\,U_\mathrm{surf}\,. \tag{2.61}$$

Long wave approximation (first order)

For the first order long wave approximation all terms of order k^{*2} and higher are omitted in eqs. (2.49) through (2.53). The Reynolds number and the Kapitza number again are assumed finite.

$$0 \le y^* \le 1: \qquad \hat{\psi}'''' = \mathrm{i}k^*\mathrm{Re}\left[(U^* - c^*)\hat{\psi}'' - U^{*\prime\prime}\hat{\psi}\right], \tag{2.62}$$

$$y^* = 0: \qquad \hat{\psi} = 0, \tag{2.63}$$

$$\hat{\psi}' = 0, \tag{2.64}$$

$$y^* = 1: \qquad \hat{\psi}'' = -\frac{2}{1-c^*}\hat{\psi}, \tag{2.65}$$

$$\hat{\psi}''' = \mathrm{i}k^*\mathrm{Re}\,(1-c^*)\,\hat{\psi}' - \frac{\mathrm{i}k^*}{1-c^*}\frac{2}{\tan\alpha}\hat{\psi}. \tag{2.66}$$

The solution of this first order approximation has to be similar to the solution of the zeroth order approximation, therefore an ansatz in form of $\hat{\psi} = \hat{\psi}_0 + \hat{\psi}_1$ and $c^* = c_0^* + c_1^*$ with $\hat{\psi}_1$ and c_1^* being of order k^* was chosen. $\hat{\psi}$ and c^* were put in eqs. (2.62) through (2.66) and U^*, $\hat{\psi}_0$ and c_0^* were substituted. After omitting terms of order k^{*2} one gets the set of equations

$$0 \le y^* \le 1: \qquad \hat{\psi}_1'''' = 4\mathrm{i}k^*\mathrm{Re}\,(y^* - 1), \tag{2.67}$$

$$y^* = 0: \qquad \hat{\psi}_1 = 0, \tag{2.68}$$

$$\hat{\psi}_1' = 0, \tag{2.69}$$

$$y^* = 1: \qquad \hat{\psi}_1'' = 2\hat{\psi}_1 - 2c_1^*, \tag{2.70}$$

$$\hat{\psi}_1''' = 2\mathrm{i}k^*\left(\frac{1}{\tan\alpha} - \mathrm{Re}\right). \tag{2.71}$$

From this set of equations one can derive the eigenvalue

$$c_1^* = \mathrm{i}k^*\left(\frac{8}{15}\mathrm{Re} - \frac{2}{3\tan\alpha}\right). \tag{2.72}$$

The stream function $\hat{\psi}_1$ could also be derived, but for the sake of the stability analysis only the phase velocity is needed. The complex phase velocity is now

$$c^* = c_0^* + c_1^* = 2 + \mathrm{i}k^*\left(\frac{8}{15}\mathrm{Re} - \frac{2}{3\tan\alpha}\right). \tag{2.73}$$

Now an imaginary part of c^* and therefore an information about the stability of the system is given. The temporal growth rate is

$$b_\mathrm{t}^* = \Im(c^*)k^* = k^{*2}\left(\frac{8}{15}\mathrm{Re} - \frac{2}{3\tan\alpha}\right). \tag{2.74}$$

In fig. 2.3(a) the temporal growth rate b_t^* is shown as a function of k^* for three different Reynolds numbers at a fixed angle α. The dashed lines indicate the analytically calculated growth rate

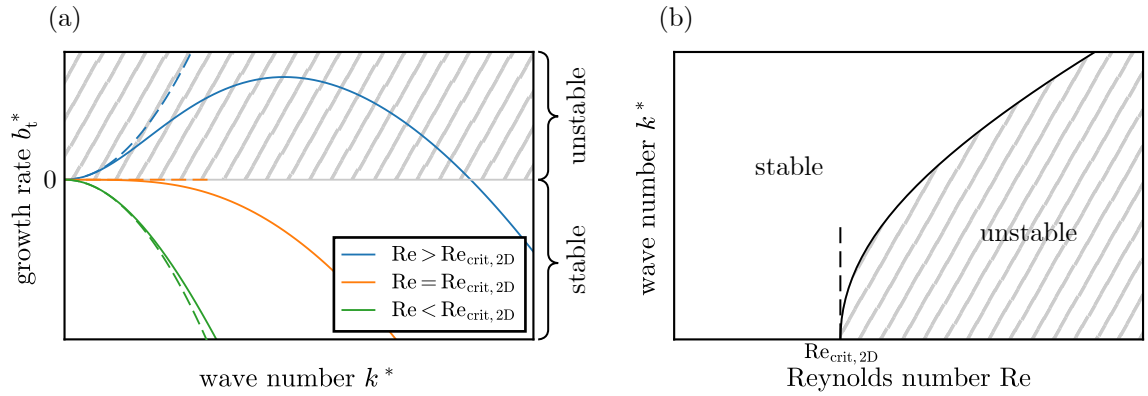

Figure 2.3: (a) Temporal growth rate b_t^* of the wave as function of the wavenumber k^* for a subcritical, critical and supercritical Reynolds number Re. (b) Corresponding stability chart. In both subfigures the inclination angle α is kept constant. The solid lines are obtained using a numerical approach described in section 2.4. The dashed lines are a result of the analytical calculations for $k^* \to 0$.

from eq. (2.74). The solid lines show the solution of the full Orr–Sommerfeld equation using a numerical approach described in section 2.4.

A quantity of major interest is the *critical Reynolds number* $\mathrm{Re}_{\mathrm{crit,2D}}$ where the system transitions from stable to unstable. At this point the growth rate has to be zero: $b_t^* = 0$. This leads to the critical Reynolds number

$$\mathrm{Re}_{\mathrm{crit,2D}} = \frac{5}{4\tan\alpha} = \frac{5}{4}\cot\alpha \tag{2.75}$$

for infinite long waves. Fig. 2.3(b) shows the stability chart of the flow for a fixed inclination angle. The critical Reynolds number $\mathrm{Re}_{\mathrm{crit,2D}}$ is marked in the figure. The stable and unstable areas are divided by the neutral curve. Eq. (2.75) shows that $\mathrm{Re}_{\mathrm{crit,2D}}$ is independent of k^* (in the first order), therefore the neutral curve in fig 2.3(b) has an infinite slope at $\mathrm{Re}_{\mathrm{crit,2D}}$.

In this thesis only the zeroth and first order long wave approximations of the Orr–Sommerfeld equation were executed. Higher order approximations can be found, e.g., in the book of Chang and Demekhin [37]. However, since it is possible to obtain the solution of the Orr–Sommerfeld equation for the whole parameter space via numerical computation, it is not necessary to evaluate higher order approximations analytically. The results of this section are nevertheless important since they provide a good starting estimation for the numerical calculations which will be presented in the following section.

2.4 Numerical solution for the full parameter space

As mentioned above, an analytic solution of the Orr–Sommerfeld equation with the corresponding boundary conditions can only be found for small wave numbers. With a numerical approach it is possible to find a solution for the whole parameter space. Since in this work mainly the spatial instability of the film flow is investigated, only the calculation of the spatial growth rate is shown here (see eq. (2.55)). To this end, the fourth order Orr–Sommerfeld equation (2.49) has to be rewritten as a set of first order differential equations. The derivations of the stream function $\hat{\psi}$ are denoted as $\vec{\Psi}$ with $\Psi_0 = \hat{\psi}, \Psi_1 = \hat{\psi}', \Psi_2 = \hat{\psi}''$ and $\Psi_3 = \hat{\psi}'''$. For the calculation of the spatial growth rate, the phase velocity c^* is replaced by ω^*/k^*.

$$\begin{aligned}
\Psi_0' &= \Psi_1 \,, \\
\Psi_1' &= \Psi_2 \,, \\
\Psi_2' &= \Psi_3 \,, \\
\Psi_3' &= 2k^{*2}\Psi_2 - k^{*4}\Psi_0 + \mathrm{i}k^*\mathrm{Re}\left[(U^* - \frac{\omega^*}{k^*})\left(\Psi_2 - k^{*2}\Psi_0\right) - U^{*\prime\prime}\Psi_0\right] .
\end{aligned} \tag{2.76}$$

The boundary conditions at $y^* = 0$ are denoted as

$$\vec{F}_0\left(\vec{\Psi}\right) = \begin{pmatrix} \Psi_0 \\ \Psi_1 \end{pmatrix} = \vec{0} \tag{2.77}$$

and the boundary conditions at $y^* = 1$ as

$$\vec{F}_1\left(\vec{\Psi}, k^*\right) = \begin{pmatrix} \Psi_2 + \left(k^{*2} + \dfrac{2}{1 - \frac{\omega^*}{k^*}}\right)\Psi_0 \\ \Psi_3 - \left[3k^{*2} + \mathrm{i}k^*\mathrm{Re}\left(1 - \dfrac{\omega^*}{k^*}\right)\right]\Psi_1 + \\ \qquad + \dfrac{\mathrm{i}k^*}{1 - \frac{\omega^*}{k^*}}\left[\dfrac{2}{\tan\alpha} + k^{*2}\mathrm{Ka}\left(\dfrac{2}{\mathrm{Re}^2\sin\alpha}\right)^{\frac{1}{3}}\right]\Psi_0 \end{pmatrix} = \vec{0}\,. \tag{2.78}$$

For the solution of eq. (2.76) a numerical shooting method was used. Starting at $y^* = 0$ the values for Ψ_0 and Ψ_1 are given by the boundary condition (2.77). One of the two terms Ψ_2 and Ψ_3 can be chosen arbitrarily since the prefactor of the solution $\vec{\Psi}$ cannot be determined Here $\Psi_2(y^* = 0) = 1$ w.l.o.g. The starting value of Ψ_3 as well as k^* has to be guessed. The integration from $y^* = 0$ to $y^* = 1$ is done using a Runge-Kutta method. The so obtained values of $\vec{\Psi}$ at $y^* = 1$ are substituted into the boundary condition (2.78) which generally is not fulfilled. The guessed values $\Psi_3(y^* = 0)$ and k^* are varied using Newton's method until $\left|\vec{F}_1\left(\vec{\Psi}, k^*\right)\right|$ is below 10^{-5}.

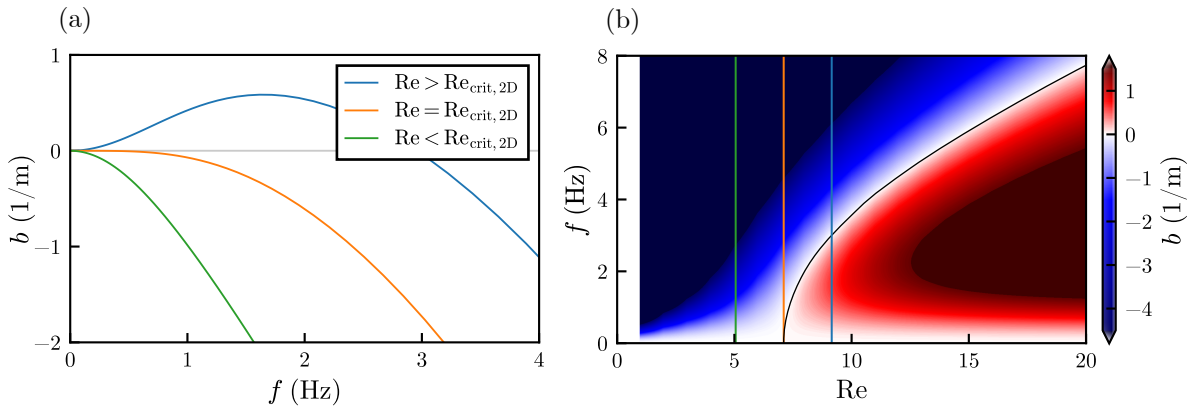

Figure 2.4: (a) Spatial growth rate b as a function of the wave frequency f for a subcritical, critical and supercritical Reynolds number. (b) Stability chart of the two dimensional film flow. The growth rate b is color coded. The solid black line marks the neutral curve $b = 0$. The vertical solid lines denote the Reynolds number used in (a). In both (a) and (b) the inclination angle was $\alpha = 10°$ and the Kapitza number was $\mathrm{Ka} = 1.32$.

From the so obtained eigenvalue $k^* = k_\mathrm{r}^* + \mathrm{i}k_\mathrm{i}^*$ one can derive the spatial growth rate b_s^*, the wavelength λ^* and the phase velocity c^*

$$b_\mathrm{s}^* = -k_\mathrm{i}^* \,, \tag{2.79}$$

$$\lambda^* = \frac{2\pi}{k_\mathrm{r}^*} \,, \tag{2.80}$$

$$c^* = \frac{\omega^*}{k_\mathrm{r}^*} \,, \tag{2.81}$$

as well as their dimensioned values

$$b = \frac{b_\mathrm{s}^*}{H} \,, \tag{2.82}$$

$$\lambda = \lambda^* H \,, \tag{2.83}$$

$$c = c^* U_\mathrm{surf} \,. \tag{2.84}$$

Since in the experiments the frequency f is used instead the angular frequency ω^*, f has to be calculated via

$$f = \omega^* \frac{U_\mathrm{surf}}{2\pi H} \,. \tag{2.85}$$

Fig. 2.4 illustrates the results of the numerical calculations. Fig. 2.4(a) shows the dimensioned spatial growth rate b as a function of the frequency f for a subcritical, critical and supercritical Reynolds number Re (see also fig. 2.3). The whole stability chart is shown in fig. 2.4(b), where the growth rate b is color coded: In the blue area b is negative and the flow is stable, in the red area b is positive and the flow is unstable. The neutral curve is marked by the solid black line. The three vertical colored lines show the three Reynolds numbers used in fig. 2.4(a).

3 Studied system and measurement methods

3.1 Studied system

In the following section the studied system will be presented. This includes the flow facilities in general, a detailed description of the side walls used in the channels, the properties of the fluids and the properties of the used tracer particles. The content of this section is based on the publications [62, 63].

3.1.1 Flow facilities

The experimental setup is schematically shown in Fig. 3.1. The measurements were carried out in a channel with a flat substrate of aluminum and flat side walls of acrylic glass (PMMA). Two movable aluminum side walls could be placed within the channel in order to change the channel width B (see section 3.1.3 for a detailed description of the side walls). The whole channel could be tilted by an angle α and was mounted on a vibration isolating table to reduce parasitic vibrations from the surroundings (mainly the pump and thermostat).

The fluid was pumped by an eccentric pump from the reservoir to the channel inlet through flexible hoses. Due to the flexibility of the hoses, pressure surges produced by the pump were partially damped. A non-inversive flow meter type *Deltawave C* from *Systec controls* was mounted on a stiff pvc pipe. The adjustable bypass had multiple advantages for the system: First, pressure surges from the pump could partially escape through the bypass—similar to a

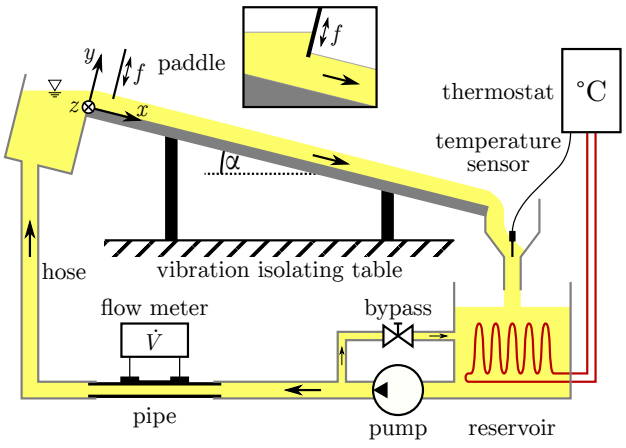

Figure 3.1: Schematic plot of the experimental system. © Springer Nature

surge tank [64]—and therefore had a smaller impact on the fluid within the channel. Second, the volume flux $\dot{V}$ could be adjusted more precisely and third, it was possible to set the same volume flux with different pumping capacities. The latter was necessary to investigate measurement artifacts (e.g. parasitic frequencies) produced by the pump. An inflow tank was installed at the inlet of the channel to calm the fluid and allow a steady inflow into the channel. An optional paddle could be installed that was permanently dipped into the fluid surface (see the inlay of Fig. 3.1) and oscillated periodically with frequency f and amplitude A. With the use of the paddle, the volume flux $\dot{V}$ could be varied periodically which lead to sinusoidal surface waves with frequency f that evolved downstream along the channel. The paddle was driven by a linear motor type *PS01-23x160H* from *LinMot*. At the end of the channel, the fluid flowed back into the reservoir and passed a temperature sensor. A thermostat kept the fluid at a fixed temperature T. The pumps and the thermostats varied from channel to channel, please see section 3.1.5 for further information.

The x-axis was set to be along the channel in streamwise direction, whereas the y-axis was set to be perpendicular to the bottom (see also fig. 2.1). For the three-dimensional channel, an additional z-axis is introduced that points in spanwise direction, as illustrated in fig. 3.1.

Experiments were performed at three inclination angles $\alpha = 5^\circ, 10^\circ$ and 15° ($\pm 0.1^\circ$). The channel width B was varied from 84 mm up to 255 mm (± 0.5 mm). The excitation frequency f ranges from 1 Hz to 15 Hz (± 0.01 Hz) and the Reynolds number Re (see the following section) from 5 to 60 (± 0.5).

3.1.2 Definition of the Reynolds number

The definition of the Reynolds number Re is given by eq. (2.10) for a two-dimensional system. In the three-dimensional channel flow, side walls affect the velocity profile that in result varies with the position within the channel. The velocity profile in the center of the channel is nearly constant, but in the vicinity of the side walls, the fluid is slowed down due to the no-slip condition. The effect of the capillary elevation at the side walls will be neglected, since in the experimental system the film thickness is much larger than the capillary elevation [13, 21] and the Kapitza number is sufficiently low [52]. The velocity profile of the channel flow can therefore be described by the flow through a pipe with rectangular cross section [65]. The surface of the film flow is the symmetry plane of the corresponding pipe flow. An exemplary velocity field is shown in fig. 3.2.

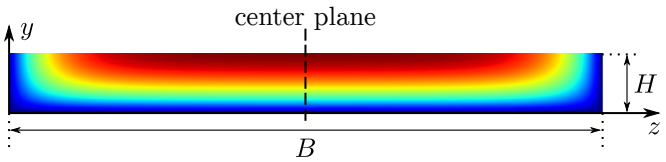

Figure 3.2: Exemplary cross sectional velocity field of a channel flow with no-slip condition at the side walls. The velocity is color coded from blue (slow) to red (fast). The channel width is denoted as B and the film thickness as H. The center of the channel is shown by the dashed line.

The Reynolds number of the fully developed channel flow is defined by

$$\mathrm{Re} = \frac{U_{\mathrm{surf,center}} H}{\nu}\,, \tag{3.1}$$

where $U_{\mathrm{surf,center}}$ is the surface velocity in the center of the channel at $z = B/2$, H is the film thickness and ν the kinematic viscosity. Both $U_{\mathrm{surf,center}}$ and H are a priori unknown, but can be calculated from the measured volume flux $\dot{V}$. To this end, the following equation describing the volume flux as a function of the film thickness is used [65]:

$$\dot{V} = \frac{g \sin\alpha}{\nu} H^3 B \left(\frac{1}{3} - \frac{128}{\pi^5} \frac{H}{B} \sum_{n=1}^{\infty} \frac{\tanh\left(m \frac{B}{H}\right)}{(2n-1)^5} \right) \quad \text{with} \quad m = \frac{\pi}{4}(2n-1)\,. \tag{3.2}$$

To calculate the film thickness H from the volume flux $\dot{V}$, one has to numerically solve eq. (3.2) for H. Since the elements of the series become rapidly smaller for larger n (about $\mathcal{O}\left(n^{-5}\right)$) the series is only calculated up to 10 elements.

The surface velocity at the center of the channel can be calculated via [65]

$$U_{\mathrm{surf,center}} = \frac{g \sin\alpha}{2\nu} H^2 \left(1 + \underbrace{\frac{1}{2} \sum_{n=1}^{\infty} \frac{(-1)^n}{m^3 \cosh\left(m \frac{B}{H}\right)}}_{S} \right) \quad \text{with} \quad m = \frac{\pi}{4}(2n-1)\,. \tag{3.3}$$

The only difference between the surface velocity of a plane flow (see eq. (2.5)) and the surface velocity of the channel flow is given by the term denoted as S in eq. (3.3). For thin films or wide channels ($B/H \gg 1$) this term vanishes. In fact, for all parameter combinations used in the experiments, the term S can be neglected: $S < 10^{-6} \ll 1$. The surface velocity in the center of the channel therefore is

$$U_{\mathrm{surf,center}} = \frac{g \sin\alpha}{2\nu} H^2\,. \tag{3.4}$$

The Reynolds number (eq. (3.1)) can therefore be calculated via

$$\mathrm{Re} = \frac{g \sin\alpha}{2\nu^2} H^3 \tag{3.5}$$

using the numerically calculated film thickness H.

To summarize this section, the influence of the side walls has to be taken into account calculating the film thickness from the volume flux. The flow profile in the center of the channel, however, is not affected by the presence of the side walls, at least for the film thicknesses and channel widths used in the experiments. The assumption of a parabolic velocity profile—as in the two-dimensional case—is valid for the central area of the channel.

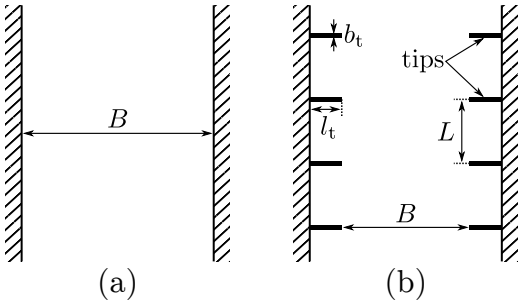

Figure 3.3: Geometric dimensions of the channel (top view) for (a) flat and (b) corrugated side walls. The main flow direction is from top to bottom. © AIP Publishing, Springer Nature

3.1.3 Side wall configurations

The movable inner side walls of the channel could either be flat or corrugated. In the "flat" case, the channel width B is simply defined as the distance between the two side walls (see fig. 3.3(a), for a three dimensional sketch of the full channel see fig. 3.8). In the "corrugated" case, vertical tips were attached to the side walls perpendicular to the bottom (see figs. 3.3(b), 3.7). The geometric dimensions of the tips were constant for all experiments: $b_t = 1\,\text{mm}$ and $l_t = 8\,\text{mm}$. The height of the tips was the same as the height of the side walls and therefore much larger than the film thickness. The streamwise length scale of the corrugations is given by the distance of two consecutive tips. It is denoted as L and was varied in the experiments. For all measurements, the opposing tips of the two side walls were placed symmetrically. The channel width B of the corrugated system is defined as the distance between two opposing tips (see fig. 3.3(b)).

For the flow in a channel with corrugated side walls, the definition of the Reynolds number is not unambiguous, since multiple geometric lengths appear in the system. However, for a reasonable comparison the same definition of the Reynolds number as for the "flat" system (see eq. (2.10)) is used. The channel width B for channels with corrugated side walls is defined as stated above.

3.1.4 Fluid properties

Two different fluids were used in the experiments. Both were mixtures of the highly viscous silicone oils *Elbesil 50* and *Elbesil 200* from *Elbesil* and had similar densities and surface tensions but differed significantly in their viscosity. The fluid mixtures are denoted as *Elbesil 140* and *Elbesil 100*, according to their viscosity. Their physical properties are given in tab. 3.1. The kinematic viscosity ν and the density ρ was measured with an Ubbelohde capillary viscosimeter

Table 3.1: Fluid properties.

Notation	ρ (kg/m^3)	η (mPas)	ν (mm^2/s)	σ (mN/m)	Ka	T (°C)
Elbesil 140	962.7 ± 0.4	136.7 ± 0.5	142.0 ± 0.5	20.25 ± 0.11	1.32 ± 0.01	24.0 ± 0.1
Elbesil 100	964.9 ± 0.4	99.4 ± 0.5	103.0 ± 0.5	20.14 ± 0.07	2.02 ± 0.01	23.0 ± 0.1

Table 3.2: Properties of different channels.

channel number	length (m)	maximum width (mm)	silicone oil	pump	thermostat
1	2.0	255	*Elbesil 140*	*AFJ 40.1B*	*TC300*
2	1.4	170	*Elbesil 140*	*SK90L/4*	*N6*
3	2.0	170	*Elbesil 100*	2×*AFJ 15.1B* (parallel)	*TC300*

from *Schott* and with a Mohr–Westphal balance from *Kern*, respectively. The dynamic viscosity η was calculated by $\eta = \nu\rho$. The measurement of the surface tension σ was performed with a ring tensiometer type *TE1CA-M* from *Lauda*. The Kapitza number Ka is given by eq. (2.47). The temperature T at which the measurements of the fluid properties were performed is given in tab. 3.1. The actual experiments in the channels were carried out at the same temperature.

3.1.5 Properties of different channels

To eliminate measurement artifacts produced by the setup, measurements were performed in three different channels with different peripherals. The dimensions of the channels and the used silicone oil, pump, and thermostat are given in table 3.2. All pumps were from *Johstadt* and all thermostats were from *Haake*. It is noteworthy that all three setups had different pipe systems (i.e. different diameters and lengths) in order to identify any resonances that may occur. It was possible to verify the experimental outcome from channel 1 by repeating the measurement in channel 2 with the same system parameters.

3.2 Measurement methods of the basic flow

This section deals with the description of the measurement methods of the basic flow, i.e. the channel flow without excited surface waves. To this end, the paddle at the inlet of the channel was removed and no artificial waves were generated. In general, the basic flow can only exist if the flow is stable. But since the experimental setup is well insulated against external vibrations, the spontaneously emerging waves in the unstable regime are very small. Thus the measurement of the basic flow is not visibly affected by the appearance of surface waves.

3.2.1 Film thickness

The measurement of the film thickness h of the basic flow was performed with the setup shown in fig. 3.4(a). A precision gage type *Millitast 1083* from *Mahr* was mounted perpendicular to the channel bottom. After calibrating the instrument to the bottom level, its tip was carefully lowered manually using a screw with fine-pitch thread. The touch down to the surface was indicated by a sudden capillary elevation of the fluid at the tip (see fig. 3.4(b) and (c)). The measurements were performed in the center of the channel at different streamwise positions. With this measurement method, a precision of 30 µm was achieved.

3.2.2 Tracer particles

Tracer particles are necessary for different measurement methods. For the PIV measurement of the velocity profile (see section 3.2.3) hollow glass spheres type *80A601* from *Dantec* were seeded into the fluid. The mean density of the particles was $\rho_P = 2230\,\mathrm{kg/m^3}$, according to the manufacturer. The particle size distribution was measured with the *Mastersizer 2000* laser diffraction particle size analyzer from *Malvern Instruments* (see fig. 3.5). The median particle size was $d_P = 9.6\,\mu\mathrm{m}$. For PIV measurements it is necessary that the individual particles follow the flow properly. This is the case if the particles are much smaller than the geometric lengths in the system and if the particles do not sediment. The sedimentation speed of spherical particles with diameter d_P is given by $u_{sed} = d_P^2 g(\rho_P - \rho)/(18\eta)$ with the fluid's density ρ and viscosity η [66]. For the used silicone oils (see tab. 3.1) the typical sedimentation speeds are $4.7 \cdot 10^{-7}\,\mathrm{m/s}$ respectively $6.4 \cdot 10^{-7}\,\mathrm{m/s}$ and therefore several orders of magnitude smaller than the typical flow velocities in the experiments. A sedimentation effect can therefore be neglected.

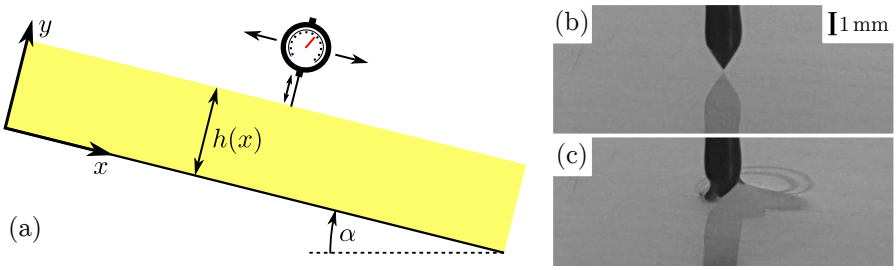

Figure 3.4: (a) Setup for measurements of the film thickness. (b) Image of the tip before and (c) after touching the fluid surface.

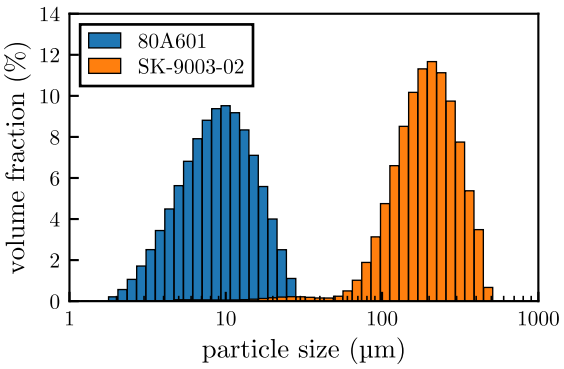

Figure 3.5: Weighted particle size distributions of (left) the tracer particles Type *80A601*, used for the PIV measurements and (right) the tracer particles type *SK-9003-02*, used for the measurement of the surface velocity.

For the measurement of the surface velocity profile (see section 3.2.4) larger particles were needed that also float on the fluid surface. To this end, hollow glass spheres type *SK-9003-02* from *S u. K Hock GmbH* were used. The weighted particle size distribution is shown in fig. 3.5. The median particle size is $d_\mathrm{P} = 210\,\mu\mathrm{m}$. The mean density of the particles is $\rho_\mathrm{P} = (630 \pm 30)\,\mathrm{kg/m^3}$ and therefore less than the fluid density. Thus the particles remain at the fluid surface.

3.2.3 Velocity profile

The steady state velocity field in the center plane of the channel was measured with a particle image velocimetry (PIV) setup that is shown in fig. 3.6. For this purpose the fluid was seeded with tracer particles type *80A601* from *Dantec* (see section 3.2.2). A 100 mW continuous wave laser type *FP-MVmicro-660-100-10-F* from *Laser Components* with a wavelength of 660 nm illuminated the center plane of the channel. The streamwise extent of the laser sheet was $\sim 20\,\mathrm{mm}$ but may have varied from experiment to experiment. The width of the laser sheet was $\lesssim 0.5\,\mathrm{mm}$. As shown in fig. 3.6(a) a high speed camera *Optronis CR600x2* was mounted next to the channel. Its direction of view was perpendicular to the transparent side walls. If necessary, the camera could be tilted for a better view. The resulting distortions could be corrected by calibration.

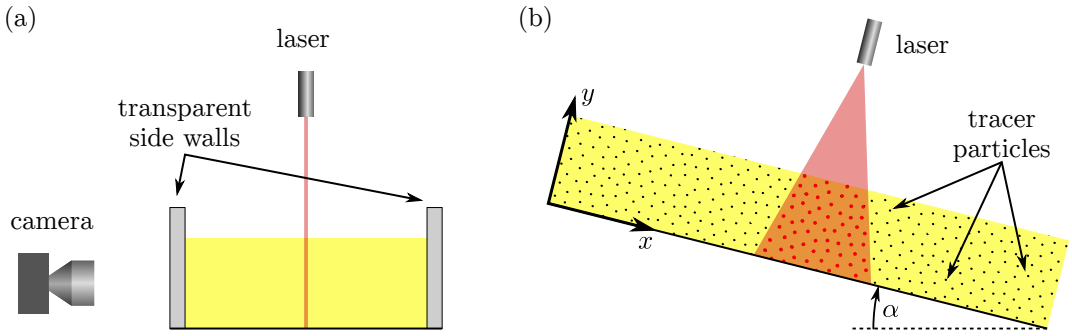

Figure 3.6: Setup for Particle Image Velocimetry (PIV). (a) Streamwise view, (b) camera perspective.

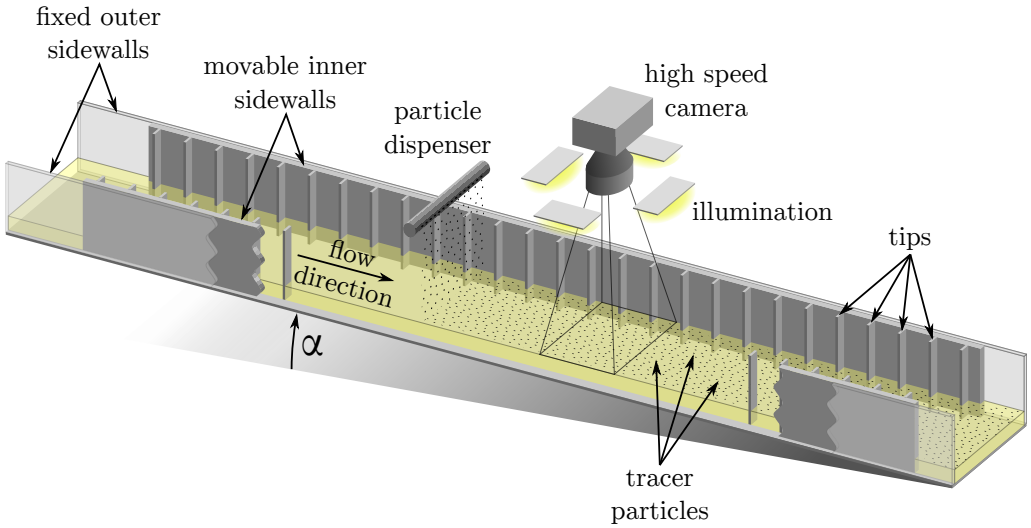

Figure 3.7: Experimental setup for measurements of the surface velocity. Here the side walls are shown with attached tips (see fig. 3.3). © AIP Publishing.

In the following, a short overview of the functionality of a PIV setup is given. For a more detailed description, please see the relevant literature, e.g. [67]. In short, two (or more) images of the illuminated fluid section containing seeding particles that scatter the laser light were captured by the camera in a short row. In the present experiments, the camera captured multiple frames with a frame rate of 500 fps and an exposure time of 0.5 ms. From the displacement of the particle positions in the two frames the velocity field could be calculated. The image analysis was done with the open source *MATLAB* application *PIVlab* [68, 69]. All frames were split up into smaller interrogation windows that eventually overlap. The corresponding windows of two consecutive frames were cross correlated to obtain the mean displacement vector of the particles in the specific window from one frame to the other. With the help of a calibration plate, the displacement could be converted into real-world coordinates. The flow field finally could be calculated from the displacement vectors and the frame rate of the camera. For a more reliable result, this procedure was repeated for at least 200 consecutive image pairs and the resulting flow fields were averaged.

For a reliable PIV measurement the particles had to be much smaller than the size of the interrogation window. With a typical window size of $\sim 500-1000\,\mu m$ and a particle size of $\sim 10\,\mu m$, this requirement was met.

3.2.4 Surface flow field

The description of the measurement technique of the surface flow field is based on the publication [62].

For the measurement of the surface velocity of the basic flow a particle tracking method as shown in fig. 3.7 was used. A particle dispenser scattered hollow glass spheres (type *SK-9003-02*, see section 3.2.2) on top of the oil film. The particles were less dense than the fluid and

remained on the surface. Before the fluid flowed back into the reservoir, the particles were filtered out. With the diameter much smaller than the film thickness and other geometric lengths the particles followed the surface velocity field. Only the close vicinity of the side walls could not be observed with this technique. This had two reasons: First, the finite particle size is no longer smaller than the distance to the side walls. And second, the capillary elevation at the vertical walls leads to a rise of the floating particles that therefore do not follow the streamlines properly. On top of the channel a high speed camera *Optronis CR600x2* was mounted. To reduce the shadows of the particles on the bottom of the channel, four areal LEDs were used as illumination and placed around the camera. The surface was recorded with a frame rate up to 500 fps, adapted to the surface velocity, and a resolution of $1024\,\mathrm{px} \times 1280\,\mathrm{px}$. This results in a spatial resolution of $\sim 100\,\mu\mathrm{m/px}$. For one measurement $500 - 1000$ frames were taken with about $200 - 1000$ particles in every frame. Before performing the measurement the position of the camera was adjusted, so that the distance between camera and surface remained constant.

The data was post-processed with a single particle tracking method based on the Crocker-Grier algorithm [70] implemented in the Python module *trackpy* [71]. To summarize the procedure shortly, first the individual particles in every frame were localized with sub-pixel accuracy. Afterwards the particle coordinates of subsequent frames were linked into trajectories. With the help of a calibration plate, the conversion in real-world coordinates could be done. With this method one could obtain not only the trajectories but also the velocity of the corresponding particles.

For acquiring the velocity field, the recorded surface was divided into bins of size $15\,\mathrm{px} \times 15\,\mathrm{px}$. The velocities of all particles crossing each bin were averaged and major outliers were removed by Grubb's test for outliers [72]. The resulting grid finally could be linearly interpolated in order to obtain a smooth velocity field.

3.3 Measurement methods of the wave properties

The following section deals with the measurement techniques concerning the properties of the artificial waves excited by the paddle in the inflow of the channel. The content of this section is based on the publications [62, 63].

3.3.1 Growth rate and linear stability

To measure the linear stability of the flow and particularly the linear growth rate b of the excited waves, a similar setup as in previous works was used [38, 43–45, 53, 73–75]. Fig. 3.8 gives a three dimensional view of the channel. Within the symmetry plane of the channel two parallel laser beams were reflected at the fluid surface and projected onto the screen. As lasers, the diode lasers *FP-D-635-5-C-F* from *Laser Components* were used. A misleading reflection at the bottom of the channel could not be observed. A sinusoidal wave with frequency f, excited by the paddle, caused an oscillation of the laser spots on the screen with the same frequency:

$$A_1(t) = A_1^0 \sin(2\pi f t - \varphi_1)\,, \qquad A_2(t) = A_2^0 \sin(2\pi f t - \varphi_2)\,. \tag{3.6}$$

The terms A_1^0 and A_2^0 denote the amplitudes of the signals, whereas φ_1 and φ_2 denote arbitrary phases at $t = 0$. The position $x_1 = 600\,\text{mm}$ was large enough to ensure that the measurement was carried out in the fully developed flow (this topic will be discussed in section 4.1). The distance between the two reflection positions $\Delta x = (400 \pm 3)\,\text{mm}$ had to be large enough for a reliable measurement but small enough so the second reflection spot is not affected by the outflow of the channel. The distance from the second spot to the screen x_s varied for different channels. Image stacks were acquired using a CCD camera type *DMK31BU30* from *IC Imaging* with a frame rate of 30 Hz. For each measurement, 600 images were taken.

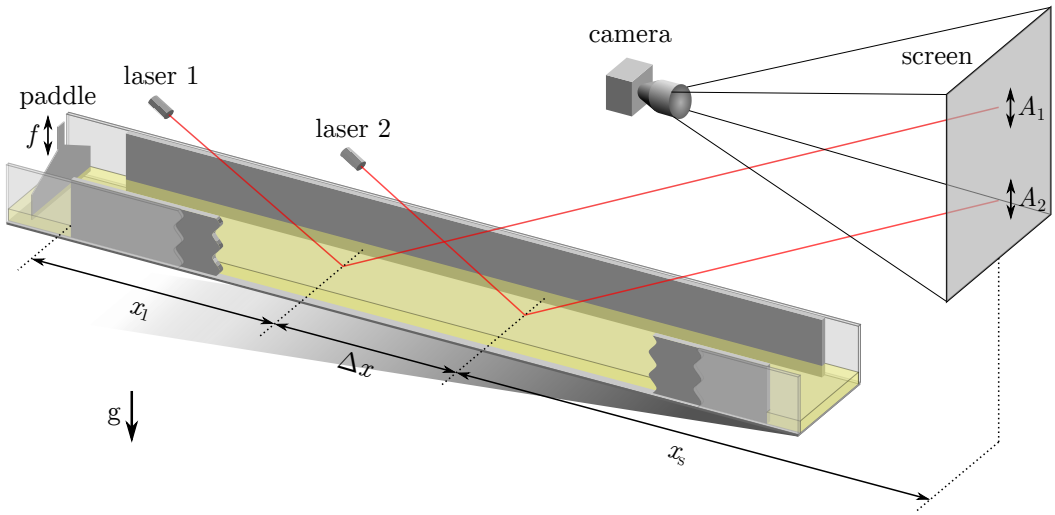

Figure 3.8: Experimental setup for measurements of the linear stability. © AIP Publishing, Springer Nature

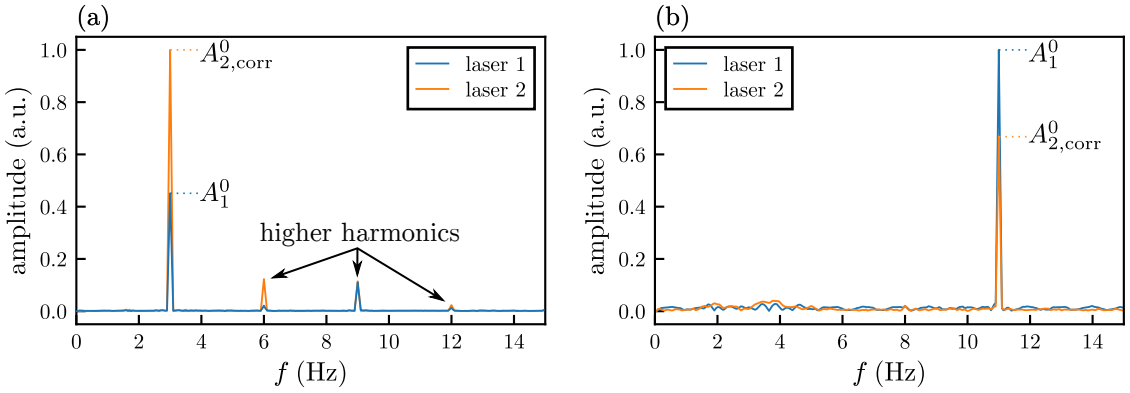

Figure 3.9: Absolute values of the Fourier spectra of the oscillation amplitudes A_1 (laser 1) and A_2 (laser 2) for (a) $f = 3\,\mathrm{Hz}$ and (b) $f = 11\,\mathrm{Hz}$. The spectrum of laser 2 has already been corrected (see eq. (3.7)). The measurements were performed with *Elbesil 100* at $\alpha = 10°$, $B = 129\,\mathrm{mm}$ and $\mathrm{Re} = 25$.

The oscillations of the laser spots are only caused by the oscillation of the surface slope of the fluid at the corresponding reflection positions. An influence of the oscillating film thickness itself could be neglected since the measurements were done in the linear regime where the emerging waves were sufficiently small. The oscillation amplitudes A_1^0 and A_2^0 were proportional to the oscillation amplitude of the surface slope and—since the appearing linear waves were sinusoidal—also proportional to the wave amplitudes at the reflection positions. The oscillation amplitudes A_1^0 and A_2^0 were determined by a Fourier transformation approach: The Fourier spectra of $A_1(t)$ and $A_2(t)$ show a peak at the excitation frequency f as depicted in fig. 3.9. The frame rate of the camera and the number of images taken per measurement were carefully chosen, so that every excitation frequency f used in the experiment matches a frequency in the discrete Fourier spectrum. Therefore the peak is concentrated at this very frequency and the height of this peak represents the oscillation amplitude A_1^0 respectively A_2^0. To calculate the spatial growth rate b, one had to compare the oscillation amplitudes of the two laser spots. As the second laser beam covered a smaller distance between the surface and the screen, its amplitude has to be corrected to compare it with the oscillation amplitude of the first laser:

$$A^0_{2,\mathrm{corr}} = A^0_2 \left(1 + \frac{\Delta x}{x_\mathrm{s}}\right) . \tag{3.7}$$

The amplitudes A_1^0 and $A^0_{2,\mathrm{corr}}$ are shown in fig. 3.9 as the height of the peaks at the excitation frequency f in the two Fourier spectra. The amplitude of the Fourier spectra is given in arbitrary units, since the absolute oscillation amplitude of the laser spots has no practical meaning. The important information is the ratio of A_1^0 and $A^0_{2,\mathrm{corr}}$. In fig. 3.9(a) the amplitude of the wave is increasing in streamwise direction, therefore the flow is *convectively unstable* against perturbations with frequency f. On the other hand, in fig. 3.9(b) the amplitude is decreasing and the flow is *stable*. Fig. 3.9(a) additionally shows the occurrence of higher harmonics, probably caused by small nonlinearities in wave generation. However, since a linear system is assumed in which no coupling of different frequencies occurs, their influence can be neglected.

The spatial growth rate b of the linear free surface wave is given by (cf. eq. (2.55))

$$b = \frac{\ln\left(A^0_{2,\mathrm{corr}}/A^0_1\right)}{\Delta x} . \tag{3.8}$$

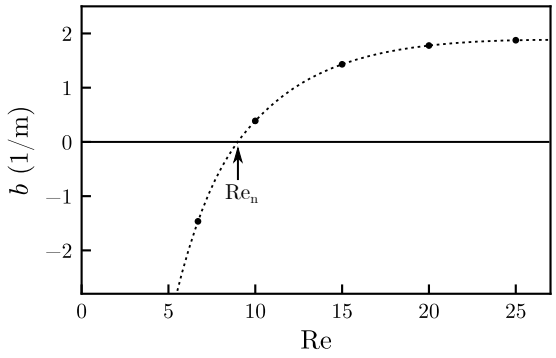

Figure 3.10: Growth rate b as a function of the Reynolds number Re for $f = 3\,\mathrm{Hz}$. The measurements are denoted by the black dots (errorbars are too small to display), the dotted line shows a cubic interpolation. The measurements were performed with *Elbesil 100* at $\alpha = 10°$ and $B = 129\,\mathrm{mm}$.

For $b < 0$, the flow is *stable* against perturbations with frequency f. For $b > 0$, the flow is *convectively unstable*. The neutral point is given by $b = 0$. For a reliable result and a statistic error estimation every measurement was repeated and averaged at least 6 times.

In order to gain information on the stability chart of the system (cf. fig. 2.4(b)), the measurement of the growth rate had to be repeated for multiple frequencies and Reynolds numbers. The data could be linearly interpolated to obtain a smooth chart.

For a more precise determination of the neutral curve, the measured growth rates for a fixed frequency f were interpolated by a cubic spline, shown in fig. 3.10. The root of the growth rate defines the neutral Reynolds number $\mathrm{Re_n}(f)$ that depends on the frequency. This procedure could be repeated for multiple frequencies in order to obtain the full neutral curve.

3.3.2 Wavelength

The measurement of the wavelength of free surface waves could be done with the same setup as the measurement of the linear stability (fig. 3.8). For this purpose one could use the fact that for a sinusoidal wave with frequency f the oscillation of the second laser spot is proportional to the first, but with a time delay Δt:

$$A_2(t) \propto A_1(t - \Delta t)\,. \tag{3.9}$$

To calculate the time delay, the phases φ_1 and φ_2 of the signals $A_1(t)$ and $A_2(t)$ (see eq. (3.6)) were extracted from the Fourier spectrum at the excitation frequency f. The *measured phase difference* $\Delta\varphi_0$ is given by

$$\Delta\varphi_0 = (\varphi_1 - \varphi_2) \bmod 2\pi\,, \quad \Delta\varphi_0 \in [0, 2\pi)\,. \tag{3.10}$$

Because the phases φ_1 and φ_2 are 2π-periodic, also the measured phase difference $\Delta\varphi_0$ is 2π-periodic. The modulo term is necessary so that $\Delta\varphi_0$ is in the range $[0, 2\pi)$. Since in general it is unknown how many full waves lie between the two measurement positions, one cannot directly achieve the *real phase difference* $\Delta\varphi$, which is generally larger than the measured phase difference:

$$\Delta\varphi = \Delta\varphi_0 + 2\pi\, n, \quad n \in \mathbb{N}_0\,, \tag{3.11}$$

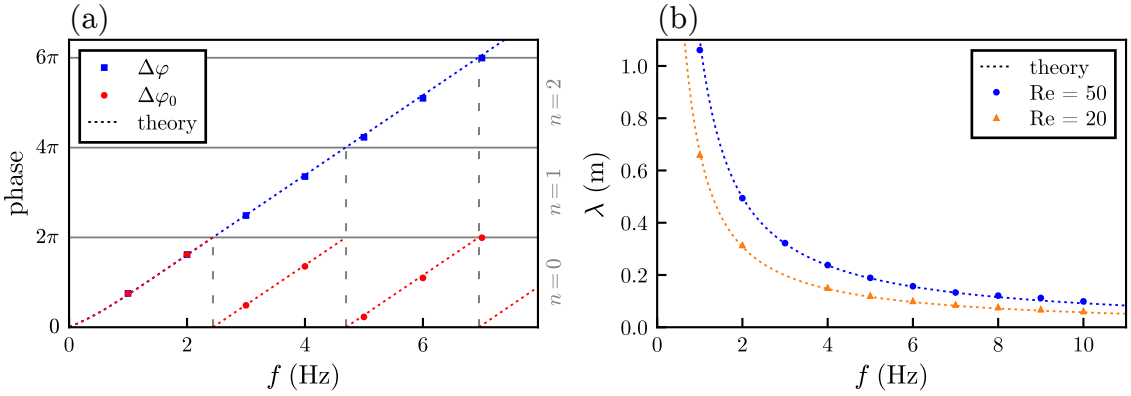

Figure 3.11: (a) Real and measured phase difference $\Delta\varphi$ and $\Delta\varphi_0$, respectively, as a function of the excitation frequency f for $B = 100\,\mathrm{mm}$, $\alpha = 10^\circ$ and $\mathrm{Re} = 50$. The dotted lines show the two-dimensional theoretical predictions. (b) Measured and theoretical wavelength for $B = 100\,\mathrm{mm}$, $\alpha = 10^\circ$ and $\mathrm{Re} = 50$, respectively, $\mathrm{Re} = 20$. The dotted lines show the two-dimensional theoretical predictions. © Springer Nature

where n is the number of full waves between the measurement positions. In order to obtain n, multiple measurements with increasing frequency f were performed. It is expected that the experimental data has to be similar to the theoretical prediction for the wavelength of the plane flow (see section 2). Therefore one can assume the wavelength at $f = 1\,\mathrm{Hz}$ to be much larger than the distance between the measurement positions Δx. In this case n equals 0. With increasing frequency, the real phase difference $\Delta\varphi$ must increase since more and more full waves are in between Δx. Fig. 3.11(a) shows an example of $\Delta\varphi$ and $\Delta\varphi_0$ as well as the theoretical prediction of both as a function of f. When $\Delta\varphi$ exceeds 2π or multiples thereof, one can see a jump down in $\Delta\varphi_0$. If such a jump occurred in the measurement of $\Delta\varphi_0$, n had to be increased for all higher frequencies by one. As one can see, the so obtained values of the real phase difference $\Delta\varphi$ match the theoretical prediction very well.

The time delay Δt can now be derived from the real phase difference:

$$\Delta t = \frac{\Delta\varphi}{2\pi f} = \frac{1}{f}\left(\frac{\Delta\varphi_0}{2\pi} + n\right) . \tag{3.12}$$

From the time delay and the spatial distance between the measurement positions one can calculate the phase velocity

$$c = \frac{\Delta x}{\Delta t} = \frac{\Delta x\ f}{\dfrac{\Delta\varphi_0}{2\pi} + n} \tag{3.13}$$

and finally the wavelength

$$\lambda = \frac{c}{f} = \frac{\Delta x}{\dfrac{\Delta\varphi_0}{2\pi} + n} . \tag{3.14}$$

Fig. 3.11(b) shows an example of the measured and theoretical wavelengths for two different Reynolds numbers. Experiments with different channel widths B, inclination angles α and Reynolds numbers Re were performed. All measurements match the two-dimensional theoretical predictions very well, independent of the system parameters. The small derivations of less

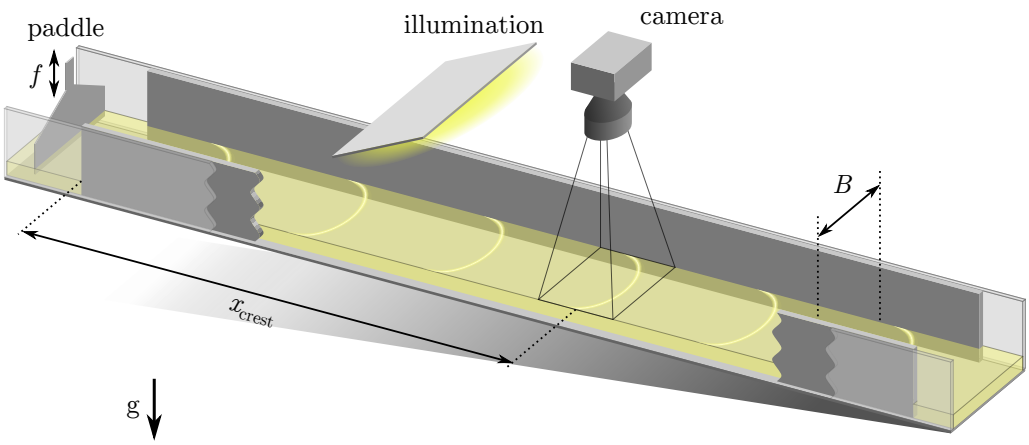

Figure 3.12: Experimental setup for measurements of the wave shape. © Springer Nature

than 3% are mainly caused by the uncertainty of the Reynolds number (see section 3.1.1) and the distance Δx (see section 3.3.1). Hence it is not necessary to measure the wavelength for every experiment. Instead, the calculated wavelength of the plane flow can be used.

3.3.3 Wave shape

For the measurement of the shape of the crest line, the setup shown in Fig. 3.12 was used. On top of the channel a camera type *CR600x2* from *Optronis* was mounted. The measurement position $x_{\text{crest}} = x_1 + \Delta x/2 = 800\,\text{mm}$ was set to be in the middle of the measurement positions for the linear stability (see section 3.3.1). Next to the camera an areal LED panel that illuminated the fluid surface was mounted. The reflection of the light at the part of the surface wave with an appropriate slope was recorded by the camera, see fig. 3.13(a) for an exemplary image. In fact, the recorded bright line is not exactly the crest of the wave, but since only the form of the wave and not the exact position of the crest is interesting, this difference does not matter. After a background image had been subtracted (see fig. 3.13(b)), the crest line could be extracted. To obtain a smooth signal, the brightness along each vertical pixel column in the image was convoluted with a gaussian kernel with a standard deviation of 15 px (see fig. 3.13(c)). The size of the kernel was chosen large enough to obtain a smooth signal but small enough to distort the curve. Afterwards its maximum was localized. The maxima of all pixel columns form the crest line. An example for a detected crest line is given in Fig. 3.13(b). For a reliable measurement, 10 – 30 crest lines were averaged, which also provides an statistic error estimation. After calibrating the result, we obtain the crest line in the form $x(z)$. The spanwise coordinate z originates at the left side of the channel (according to the images taken by the camera, see Fig. 3.13), whereas the origin of the streamwise coordinate x, which is in general at the inlet of the channel, could be chosen arbitrarily, since the streamwise position of the wave within the frame has no practical meaning.

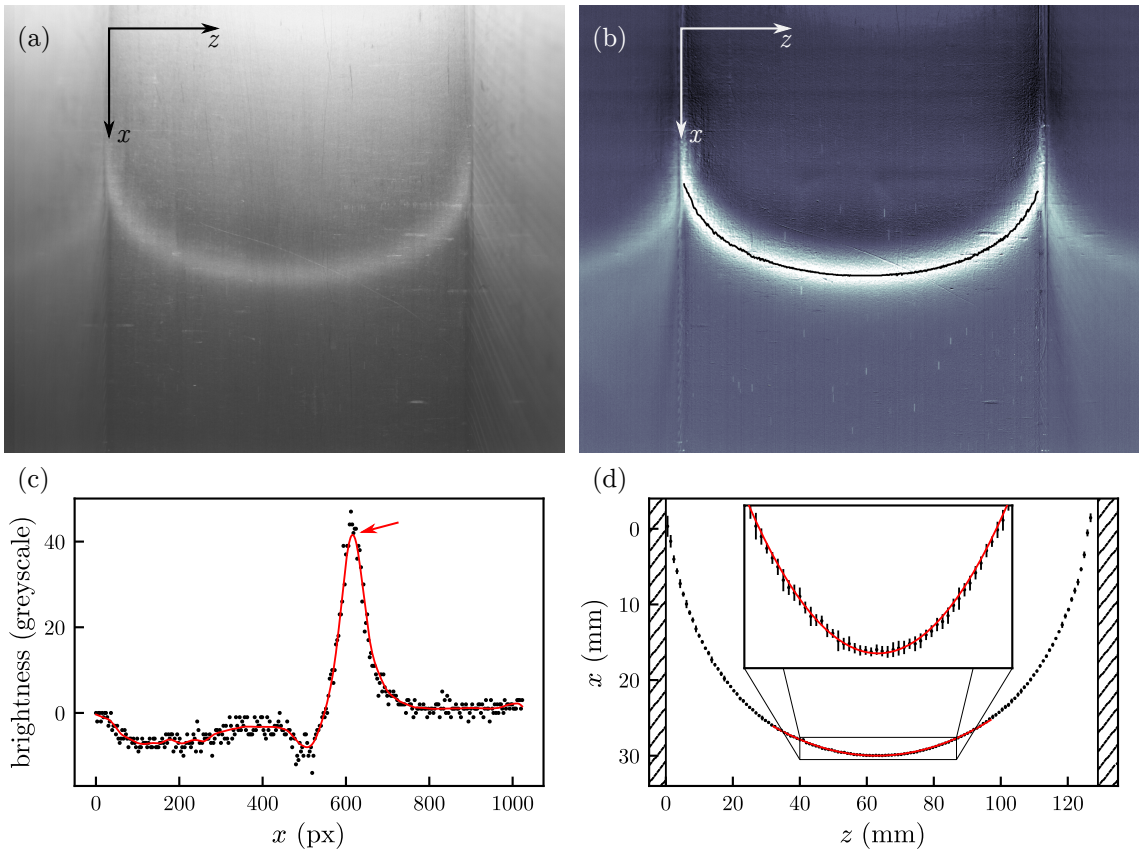

Figure 3.13: (a) Original image of a wave crest. The flow direction is from top to bottom. (b) Background subtracted image with detected crest line shown in black. (c) Brightness of one exemplary pixel column from subfig. (b) (black dots). The red line shows the filtered signal with its maximum denoted by the arrow. (d) Averaged and calibrated crest line positions (black dots, with vertical errorbars) with the quadratic fit given in eq. (3.15) (red line). The hatching at the edges mark the positions of the side walls. All images correspond to the measurement parameters $f = 4\,\mathrm{Hz}$, $B = 129\,\mathrm{mm}, \mathrm{Re} = 40$ and the fluid *Elbesil 140*. © Springer Nature

The center curvature k of the crest line was calculated via a weighted quadratic fit over the center half of the channel ($\frac{1}{4}B < z < \frac{3}{4}B$):

$$x_{\mathrm{fit}}(z) = -\frac{k}{2}\left(z - \frac{B}{2}\right)^2 + a\left(z - \frac{B}{2}\right) + x_0\,, \tag{3.15}$$

where $B/2$ is the center of the channel and k, a and x_0 are the fit parameters. The parameter $a \approx 0$ is necessary to compensate a small potential asymmetry of the wave, whereas x_0 is the arbitrary streamwise position of the wave. A visual example of the averaged crest line, including its statistical errors, and the quadratic fit is given in fig. 3.13(d). The assumption of a parabolic shape of the crest line—at least in the center half of the channel—could be confirmed.

4 Results and discussion

4.1 Inflow effects in a channel

The following section deals with the influence of a finite channel length. There are certain effects at the inflow of the channel that have not been investigated until now. Particularly for the design of coating [1–3] and heat exchanging applications [4, 5] it is necessary to take an undeveloped flow into account. Depending on the specific application, the minimization of the inflow is desirable. Most experimental and theoretical approaches to film flows—particularly the calculations and measurements presented in this thesis—assume a fully developed flow far away from the inflow. Therefore it is necessary to investigate the streamwise length of the inflow area. This section contains measurements of the varying film thickness and surface velocity along the channel. Additionally the full velocity profile directly at the inlet will be presented.

4.1.1 Development of the film thickness

As described in section 3.1, the fluid passes an inflow tank before entering the channel to reduce parasitic vibrations caused by the pump. The fluid surface in the tank is horizontal (regarding to gravity) but afterwards in the channel the surface is tilted by the inclination angle α (see fig. 3.1). The transition from the horizontal to the tilted area does not occur abruptly but smooth. To characterize the transition regime, the film thickness was measured along the center of the channel using the setup presented in section 3.2.1.

The results are displayed in fig. 4.1(a) where the film thickness is shown for several Reynolds numbers. The position $x = 0\,\mathrm{mm}$ marks the upper end of the substrate, that is shown in gray. The film thickness shows three different regimes: A distinct maximum at $x \approx 0\,\mathrm{mm}$ divides the curve into a regime of constant slope on the left and a regime of nearly constant film thickness on the right. The slope on the left marks the horizontal surface (regarding to gravity) in the inflow tank. After passing the transition regime, the film thickness converges to the film thickness of the fully developed flow that is denoted by the arrows at the right side of the figure. As one can see, at low Reynolds numbers the fully developed film thickness is reached after a relatively short distance. For example at $\mathrm{Re} = 10$ the film thickness is constant at $x \gtrsim 20\,\mathrm{mm}$. At higher Reynolds numbers, however, a longer distance is needed to reach the fully developed film thickness.

Fig. 4.1(a) is dominated by the maximum in the film thickness at $x \approx 0\,\mathrm{mm}$. The absolute and relative height maximum becomes larger for higher Reynolds numbers. The occurrence of the

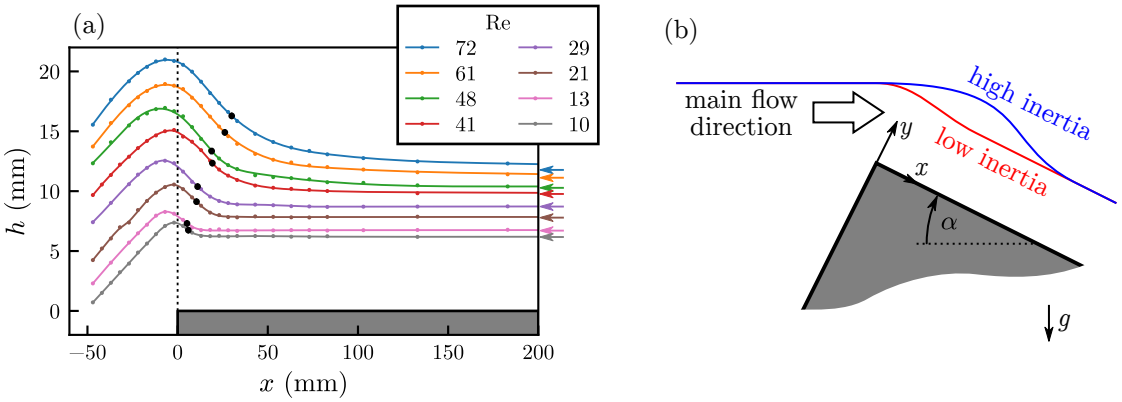

Figure 4.1: (a) Feasured film thickness at $\alpha = 10°$ and different Reynolds numbers. The solid lines are guides to the eye. The arrows at the right edge of the figure show the final film thickness. The inflow length l_{50} is denoted by black dots. The measurements were performed with the fluid *Elbesil 140* at $B = 170\,\text{mm}$. (b) Schematic sketch of the effect of inertia on the local film thickness at the inflow.

maximum can be explained by the fluid's inertia when entering the channel. A sketch of the problem is depicted in fig. 4.1(b). One can assume that the main flow direction is parallel to the free surface due to the lack of friction (this assumption will be confirmed in section 4.1.3). If the inertia of the fluid is relatively high (blue line), the fluid moving along the surface of the inflow tank is not able to follow the abrupt change in the geometry: an *overshoot* occurs. If the inertia is relatively low (red line), this overshoot becomes smaller. In fig. 4.1(b) the fully developed film thickness in both cases was chosen to be the same for a better comparability of the two cases. Experimentally the inertia could be changed for example by changing the viscosity of the fluid. The position at which the maximum in the film thickness occurs shifts to the right when increasing the inertia. However, in the present experiment the viscosity is constant and only the fully developed film thickness changes. As one can see in fig. 4.1(a) the position of the maximum is more or less the same for all Reynolds numbers. Yet, the width of the maximum (the spatial extent of the overshoot) and therefore the size of the transition regime grows with increasing Reynolds number. A suitable characteristic length for determining the extent of the transition regime is the position at which the overshoot decays by 50%. At this position the film thickness is the mean of the maximum film thickness and the film thickness of the fully developed flow. This length is denoted as the *inflow length* l_{50} and is depicted in fig. 4.1(a) as black dots.

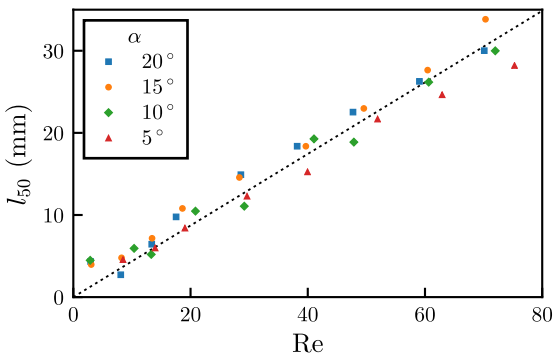

Figure 4.2: Inflow length l_{50} as a function of the Reynolds number for different inclination angles α. The dotted line shows a linear dependency. The measurements were performed with the fluid *Elbesil 140* at $B = 170\,\text{mm}$.

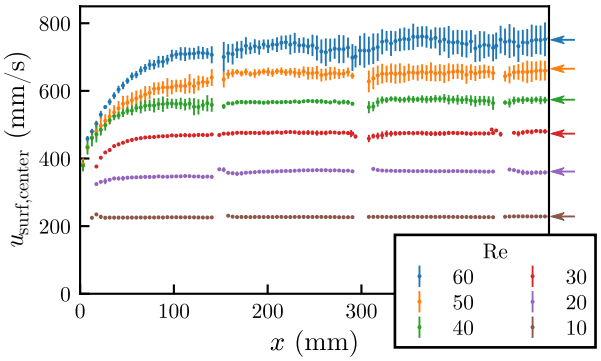

Figure 4.3: Surface velocity $u_{\mathrm{surf,center}}$ in the center of the channel as a function of x for different Reynolds numbers. The arrows at the right edge of the figure show the theoretical values for the fully developed flow. The measurement was performed with the fluid *Elbesil 140* at $\alpha = 10°$ and $B = 170\,\mathrm{mm}$.

The measurement of the inflow length l_{50} was repeated for four different inclination angles α and several Reynolds numbers. The dependency of l_{50} on the Reynolds number and the inclination angle is portrayed in fig. 4.2. It can be seen that the inflow length does not visibly depend on the inclination angle α, at least for the investigated measurement range. The dotted line in fig. 4.2 shows a line through the origin that describes the dependency of the inflow length on the Reynolds number very well. Within the measurement range the inflow length l_{50} is roughly proportional to the Reynolds number Re.

A common estimation for inflow lengths is $l_{\mathrm{inflow}}/H \propto \mathrm{Re}$ (with H being the fully developed film thickness) [65]. This can be written as $l_{\mathrm{inflow}} \propto \mathrm{Re}^{4/3}$ which contradicts the present findings for the inflow length: $l_{50} \propto \mathrm{Re}$. Yet this discrepancy is not surprising since for the derivation of the inflow length in the literature boundary layer equations were used. However, as one can see in fig. 4.1(a), the streamwise length scales of the flow are of the same order of magnitude as the film thickness. Therefore the boundary layer equations are not valid for the present system and the comparison of the literature with the measurements is not reasonable.

4.1.2 Development of the surface velocity

The inflow can not only be characterized by the variation of the film thickness but also by the variation of the surface velocity. Measurements were performed to obtain the surface velocity $u_{\mathrm{surf,center}}$ in the center plane of the channel (see section 3.2.4). Fig. 4.3 shows $u_{\mathrm{surf,center}}$ as a function of the streamwise coordinate x for several Reynolds numbers. The surface velocity generally increases along the channel until it asymptotically reaches the surface velocity of the fully developed flow, denoted by the arrows on the right of the figure. For $\mathrm{Re} = 10$ the surface velocity is constant within the observed range of x whereas for $\mathrm{Re} = 60$ it takes a few hundred millimeters to fully develop. However, a quantitative characterization of an inflow length will not be performed due to the lack of measurement accuracy in this experiment.

4.1.3 Flow field at the inlet

Now exemplary velocity fields directly at the inlet of the channel will be presented. To this end, PIV-measurements (see section 3.2.3) were performed to obtain the fluid velocity in the

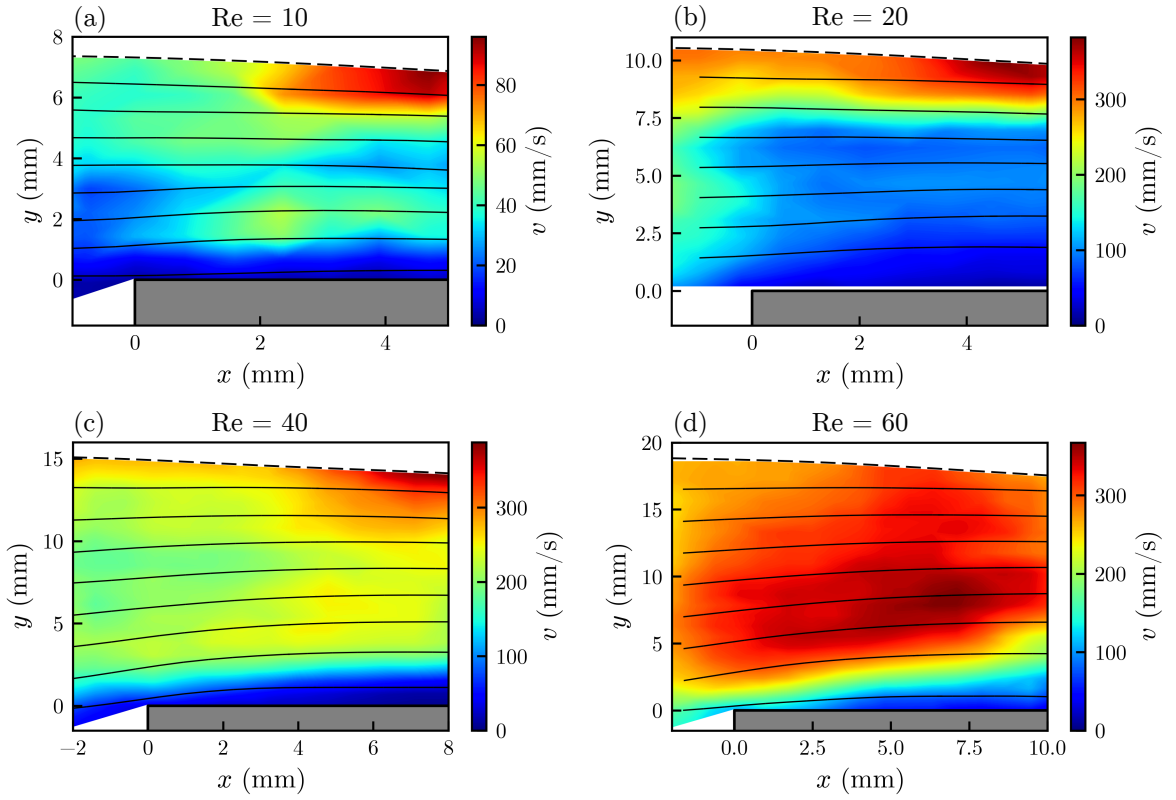

Figure 4.4: Velocity field at the inflow of the channel at different Reynolds numbers. The velocity is color coded. The solid black lines depict the streamlines, the dashed black line depicts the fluid surface. The position of the substrate is shown in gray. Measurements were performed with *Elbesil 140* at $\alpha = 10°$ and $B = 170\,\text{mm}$.

central plane of the channel for four different Reynolds numbers. The inflow of the channel was experimentally difficult to access because the side walls of the inflow tank were not transparent. The camera had to be tilted sideways which results in a focus plane that is not completely parallel to the illumination plane of the laser sheet (see fig. 3.6). This leads to a reduction of the measurement precision particularly at the edges of the measurement area. The results of this section, however, are suitable for a qualitative understanding of the inflow of the channel.

The measured flow fields are depicted in fig. 4.4: The velocity is color coded, the streamlines are shown as solid black lines. The substrate which starts at $x = 0\,\text{mm}$ is displayed in gray. The fluid surface (which is also a streamline) was measured as presented in section 4.1.1 and is displayed as dashed black line. In the white areas left of the substrate no measurements could be performed since these areas were not visible from camera perspective.

The streamlines in fig. 4.4 are visibly curved which matches the findings of a curved surface. However, the curvature of the streamlines is not very pronounced. Within the measurement range no strong vertical flow component could be observed. This is consistent with the assumption made in section 4.1.1 that the main flow direction in the inflow tank is along the fluid surface (see fig. 4.1(b)).

The flow fields in fig. 4.4 can be divided into three layers: At the bottom there is a relatively slow layer due to the no-slip condition. Above this boundary layer there is an almost constant flow field that covers most of the area. In subfigs. (a)–(c) there is an additional fast layer at the fluid surface. The fluid in this top layer also accelerates in downstream direction which is consistent with the findings of an accelerating surface velocity in section 4.1.2. In subfig. (d) no fast surface layer acceleration could be found, at least within the measured area. Possibly a fast surface layer is formed further downstream.

4.1.4 Conclusions

In this section the inflow effects at the inlet of the channel were examined. To this end, several quantities were measured which are suitable to distinguish between the inflow area where the flow is not constant and the fully developed flow that does not change in streamwise direction. PIV measurements at the inlet revealed weakly curved streamlines which are nearly parallel to the free surface, even in the inflow tank. The main flow direction at the inlet is therefore along the surface, as sketched in fig. 4.1(b). Due to the inertia of the fluid entering the channel the flow direction can not be changed abruptly, which leads to an overshoot of the film thickness in the region of the inlet. A large Reynolds number—and therefore a higher inertia—causes a greater overshoot. The streamwise extent of the overshoot and therefore the characteristic inflow length is proportional to the Reynolds number. This is in contrast to the common estimation that the inflow length is $l_{\text{inflow}} \sim \text{Re}^{4/3}$. The assumptions made for this estimation is that boundary layer equations can be used to describe the system. In the given case, however, this assumption is not valid since the film thickness and the typical length scale in streamwise direction are of the same order of magnitude.

Additionally the velocity of the fluid surface along the center of the channel was measured. It was found that the surface accelerates in downstream direction until it reaches the final velocity of the fully developed flow. The extent of the accelerating regime increases with the Reynolds number. However, a quantitative measurement of this extent was not possible due to the measurement inaccuracy.

The important result of this section is that all inflow effects decay after only a few hundred millimeters, for small Reynolds numbers even a few ten millimeters. As mentioned in section 3.3.1, the distance between the inlet and the measurement position for the linear stability is 600 mm. For the measurement of the surface velocity field (section 3.2.4) and the wave properties (section 3.3.3), the distance is the same or even greater. Therefore, the assumption of a fully developed flow at the measurement position is justified and no inflow effects have to be considered.

4.2 Influence of side walls on the basic flow

Most of the literature dealing with film flows is limited to two-dimensional systems and neglects the presence of side walls. However, at least in experimental setups side walls are inevitable and therefore their influence on the film flow has to be considered. The effect of flat side walls on the basic flow is already covered by the literature [12, 13], while the effect of corrugated side walls has not yet been reported. This section deals with the influence of both flat and corrugated side walls on the unperturbed basic channel flow, characterized by the surface velocity flow field. For the experiments, the measurement methods presented in section 3.2.4 were used. This section is based on the publication [62].

Figs. 4.5 and 4.6 show the surface velocity field of the fully developed basic flow for Re = 15, channel width $B = 84\,\mathrm{mm}$ and different side wall configurations. Fig. 4.5 depicts the streamlines and therefore the direction of the surface flow, whereas in fig. 4.6 its absolute velocity u_{surf} is shown. In the white areas in figs. 4.5 and 4.6 no trajectories were measured, as will be discussed later in this section. As was to be expected, the streamlines for the flow within

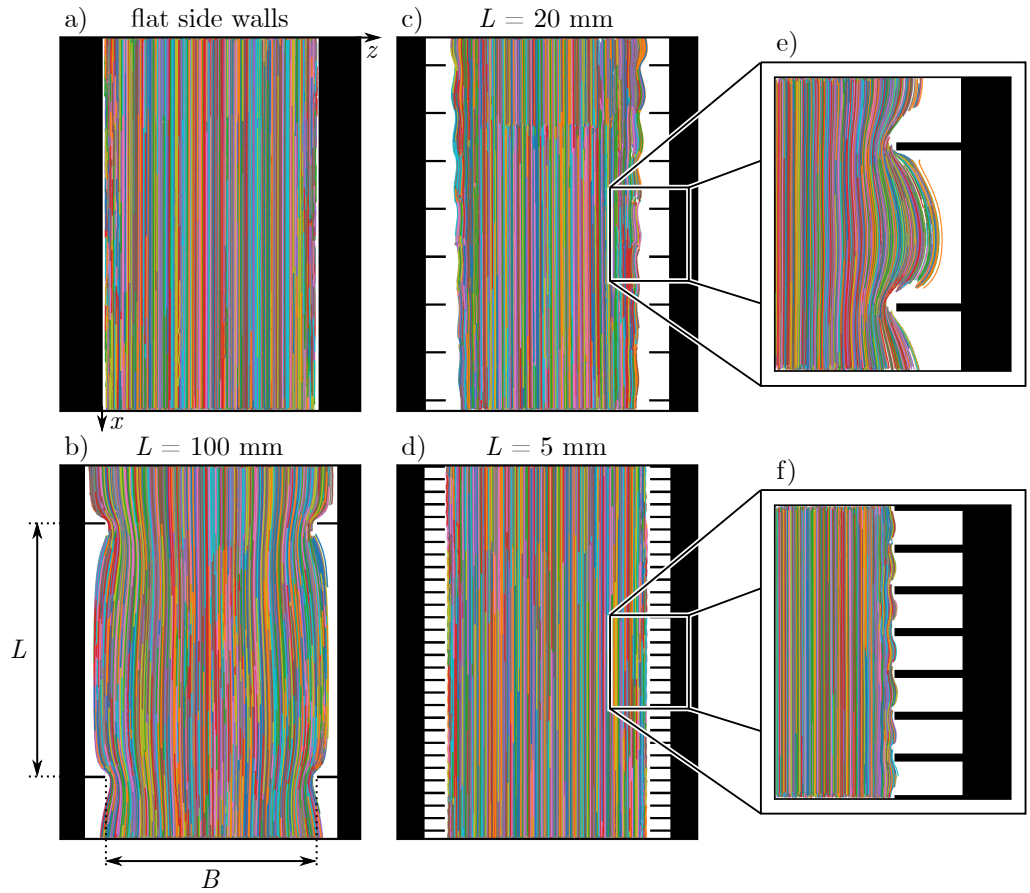

Figure 4.5: Trajectories of the surface velocity for Re = 15, channel width $B = 84\,\mathrm{mm}$, and different tip distances L. The main flow direction is from top to bottom. (a) Flat side walls, (b) $L = 100\,\mathrm{mm}$, (c) $L = 20\,\mathrm{mm}$, and (d) $L = 5\,\mathrm{mm}$. (e) and (f) are more detailed measurements corresponding to (c) and (d), respectively. In the white areas no trajectories could be measured. © AIP Publishing

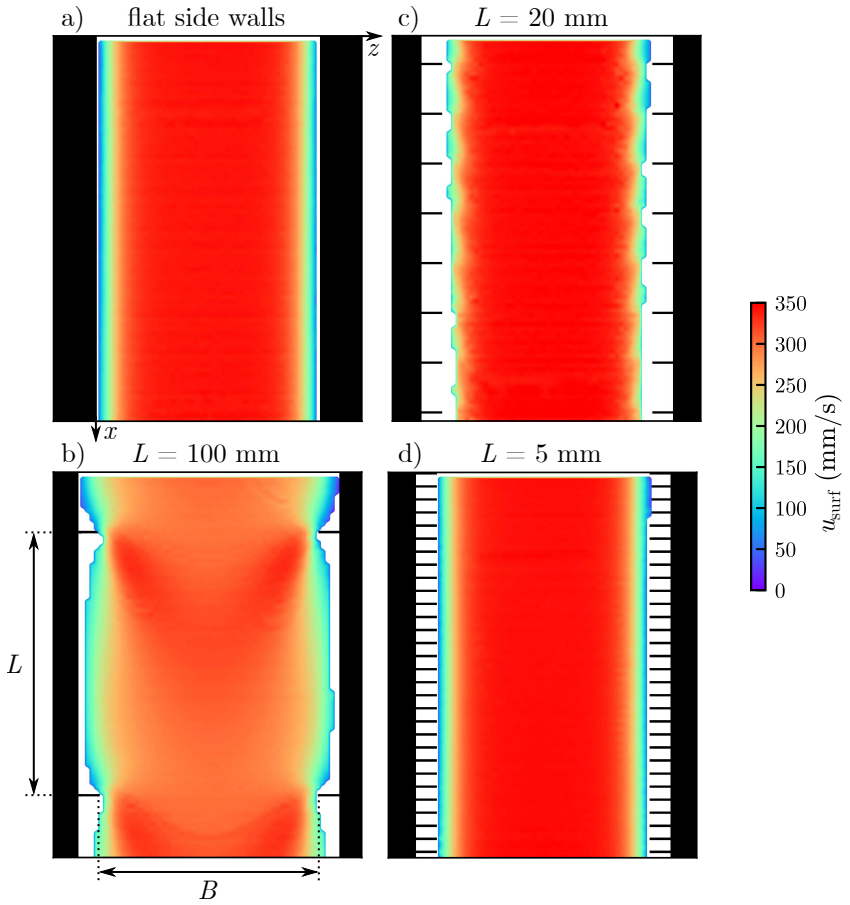

Figure 4.6: Velocity fields corresponding to figs. 4.5(a) – (d). (a) Flat side walls, (b) $L = 100\,\text{mm}$, (c) $L = 20\,\text{mm}$, and (d) $L = 5\,\text{mm}$. © AIP Publishing

flat side walls (fig. 4.5(a)) are parallel to the side walls and the velocity is constant along the streamlines (fig. 4.6(a)). In the vicinity of the side walls the flow is slowed down due to the no-slip condition, whereas in the center of the channel the velocity is constant (see also section 3.1.2). As the film thickness is large enough, the accelerating effects of the capillary elevation at the side walls can be neglected [53]. The velocity field in the channel is identical to the velocity field of an rectangular pipe where the free surface of the channel flow corresponds to the symmetry plane of the pipe (see section 3.1.2 and in particular fig. 3.2).

Flows within corrugated side walls show different behavior. If the tip distance is small (e.g. $L = 5\,\text{mm}$, see figs. 4.5(d), (f) and 4.6(d)), the surface flow field is similar to the one with flat side walls. Only near to the side walls the flow fields differ. In between the tips of each wall, eddies appear, as often seen in strongly undulated substrates at the bottom on the channel [23, 43, 75]. Since in the area where these eddies appear, the capillary elevation is dominant, it was not possible to quantitatively investigate them. The tracer particles tend to rise within the elevation and therefore do not follow the streamlines properly. In order to avoid the depiction of false streamlines, no particles were introduced into the region of the eddies. Therefore, no trajectories and in particular no eddies are visible in the close vicinity of the side walls in fig. 4.5.

When increasing the tip distance L, also the difference to the flow field with flat side walls increases. The surface velocity field for $L = 20\,\mathrm{mm}$ (figs. 4.5(c),(e) and 4.6(c)) shows a stronger modulation that reaches further into the central flow.

For $L = 100\,\mathrm{mm}$ (figs. 4.5(b) and 4.6(b)) one can see a nearly parallel flow within two subsequent tips but strongly curved streamlines around the tips. The velocity field shows a slight overshoot right after the tips. This overshoot is more distinct for low Reynolds numbers and vanishes for higher Reynolds numbers.

To summarize this section, the influence of corrugated side walls on the surface velocity of film flows exceeds the influence of flat side walls. The larger the tip distance, the further the disturbance caused by the side walls reaches into the fluid. For short tip distances, the influence of corrugated side walls is similar to the influence of flat side walls. For very long tip distances, which were experimentally not accessible, the influence of the corrugations have to be limited to the region of the tips, whereas in the region between two subsequent tips the flow field has to be similar to the flow field in a channel with flat side walls.

4.3 Influence of side walls on the stability of the flow

The following section deals with the main question of this thesis: How do the side walls affect the stability of an open-channel flow? It is known, that side walls tend to stabilize the channel flow compared to the plane flow [51–53]. However, the literature focuses on systems with flat side walls. Therefore the question arises: How do corrugated side walls affect the stability of an open-channel flow? Section 4.3.1 includes a parameter study of the effect on both flat side walls and corrugated side walls (including a variation of the channel width) on the critical Reynolds number. Section 4.3.2 focuses on the full stability charts and shows an unexpected fragmentation of the neutral curve that was known so far only from undulated substrates. An extensive parameter study unveils the dependencies of this fragmentation on numerous system parameters including the side wall configurations.

4.3.1 Shift of the critical Reynolds number

The following section contains a parameter study to investigate the effect of both the channel width and the side wall configuration on the stability of the basic flow. To this end, stability measurements with different channel widths were performed with flat walls as well as corrugated side walls. Finally the dependency of the critical Reynolds number on the channel width as well as on the streamwise length scale of the corrugations could be figured out and will be shown in this section. The content of this section is based on the publication [62].

4.3.1.1 Stabilization due to the reduction of the channel width

Fig. 4.7 shows the dependency of the neutral curves on the channel width B for fixed side wall configurations. The dashed lines indicate the theoretical neutral curve $\mathrm{Re}_{\mathrm{n,2D}}(f)$ of the plane flow of infinite extent. This theoretic flow becomes first unstable for the critical Reynolds number $\mathrm{Re}_{\mathrm{crit,2D}} = \mathrm{Re}_{\mathrm{n,2D}}(f \to 0) = (5/4)\cot\alpha \approx 7.09$ (for $\alpha = 10°$, see eq. (2.75)). As the measured free surface waves have to be shorter than the channel, at very low frequencies no measurements were performed. This is denoted as “invalid” areas in fig. 4.7. The capillary effects on the stability of the flow can be neglected as the capillary length is much smaller than the channel width $L_{\mathrm{cap}} \ll B$ and the Kapitza number Ka is sufficiently small. Georgantaki et al. [52] studied the effect of the Kapitza number on the stability of film flows and showed that a high Kapitza number stabilizes the flow. For the experiments with $\mathrm{Ka} \approx 1.32$ this effect is negligible.

The neutral curves for flat side walls are shown in fig. 4.7(a). Even for the maximum channel width $B = 129\,\mathrm{mm}$ the measured curve differs from the theoretical line. This is due to the finite amplitude of the measured waves unlike the theoretical waves with an infinitesimal small amplitude. Waves tend to be more stable if their amplitude is larger [44]. The strong stabilization at higher frequencies can be explained by an additional damping effect, that will be discussed in section 4.3.2. For decreasing channel widths the neutral curve shifts to higher Reynolds numbers. This stabilizing effect has already been studied by Vlachogiannis et al. [51] for a mixture of water and glycerol with low viscosity. For the present experiments with

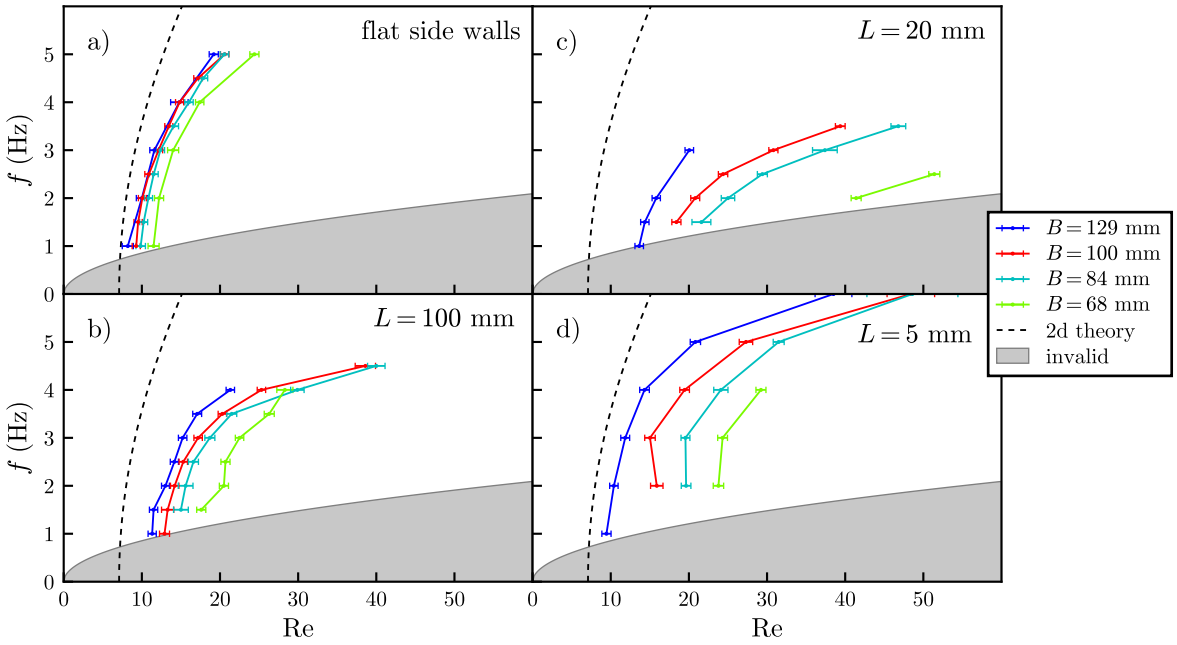

Figure 4.7: Neutral curves for different channel widths. The side wall configuration is fixed in each subfigure. (a) Flat side walls, (b) $L = 100\,\mathrm{mm}$, (c) $L = 20\,\mathrm{mm}$, and (d) $L = 5\,\mathrm{mm}$. Different colors represent different channel widths. The dashed line indicates the neutral curve of the plane flow of infinite extent. In the "invalid" area, no measurements were performed. All measurements were performed with *Elbesil 140* at $\alpha = 10°$. © AIP Publishing

highly viscous silicone oil the effect is the same. One can also see the shift of the neutral curve to higher Reynolds numbers for decreasing channel widths if corrugated side walls were used, see figs. 4.7(b)–(d). For large channel widths the neutral curve approaches the theoretical line (except a small shift due to finite wave amplitudes, which would also appear for infinite wide channels). For smaller channels the flow becomes more stable. This stabilizing effect is significantly larger for corrugated side walls than for flat side walls.

To quantify the stabilizing effect of the channel width, the measured neutral curve is extrapolated to the critical Reynolds number $\mathrm{Re_n}(f \to 0) = \mathrm{Re_{crit}}$. For this purpose the data is fitted to the function

$$\mathrm{Re_n}(f) = c_1 f^{c_2} + \mathrm{Re_{crit}} \tag{4.1}$$

with the fit parameters c_1, c_2 and $\mathrm{Re_{crit}}$. The stability shift ϵ is introduced as

$$\epsilon = \frac{\mathrm{Re_{crit}}}{\mathrm{Re_{crit,2D}}} - 1\,. \tag{4.2}$$

Fig. 4.8 shows the dependency of ϵ on the channel width B. The theoretical stability threshold of the plane flow corresponds to $\epsilon = 0$. For clarification colored shaded areas were used in fig. 4.8 to guide the eye to show the approximate course of the data points. As one can see, for every side wall configuration the stability shift grows for decreasing channel widths. For large channel widths the stability shift tends to zero which corresponds to the transition of the channel flow to the plane flow of infinite extent.

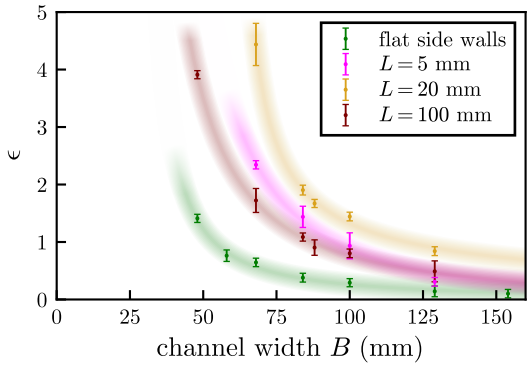

Figure 4.8: Stability shift ϵ as function of the channel width B. Different colors represent different sidewall configurations. The colored shaded areas are guides to the eye. The measurements were performed with *Elbesil 140* at $\alpha = 10°$. © AIP Publishing

The stabilizing effect of the side wall corrugations is also visible in fig. 4.8: For each channel width B, the stability shift ϵ for corrugated side walls is significantly larger than for flat side walls.

4.3.1.2 Stabilization due to side wall corrugations

Fig. 4.9 shows the dependency of the neutral curves on the side wall configuration at fixed channel widths. The neutral curves for corrugated side walls are distinctly shifted to the right compared to the case of flat side walls, most of all the curves for $L = 20\,\text{mm}$. For short and large tip distances $L = 5\,\text{mm}$, respectively $L = 100\,\text{mm}$, the neutral curves get closer to the neutral curve of the flat side walls. This is consistent with the fact, that the limit of very short tip distances $L \to 0$ corresponds to flat side walls. On the other hand, the limit of very large tip distances $L \to \infty$ also corresponds to flat side walls, but with a greater channel width $B + 2l_\text{t} = B + 16\,\text{mm}$ (see fig. 3.3). These two limits are basically different, but the difference is rather small. Please see appendix A.3 for a detailed discussion of the limiting cases for L.

Fig. 4.10 summarizes the main information of fig. 4.9. The stability shift ϵ is shown as a function of the tip distance L. For $L \to 0$ the stability shift converges to the stability shift of flat side walls, for $L \to \infty$ it converges to the shift of flat side walls with the greater channel width $B + 2l_\text{t}$. Between these two limits there is a clear maximum in the stability shift, which is indicated by the colored shaded areas. This maximum occurs for all channel widths at a similar tip distance around $L = 20\,\text{mm}$. The narrower the channel is, the more pronounced the maximum is. For very large channel widths the maximum decreases and for $B \to \infty$ it even vanishes. This corresponds to the transition to the plane flow of infinite extent, where the side walls do no longer have any influence.

To confirm the assumed profile of $\epsilon(L)$ two additional experiments were carried out. For $B = 84\,\text{mm}$ the stability shift at the two tip distances $L = 10\,\text{mm}$ and $L = 40\,\text{mm}$ was measured. As shown in fig. 4.10, the additional data points fit in with the others and confirm the assumption of one single maximum between $L = 10\,\text{mm}$ and $L = 40\,\text{mm}$.

The stabilizing effect of side walls can be brought together with the effect on the basic flow. Pollak et al. [53] investigated the amplitude of artificially excited waves at different transverse positions in the channel. They found that, even for an unstable flow, the wave amplitude in

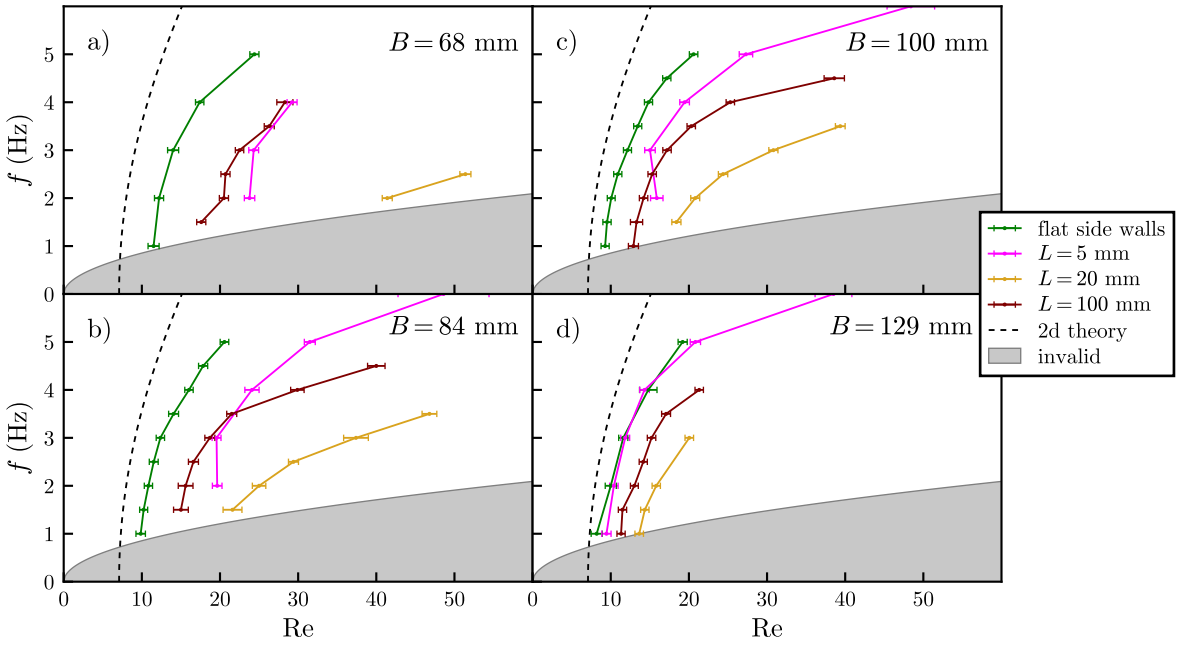

Figure 4.9: Neutral curves for different side wall configurations. The channel width is fixed in each subfigure. (a) $B = 68\,\mathrm{mm}$, (b) $B = 84\,\mathrm{mm}$, (c) $B = 100\,\mathrm{mm}$, and (d) $B = 129\,\mathrm{mm}$. Different colors represent different side wall corrugations. The dashed line indicates the neutral curve of the plane flow of infinite extent. In the "invalid" area, no measurements were performed. All measurements were performed with *Elbesil 140* at $\alpha = 10°$. © AIP Publishing

the vicinity of the side wall decreases. It was shown in section 4.2 that the fraction of the fluid which is affected by the side walls increases if the channel width is reduced. Since this "damping area" increases for small channels, the flow is generally more stable. Therewith also the stronger damping in channels with corrugated side walls can be explained. In this case the area affected by the side walls is significantly larger than for flat side walls. In the limit of very long and very short tip distances, the effect of corrugated side walls on both the basic flow and the stability are the same as for flat side walls.

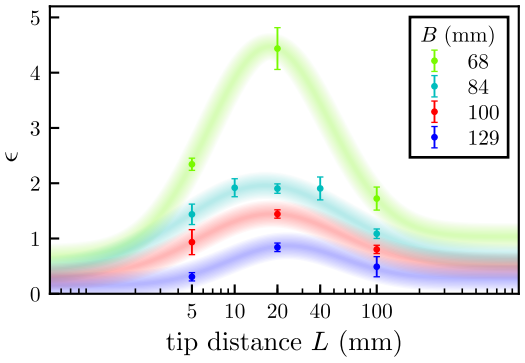

Figure 4.10: Stability shift ϵ as function of the tip distance L. Flat side walls correspond to $L \to 0$ and $L \to \infty$. Different colors represent different channel widths. The colored shaded areas are guides to the eye. The measurements were performed with *Elbesil 140* at $\alpha = 10°$. © AIP Publishing

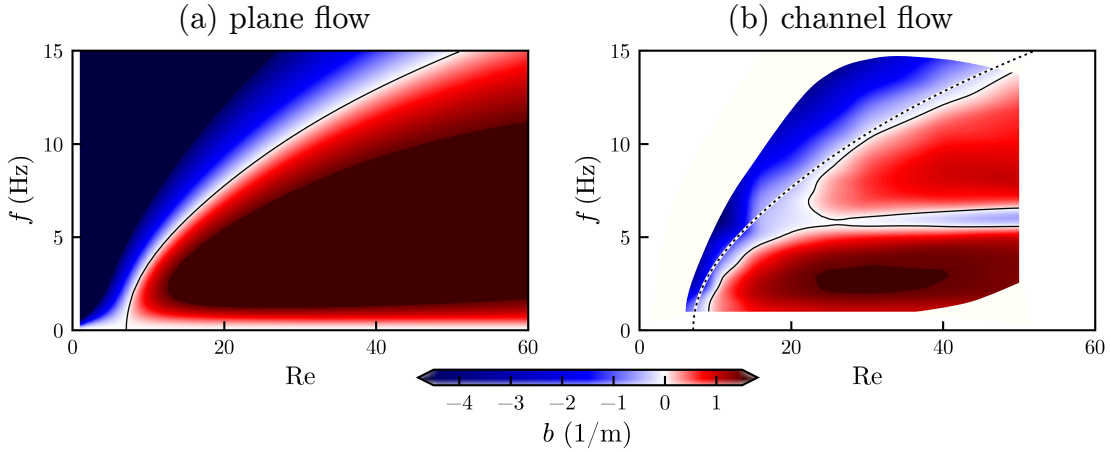

Figure 4.11: (a) Theoretical stability chart of the plane flow and (b) measured stability chart of the channel flow for $\alpha = 10°, B = 170\,\text{mm}$ with the fluid *Elbesil 140*. The growth rate b is color coded, the solid black line represents the neutral curve $b = 0$. The dotted line in (b) shows the theoretical neutral curve of the plane flow (c.f. (a)). © Springer Nature

4.3.2 Fragmentation of the neutral curve

Figure 4.11 shows (a) the theoretical stability chart of the plane flow and (b) the measured stability chart of an open-channel flow with flat side walls and flat substrate. The channel flow shows an unexpected horizontal stable band in the middle of the unstable area of the plane flow. Until now, the occurrence of fragmented neutral curves and additional unstable isles was only known for undulated substrates, but not for channels without corrugations. In this section it will be shown, that fragmentation occurs not only in "undulated" systems, but also in "flat" systems with side walls. To investigate this new phenomenon, a parameter study was performed to determine the dependency of the stabilization on several system parameters (i.e. excitation frequency, Reynolds number, channel width, inclination angle and viscosity). Finally, the question will be posed: Is this stabilization only an effect of flat side walls? Or can this phenomenon also be seen in a channel with corrugated side walls? This section is based on the publication [63].

4.3.2.1 Appearance of fragmented neutral curves in a system with flat side walls

The measured stability charts for different inclination angles α and channel widths B are depicted in Fig. 4.12. In the white areas at the margin of the charts no measurements were performed. Particularly for low Reynolds numbers or high frequencies the growth rates often were too small to measure. In subfig. (h) it was not possible to reach a higher Reynolds number due to the finite pumping capacity. One can observe a switching [44, 46] between three different patterns of stability charts when changing the system parameters. All three patterns can be found in the measurements for $\alpha = 10°$ (fig. 4.12(d)–(h)). At large channel widths (subfig. (h)) there is one single unstable area, similar to the stability chart of the plane flow (dotted line). When decreasing the channel width, the unstable area splits in two separate isles divided by a horizontal stable band (subfigs. (g) and (f)). Finally, with further reduction, the high frequency

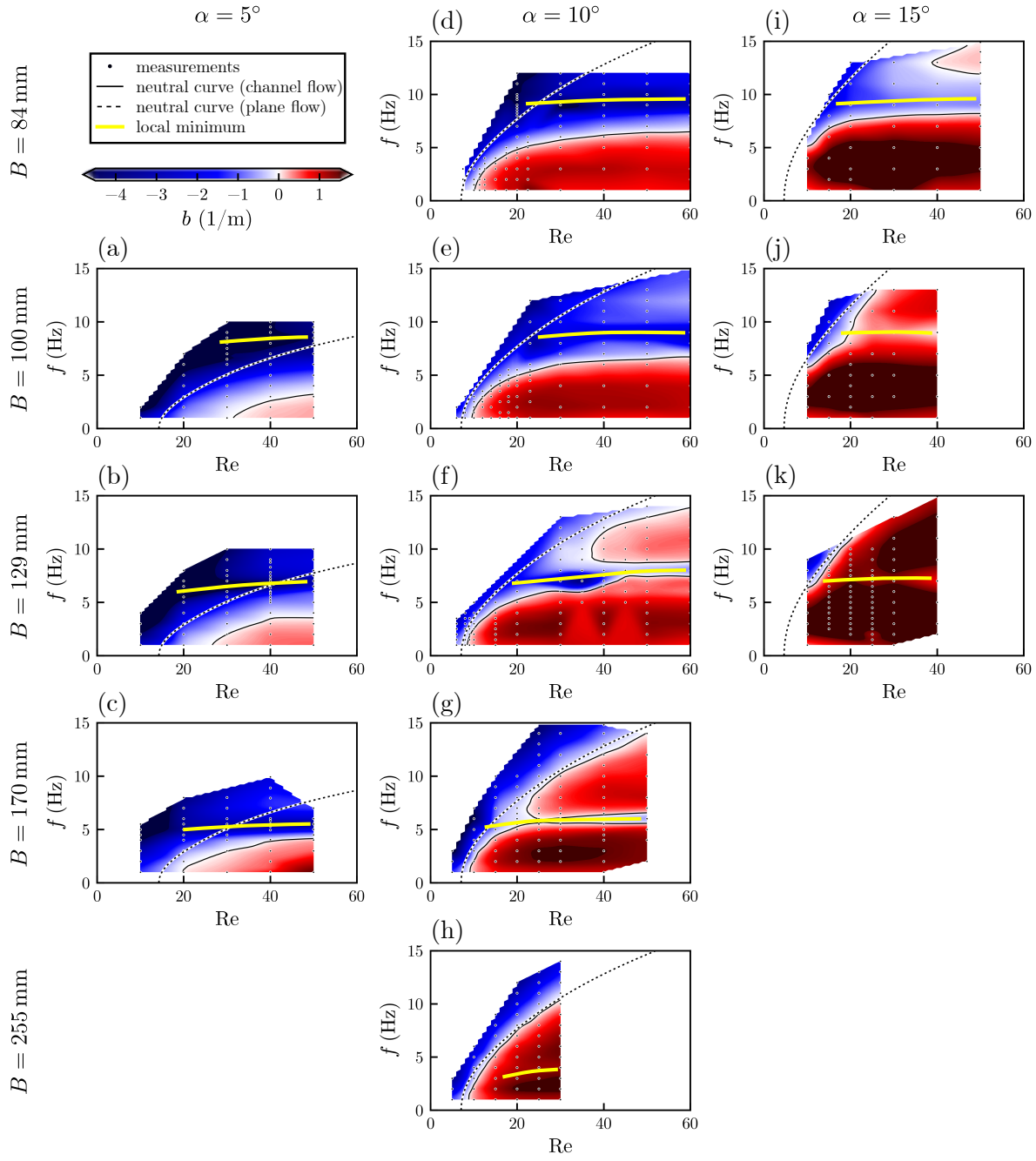

Figure 4.12: Stability charts for different inclination angles α and channel widths B measured with the fluid *Elbesil 140*. The individual measurement positions are marked as black dots. The growth rate b is color coded, stable areas are marked blue, unstable areas are marked red. The solid black lines denote the measured neutral curves, the black dotted lines the theoretical neutral curves of the plane flow. The solid yellow lines qualitatively show the local minima of the growth rate. © Springer Nature

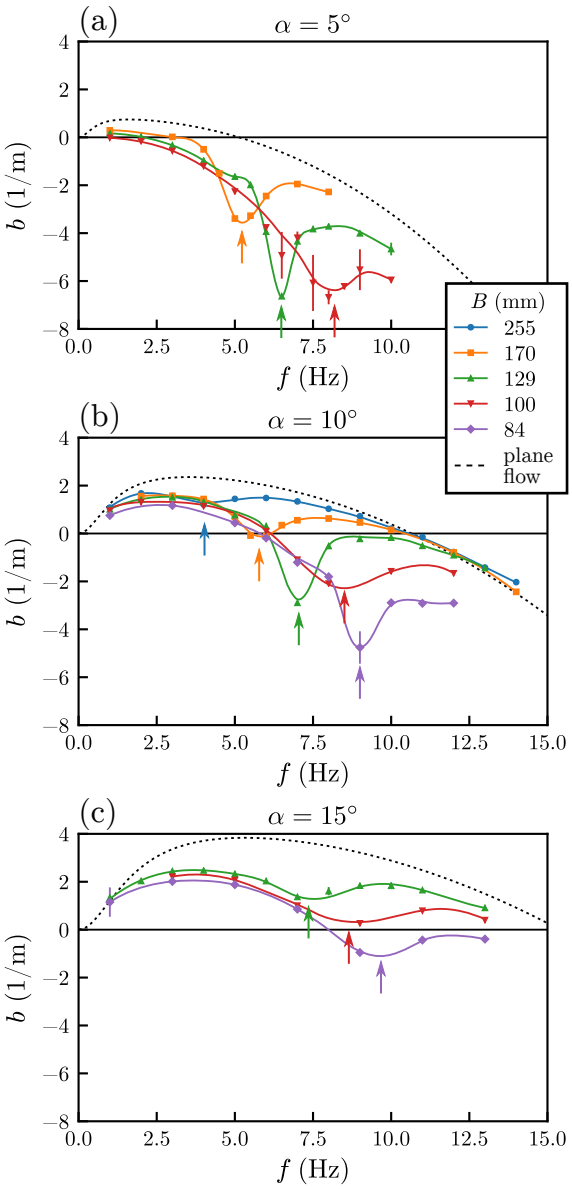

Figure 4.13: Growth rate b as function of the excitation frequency f for Re = 30 and different channel widths B measured with the fluid *Elbesil 140*. The inclination angle is (a) $\alpha = 5°$, (b) $\alpha = 10°$, (c) $\alpha = 15°$. The arrows highlight the positions of the minima, the dotted lines show the theoretical growth rate of the plane flow. © Springer Nature

isle disappears since the stable band becomes wider and moves to higher frequencies (subfigs. (e) and (d)). This effect is the same for all inclination angles. However, for $\alpha = 5°$ the system is generally more stable than for $\alpha = 10°$ and therefore there is no unstable isle at high frequencies within our measurement range. On the other hand, for $\alpha = 15°$ the system is generally less stable and therefore the stable band occurs only at smaller channel widths. All stability charts show a local minimum of the growth rate, regardless of whether there is a stable band or not, qualitatively indicated by the yellow line. The frequency of the minimum is nearly the same for all inclination angles but depends strongly on the channel width.

A more detailed visualization of the stabilization is shown in fig. 4.13, where the growth rate b is plotted as function of the excitation frequency f for a single Reynolds number Re = 30 and several channel widths B. At very low and very high frequencies the measured growth rate generally approaches the theoretical curve of the plane flow, but at intermediate frequencies a

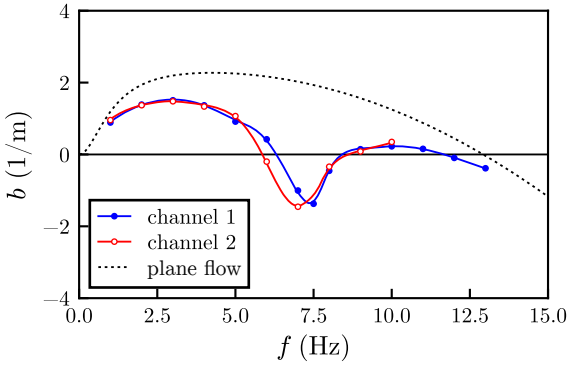

Figure 4.14: Verification of the experiment: Growth rate b as function of f for Re $= 40$, $\alpha = 10°$, $B = 129\,\text{mm}$ measured in two different channels (see Table 3.2) with the fluid *Elbesil 140*. The dotted line shows the theoretical growth rate of the plane flow. © Springer Nature

distinct minimum can be seen. The occurrence of a single minimum indicates a stabilizing effect at a certain frequency range. A destabilizing effect, as it may occur in systems with corrugated substrates [41], is not present. The position of the minimum depends strongly on the channel width B. One can also see that the damping is generally stronger for smaller channels.

To ensure that the measured damping is not an artifact of the experimental setup, two identical measurements in two channels with different geometric dimensions, pumps and other peripherals were performed (see section 3.1.5 and tab. 3.2). Fig. 4.14 shows the growth rate at Re $= 40$ for $\alpha = 10°$, and $B = 170\,\text{mm}$ measured with *Elbesil 140* in channel 1 and channel 2. The two curves show qualitatively the same damping phenomenon, only the position of the minimum is shifted by $\approx 0.5\,\text{Hz}$. Thus, the effect could be verified and also an estimate for the measurement accuracy could be achieved.

An important result of this section is the fact, that the frequency at which the minimum of the growth rate occurs shows no significant dependency on the inclination angle. On the other hand, the theoretical neutral curve of the plane flow clearly depends on the inclination angle. Therefore the damping is an effect that is generally unrelated to the two-dimensional stability of the plane flow. In other words, the damping occurs whether the two-dimensional flow is stable or unstable and the position of the damping band is unrelated to the growth rate of the two-dimensional wave at this frequency. The decisive parameter for the damping is the channel

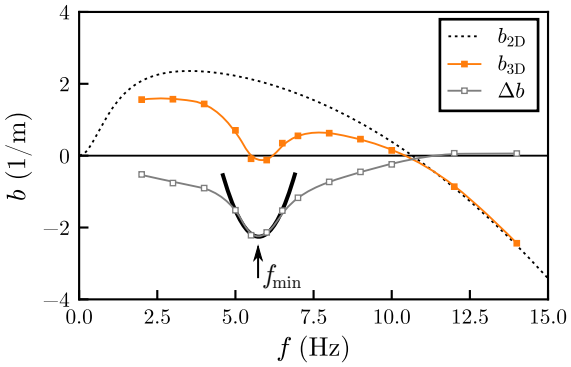

Figure 4.15: Example for determining the damping frequency f_{min}. The orange squares denote the measured growth rate of the channel flow b_{3D}, the dotted black line the theoretical growth rate of the two-dimensional flow b_{2D}. The damping term $\Delta b = b_{3D} - b_{2D}$ (see Eq. (4.3)) is shown in grey. The solid black line shows a parabolic fit around the minimum of Δb, indicated by the arrow. The measurement was done at Re $= 30, \alpha = 10°$ and $B = 170\,\text{mm}$ with the fluid *Elbesil 140*. © Springer Nature

width B. Therefore, the damping can be assumed to be an additional effect caused by the side walls that is independent of the basic stability of the plane flow of infinite extent.

4.3.2.2 Characterization of the fragmentation of the neutral curve

In this section, the dependencies of the damping on the following system parameters are investigated: the Reynolds number Re, the channel width B and the inclination angle α. The damping is assumed to be an effect that is independent of the stability of the plane flow (see previous section 4.3.2.1). Therefore, the measured growth rate b of the three dimensional channel flow (here referred as b_{3D}) can be written as the sum of the growth rate of the two-dimensional plane flow b_{2D} and an independent term Δb describing the damping.

$$b_{3D} = b_{2D} + \Delta b\,. \tag{4.3}$$

The damping term Δb includes all effects caused by the side walls. Therefore, it must vanish for infinite large channel widths. An example of Δb is given in fig. 4.15. To characterize the typical frequency of the damping, a parabola is fitted to the region of the minimum, as shown in fig. 4.15. The frequency of the local minimum is referred to as *damping frequency* $f_{\min}$.

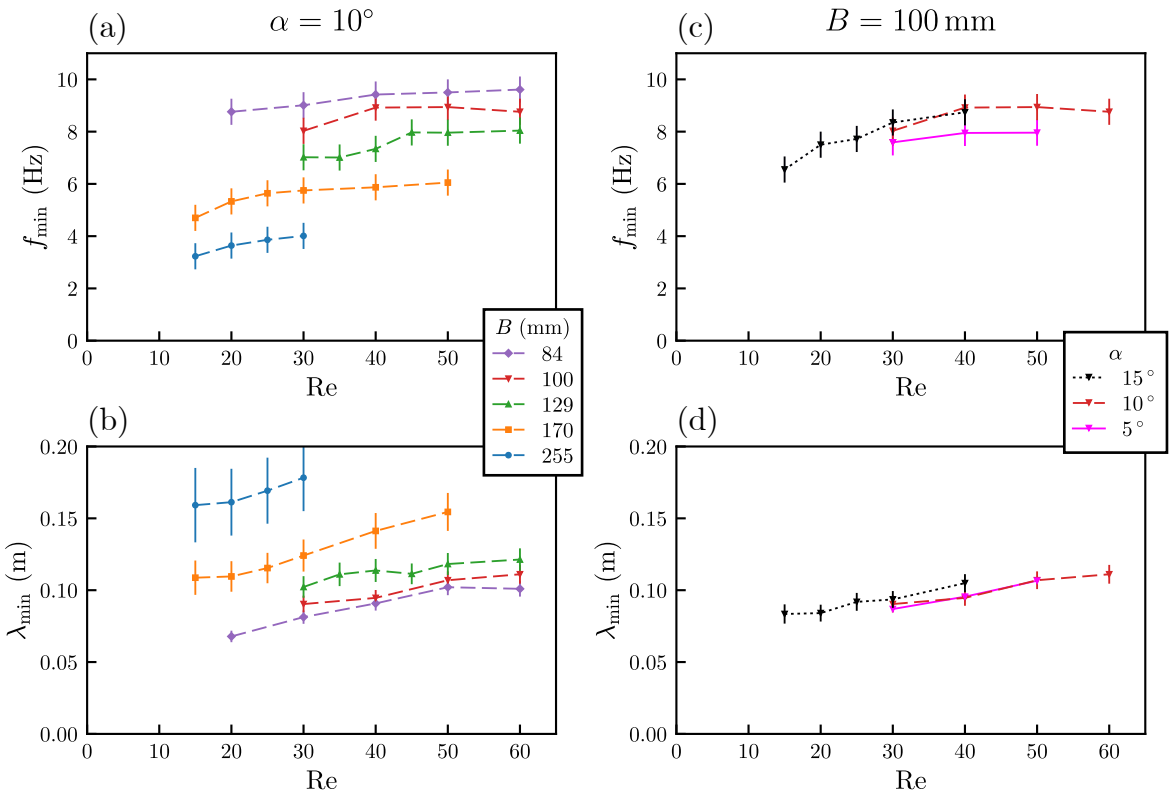

Figure 4.16: (a) Damping frequency $f_{\min}$ and (b) damping wavelength $\lambda_{\min}$ as a function of the Reynolds number Re for a fixed inclination angle $\alpha = 10°$ and different channel widths B. (c) $f_{\min}$ and (d) $\lambda_{\min}$ as a function of Re for a fixed channel width $B = 100\,\text{mm}$ and different inclination angles α. The fluid was *Elbesil 140*. © Springer Nature

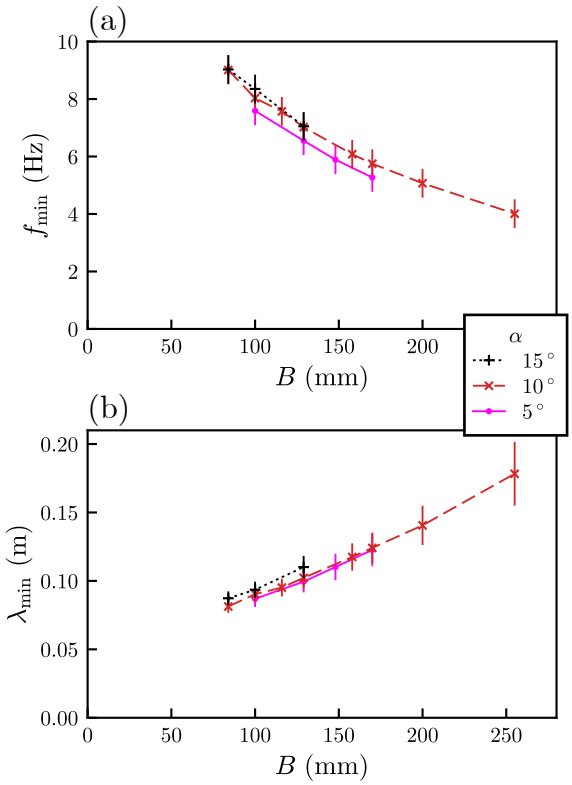

Figure 4.17: (a) Damping frequency $f_{\min}$ and (b) damping wavelength $\lambda_{\min}$ as functions of the channel width B for three different inclination angles α at Re = 30. The fluid was *Elbesil 140*. © Springer Nature

An error of 0.5 Hz is assumed, based on the reproducibility of the curves (see Fig. 4.14). The corresponding wavelength $\lambda_{\min}$, referred to as *damping wavelength*, can be calculated from $f_{\min}$ as discussed in section 3.3.2. The error of $\lambda_{\min}$ can be calculated via error propagation, including the error of $f_{\min}$ and Re.

Fig. 4.16 shows $f_{\min}$ and $\lambda_{\min}$ as a function of the Reynolds number Re for several channel widths B and inclination angles α. In subfigs. (a) and (c) one can see that $f_{\min}$ slightly increases with Re. However, for large Reynolds numbers $f_{\min}$ barely changes any more. Since the wavelength is not only a function of the frequency, but also of the Reynolds number, $\lambda_{\min}$ generally increases with Re, what can be seen in subfigs. (b) and (d). The dependency on the inclination angle α is also not notable: Fig. 4.16(c) and (d) show that $f_{\min}$ as well as $\lambda_{\min}$ barely depend on α. It is not possible for $f_{\min}$ and $\lambda_{\min}$ both to be independent of α, because the wavelength λ is a function of f and α. Therefore, if $f_{\min}$ was independent of α, $\lambda_{\min}$ would have to vary with α. With the experimental data it is not possible to determine a clear dependency, but one can see that in the measurement range the effect of the inclination angle is rather small compared to the channel width, which will be discussed in the following.

A very strong dependency on the channel width B exists for $f_{\min}$ and $\lambda_{\min}$, respectively. One can see in figs. 4.16(a) and (b) that for increasing channel widths the damping frequency $f_{\min}$ strongly decreases and the damping wavelength $\lambda_{\min}$ strongly increases. A more quantitative plot is shown in fig. 4.17, where the dependency of the damping on the channel width is plotted. Fig. 4.17(a) shows the monotonous decreasing of $f_{\min}$ with increasing B for all inclination angles α. As one can see in fig. 4.17(b), the damping wavelength $\lambda_{\min}$ increases monotonously with the channel width B, so for a wider channel longer waves are damped. But since this is no linear dependency, there is no strict matching of the wavelength and the channel width.

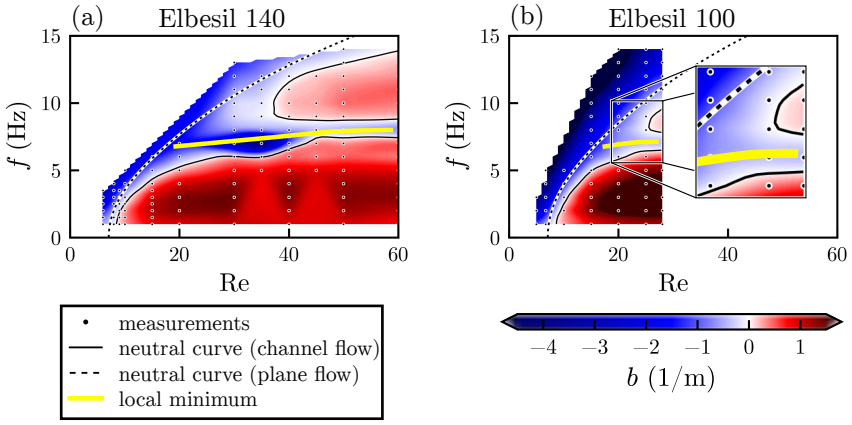

Figure 4.18: Stability charts for $\alpha = 10°$, $B = 129\,\text{mm}$ and two different viscosities: (a) $\eta = 136.7\,\text{mPas}$ (*Elbesil 140*) and (b) $\eta = 99.4\,\text{mPas}$ (*Elbesil 100*). The yellow lines qualitatively indicate the position of the local minimum of the growth rate. The dotted lines show the theoretical neutral curve of the plane flow. © Springer Nature

Exemplarily the influence of another system parameter will be shown: the viscosity η. Additional measurements with the fluid *Elbesil 100* (see section 3.1.4) were performed in channel number 3 with the channel width $B = 129\,\text{mm}$ at an inclination angle $\alpha = 10°$. Since the pumping power in this setup was limited, a maximum Reynolds number of 28 could be reached. Fig. 4.18 shows a comparison of the two measurements with the same parameters, except for the viscosity. One can clearly see that the damping effect occurs for both viscosities. Also the frequency of the damping matches for both measurements.

A more quantitative representation of fig. 4.18 is shown in fig. 4.19, where the damping frequency f_{min} is shown as a function of Re for different viscosities. It can be seen that the two lines representing the two viscosities fit together almost perfectly. The damping frequency f_{min} is not visibly affected by the viscosity. However, since the numerical calculations show that the wavelength of the wave with given frequency and Reynolds number varies when changing the viscosity of the fluid, the damping wavelength λ_{min} must be affected. In this case there is a shift of approximately 10%. It is not clear how a change in the viscosity causes a change in the damping wavelength, but not in the damping frequency.

To summarize this section, several dependencies of f_{min} and λ_{min} on the system parameters were shown: Both quantities barely depend on the inclination angle α but strongly on the

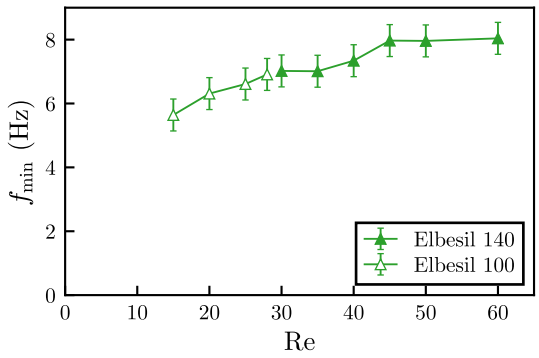

Figure 4.19: Damping frequency f_{min} as function of the Reynolds number Re for $\alpha = 10°$, $B = 129\,\text{mm}$ and two different viscosities (sc.f. fig. 4.18). © Springer Nature

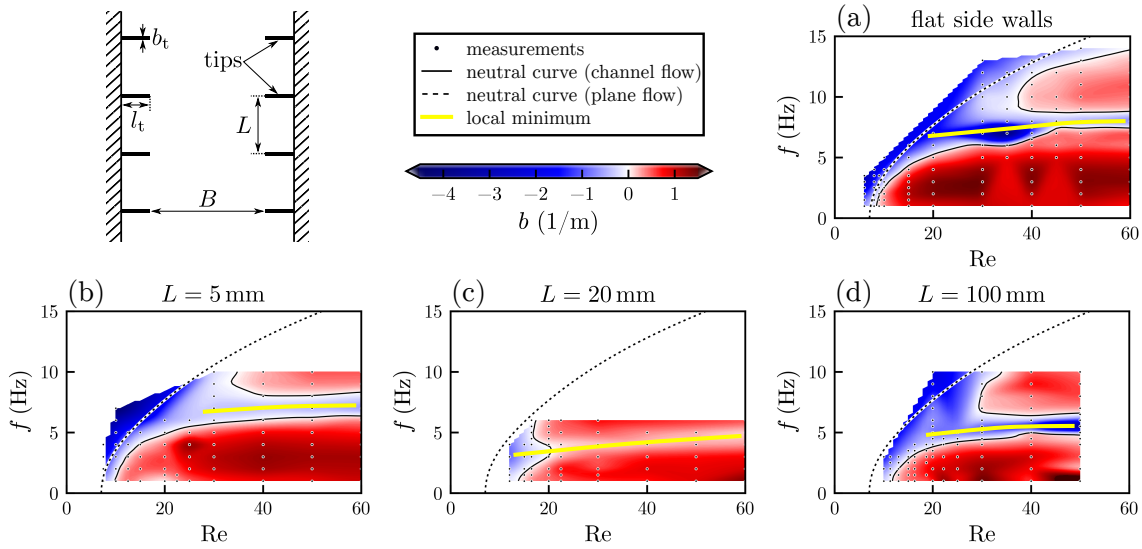

Figure 4.20: Stability charts for different side wall configurations: (a) flat side walls, (b)–(d) corrugated side walls: (b) $L = 5\,\mathrm{mm}$, (c) $L = 20\,\mathrm{mm}$, (d) $L = 100\,\mathrm{mm}$. The yellow lines qualitatively indicate the position of the local minimum of the growth rate. The dotted lines show the theoretical neutral curves of the plane flow. The measurements were performed with the fluid *Elbesil 140* at $\alpha = 10°$ and $B = 129\,\mathrm{mm}$. © Springer Nature

channel width B. The larger the channel width, the larger the wavelength of the damped wave. The Reynolds number Re has a minor effect on f_{min}, but a notable effect on λ_{min}. The viscosity has no visible impact on the damping frequency, but on the damping wavelength. It was not possible to find a matching of two quantities and particularly no dimensionless number to describe the dependency of the damping on the system parameters. Nevertheless, clear and explicit trends in the dependencies could be found.

4.3.2.3 The influence of side wall corrugations

Now the question arises: Is the newly found damping only an effect of flat side walls? Or does this phenomenon also appear in corrugated systems? And if so, does the side wall corrugation increase this effect? To this end, experiments in a channel with flat substrate and corrugated side walls (see section 3.1.3) were performed in which the streamwise length scale of the corrugation was varied. The results are depicted in fig. 4.20, where the stability chart of a channel flow within flat side walls is compared to those of channels with corrugated side walls. The inclination angle α, the viscosity η and the channel width B are the same for all measurements. For our measurements the streamwise tip distance L was varied from 5 mm to 100 mm. Fig. 4.20 clearly shows that the damping is not only an effect of flat walls, but also occurs in channels with corrugated side walls. Qualitatively, the stability charts show the same horizontal stabilization, but the position of the stable band is significantly shifted to lower frequencies.

A more quantitative representation of Fig. 4.20 is shown in Fig. 4.21, where the damping frequency f_{min} is shown as function of Re for the different side wall configurations. The corrugated

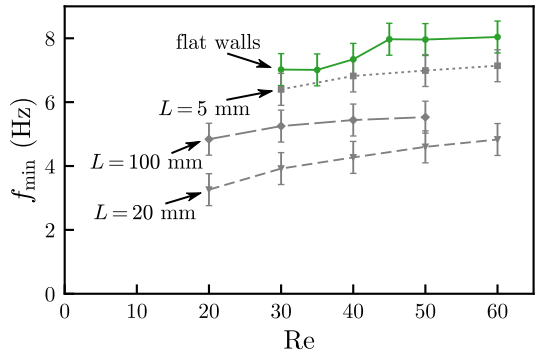

Figure 4.21: Damping frequency $f_{\min}$ as a function of the Reynolds number Re. In green the measurement with flat side walls is shown. The grey lines show $f_{\min}$ for corrugated side walls with different tip distances. The measurements were performed with the fluid *Elbesil 140* at $\alpha = 10°$ and $B = 129\,\text{mm}$. © Springer Nature

side walls show a very strong effect: As one can see, for all tip distances L the curve is significantly shifted to lower frequencies compared to the case of flat side walls. This shift is not a monotonous function of L. The maximum shift occurs for $L = 20\,\text{mm}$, for smaller and larger tip distances the shift is less pronounced. This is consistent with the limiting cases of L. For $L \to 0$, the effect of the corrugation vanishes and the "corrugated" system converges to a "flat" system with channel width B. Also for $L \to \infty$, the system converges to a system with flat side walls, but with the channel width $B + 2l_t$. The different channel width in the two limiting cases leads to a small difference in the damping frequency for $L \to 0$ and $L \to \infty$, but this difference is much smaller than the shift caused by the side wall corrugation. This is analogous to the shift in the critical Reynolds number, see section 4.3.1.2 and particularly fig. 4.10. A detailed study of the limiting cases can be found in appendix A.3.

In this section it was shown, that the newly found damping is not an effect of flat side walls exclusively, but of side walls in general. Corrugated side walls show qualitatively the same phenomenon, whereas the damping frequency shifts to significantly lower values.

4.3.3 Conclusions

In summary, section 4.3 showed that the presence of side walls, whether flat or corrugated, has two effects on the stability of film flows: First, the critical Reynolds number that defines the onset of the instability for infinite long waves is shifted to higher values compared to the two-dimensional flow. Second, the general shape of the stability chart changes dramatically and a fragmentation of the neutral curve can occur.

A stabilization of the flow is caused by the presence of side walls. This stabilization can be seen in the shift of the critical Reynolds number of the three dimensional channel flow compared to the theoretically obtained value of the two-dimensional flow. It was shown that the shift vanishes for infinite wide channels which is consistent with the transition of the channel flow to the plane flow, which is identical to the two-dimensional flow. On the other hand, a reduction of the channel width causes a greater shift of the critical Reynolds number and therefore a greater stabilization of the flow. This effect is qualitatively the same for flat and corrugated side walls whereas the shift is significantly more pronounced if the side walls are corrugated.

The stabilizing effect of corrugated side walls strongly depends on the streamwise length scale of the corrugations. In the limits of very small and very large tip distances the corrugated walls

converges to flat walls. Therefore the shift of the critical Reynolds number converges to the value of flat side walls for these limits. For intermediate tip distances a strong maximum in the stabilization could be observed.

The stabilizing effect of side walls could be brought together with the effect on the basic flow. In the vicinity of the side walls excited waves are damped [53]. Since the fraction of the fluid which is affected by the side walls increases if the channel width is reduced, this "damping area" increases for small channels and the flow is generally more stable. Moreover, the "damping area" increases significantly for corrugated side walls, which explains the correspondingly stronger damping. In the limit of very long and very short tip distances, the effect of corrugated side walls on both the basic flow and the stability are the same as for flat side walls.

The way more astonishing result of section 4.3 is the occurrence of a fragmentation of the neutral curve. The side walls cause a selective damping of waves within a specific frequency range. The frequency of the maximum damping, the *damping frequency*, mainly depends on the channel width but barely on other system parameters. The greater the channel width, the lower the damping frequency. Therefore the wavelength of the damped waves increases with the channel width. In the limit of very large channel widths, the flow transitions to the plane flow and the damping effect vanishes. The damping effect is generally unrelated to the stability of the corresponding plane flow without side walls. In other words, the stability map of the channel flow is qualitatively the same as the one of the plane flow, but with an additional damping at a certain frequency range that is caused by the side walls.

For corrugated side walls this damping effect also occurs. Yet, the damping frequency is significantly shifted to lower values. Thus, for corrugated side walls longer waves are damped compared to flat side walls. This shift, however, vanishes for very small and very large tip distances.

The occurrence of fragmented stability charts is known from film flows over undulated substrates. But to the author's knowledge it has never been observed in a channel flow with flat side substrate and flat side walls. With the findings so far the behavior of the channel flow cannot be explained. Therefore additional measurements are required which will be presented in the following section.

The damping effect presented in this section could be used to stabilize film flows in technical applications. For a certain wavelength range a massive stabilization can be achieved up to arbitrary high Reynolds numbers—at least within the measurement range. Moreover, the damping wavelength can be tuned by varying the channel width or by attaching appropriate side wall corrugations when the channel width is fixed.

4.4 Influence of side walls on the wave shape

This section is focused on the interaction between the side walls and the surface waves excited by the paddle. Since waves in a channel of finite width are not strictly two-dimensional, the transverse influence of the side walls on the flow is of great interest. It is reported that the side walls affect the shape of the wave [51, 55]. To be precise, the crest line of a wave in a channel is curved (see e.g. fig. 3.13), whereby the curvature depends on the channel width. Section 4.4.1 includes a study of the interaction between the side walls and the wave shape. Side walls do not only influence the wave shape, but also massively affect the growth rate of the wave, as examined in section 4.3. So the question arises: Is there any relation between the damping of the wave and the curvature of its crest line? This question will be discussed in section 4.4.2.

4.4.1 Characterization of the wave shape

The wave shape is defined by the curvature k of the center half of the wave's crest line (see Section 3.3.3). First of all the influence of the wave's amplitude on the crest line curvature was investigated. For the measurement of the curvature k large amplitudes and therefore nonlinear waves are needed. On the other hand, for the measurement of the stability small amplitudes and therefore linear waves are necessary. Thus, it is necessary to know if the wave's amplitude has any impact on the curvature k. In fact, the curvature of the crest line is independent of the amplitude, as demonstrated in fig. 4.22. Several measurements with different paddle amplitudes A were performed, which result in different wave amplitudes at the measurement position. As one can see, the curvature k, displayed in the inlay of fig. 4.22, is constant for all amplitudes. The experiment was repeated with different frequencies from 3 Hz to 9 Hz (only the data for $f = 9\,\mathrm{Hz}$ is shown) and all results show that the curvature k is independent of the amplitude. Therefore, the same curvature can be assumed for linear waves.

The dependency of the wave shape on the excitation frequency f is shown in fig. 4.23 for two different channel widths. The qualitative shape of the wave remains the same, whereas the measured center curvature k (displayed in the inlets of fig. 4.23(a) and (b)) shows the astonishing result that k is not a monotonous function of f, but shows a distinct maximum. Very long and very short waves have a smaller curvature than waves of intermediate length.

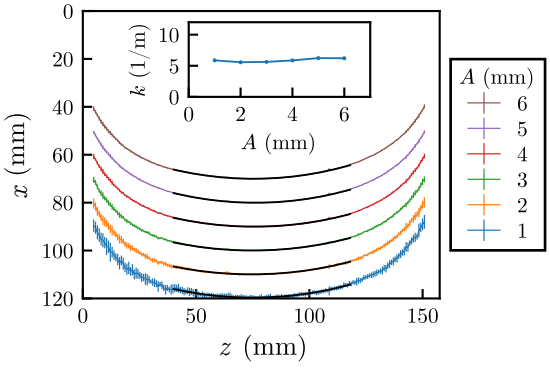

Figure 4.22: Averaged crest lines of waves with excitation frequency $f = 9\,\mathrm{Hz}$ and different paddle amplitudes A. The channel width is $B = 158\,\mathrm{mm}$, denoted by the right border. The different lines are shifted for a better display. The solid black lines show the quadratic fits (see eq. (3.15)) over the center half of each crest line. The dependency of the curvature k on the paddle amplitude A is shown in the inlet. The measurements were performed with the fluid *Elbesil 140* at $\alpha = 10°$ and $\mathrm{Re} = 40$. © Springer Nature

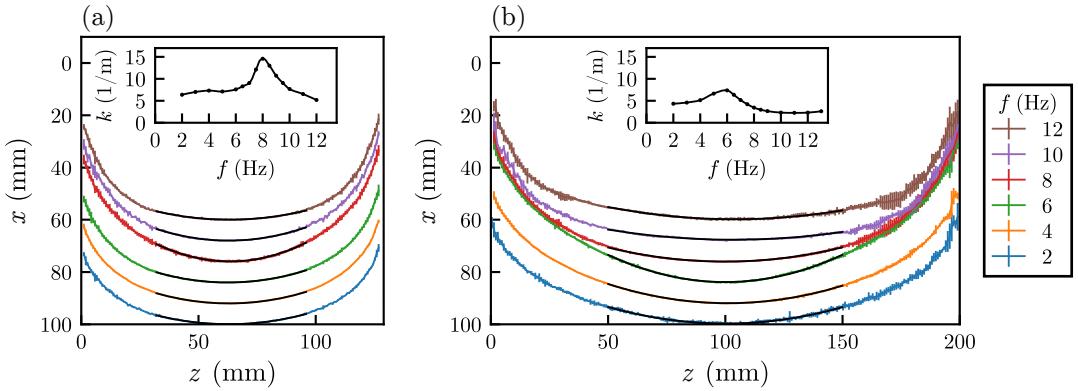

Figure 4.23: Averaged crest lines of waves with different excitation frequencies f and two different channel widths (a) $B = 129\,\mathrm{mm}$ and (b) $B = 200\,\mathrm{mm}$. The individual lines are shifted for a better display. The solid black lines show the quadratic fits over the center half of each crest line. The dependency of the curvature k on the frequency f is shown in the inlet. The measurements were performed with the fluid *Elbesil 140* at $\alpha = 10°$ and $\mathrm{Re} = 30$.

The decreasing of k at high frequencies is consistent with the findings of Leontidis et al. [55] but a maximum in the curvature was not yet reported.

A more detailed plot of the frequency dependency on k is displayed in fig. 4.24 for multiple channel widths. As one can see, the position of the maximum shifts to lower frequencies when increasing the channel width. Furthermore, with increasing channel width the height of the maximum decreases as well as the curvature in general. This is consistent with the limiting case $B \to \infty$ where the side walls do not have any influence on the flow. In this limit the primary instability leads to plane waves with zero curvature. A secondary instability, where periodic wave front modulations may occur [76], was not observed.

For a better understanding of the interaction between wave and side walls, the relation between the curvature and the wavelength can be investigated. Both quantities could be nondimensioned by the channel width B. Fig. 4.25 shows the dimensionless curvature kB as a function of the dimensionless wavelength λ/B for several channel widths. For small wavelengths ($\lambda/B < 0.75$) all curves coincide in one single band that is highlighted in subfig. (a). On the other hand for large wavelengths the curvature is almost independent of the wavelength but depends on the channel width. The waves therefore can be categorized into different regimes: a *short wave*

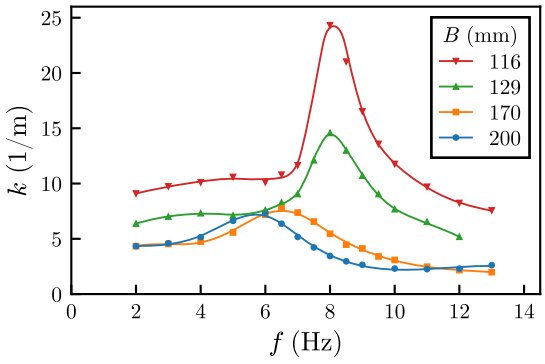

Figure 4.24: Curvature k as a function of the excitation frequency f for different channel widths. The solid lines are guides to the eye. The measurements were performed with *Elbesil 140* at $\alpha = 10°$ and $\mathrm{Re} = 30$.

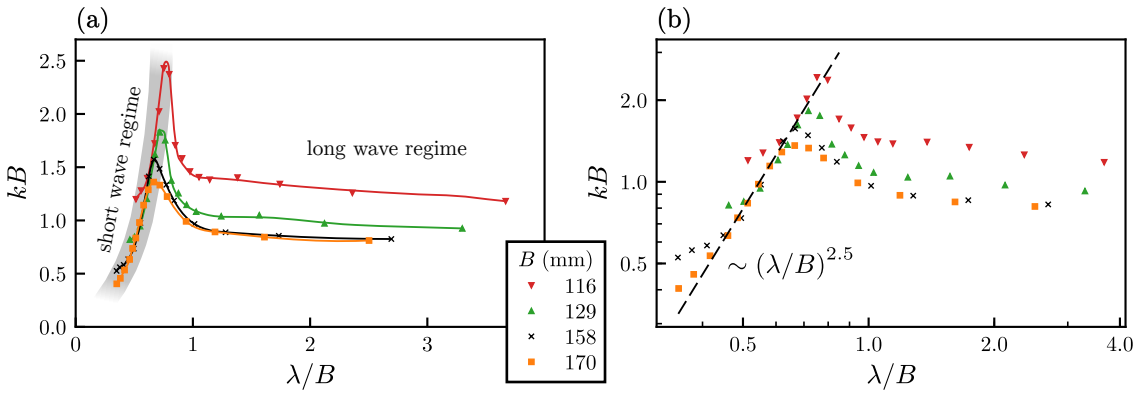

Figure 4.25: Dimensionless curvature kB as a function of the dimensionless wavelength λ/B: (a) linear scale, (b) logarithmic scale. The solid lines are guides to the eye. The grey shaded band in (a) highlights the coincidence of the curves. The dashed line in (b) shows a power law function. The measurements were performed with *Elbesil 140* at $\alpha = 10°$ and $\mathrm{Re} = 30$.

regime ($\lambda < 0.75B$), where the curvature depends on the ratio λ/B, and a *long wave regime* ($\lambda > B$), where the curvature depends mainly on the channel width. In between these regimes a transition takes place.

In the short wave regime, i.e. for waves with $\lambda < 0.75B$, the curvature does only depend on the ratio of the wavelength and the channel width. This dependency can be described approximately by a power law function with the exponent 2.5, which is displayed by the dashed line in fig. 4.25(b). Leontidis et al. [55] assumed a linear dependency between kB and λ/B. This could be, at least for the given experimental system, disproved.

At very short wave lengths another regime may occur, since for every channel width the data points most left in fig. 4.25(b) do not match the power law function. Unfortunately, no measurements with smaller wavelengths were possible because such short waves were strongly damped and the wave crest was not detectable at the measurement position.

When λ/B exceeds a certain value that depends on the channel width B, the dimensionless curvature kB passes a maximum and decreases to an almost constant value in the long wave regime. The position and the height of the maximum as well as the constant curvature for long waves strongly depend on the channel width.

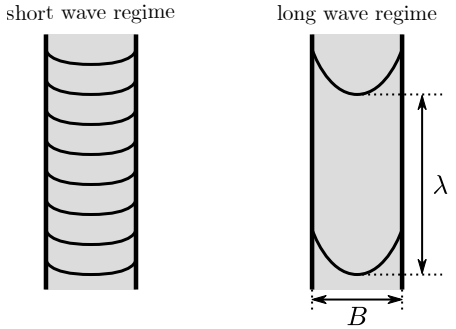

Figure 4.26: Exemplary sketch of wave crests in the short wave regime ($\lambda/B = 0.3$) and the long wave regime ($\lambda/B = 2$).

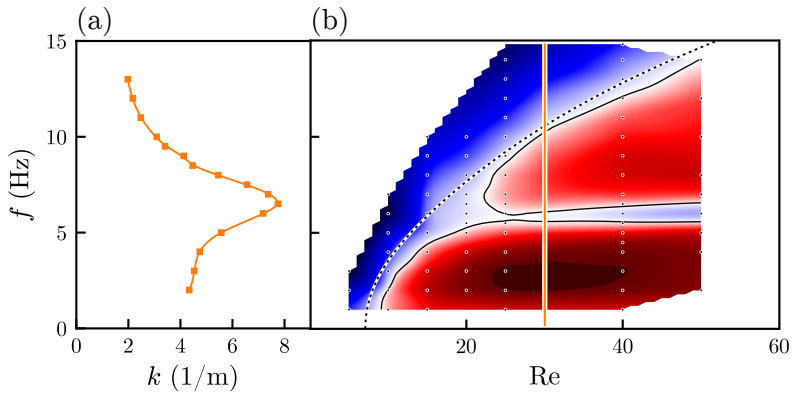

Figure 4.27: (a) Relation between the excitation frequency f and the curvature k for $B = 170\,\mathrm{mm}$, $\mathrm{Re} = 30$ and $\alpha = 10°$. The fluid was *Elbesil 140*. (b) Corresponding stability chart (c.f. fig. 4.12(g)). The straight line highlights the Reynolds number $\mathrm{Re} = 30$ used in (a). © Springer Nature

In the long wave regime, the wavelength has almost no influence on the curvature, the decisive parameter is the channel width. A possible explanation for this effect could be, that the distance between two subsequent wave crests is larger than the channel width and therefore a single wave crest only interacts with the side walls but not with other wave crests. On the other hand, in the short wave regime the interaction between subsequent wave crests dominates the shape of the wave crest and the channel width has no direct influence on the curvature. Summing up, the short wave regime is mainly dominated by the interaction between subsequent wave crests and the long wave regime is mainly dominated by the interaction between the wave and the side walls. Please see fig. 4.26 for a sketch of the wave crests in the short wave and the long wave regime. The question why the two regimes are divided by a maximum in the curvature, however, remains an important topic for future work.

4.4.2 Does the wave shape affect the stability of the basic flow?

Now the relation between the damping of a wave and the curvature of its crest line will be discussed. The occurrence of an unexpected maximum in the curvature k at a certain frequency is interesting, particularly because the corresponding stability chart shows an unexpected damping at a similar frequency. In fig. 4.27(a) one exemplary curve of fig. 4.24—rotated by 90°—is shown. The corresponding stability chart is depicted in subfig. (b), where the Reynolds number that was used in subfig. (a) is highlighted.

This matching of the maximum in the curvature and the minimum in the growth rate occurs for all channel widths. Fig. 4.28 shows (a) the growth rate b and (b) the curvature k as a function of f for several channel widths B. The arrows indicate the positions of the maxima and minima respectively. As one can see, these positions are at similar frequencies and show the same trend when changing the channel width. The curvature of a wave's crest line correlates to the wave's growth rate. Note here that the maximum of the curvature is generally shifted to slightly higher frequencies ($0.5 - - 1.0\,\mathrm{Hz}$) compared to the minimum of the growth rate. One could assume that strongly curved waves are damped more than plane waves. But since the maximum in the curvature and the minimum in the growth rate are not at the same frequency,

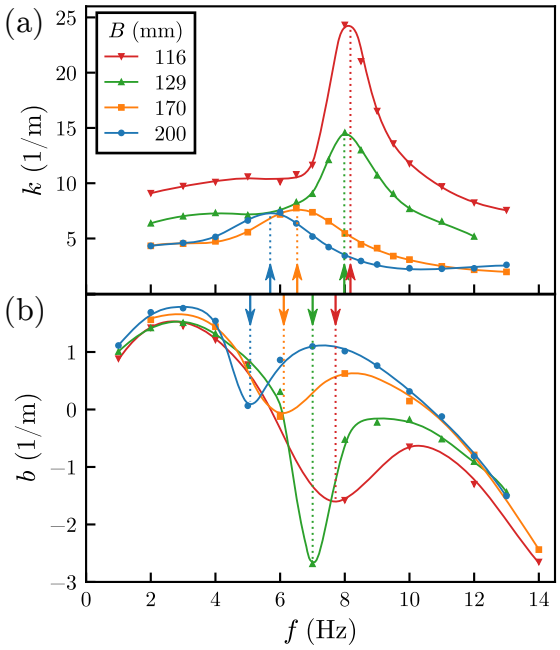

Figure 4.28: (a) Curvature k of the crest line and (b) growth rate b as functions of the excitation frequency f for different channel widths B at $\mathrm{Re} = 30, B = 170\,\mathrm{mm}$ and $\alpha = 10°$. The fluid was *Elbesil 140*. The arrows highlight the frequency of the maximum curvature the frequency of the minimum growth rate, respectively. © Springer Nature

this simple assumption has to be refused. It is more likely that there is another reason for the correlation. Maybe the interaction between the wave shape and its growth rate is more complex and additional parameters have to be taken into account. Another possible explanation could be an unknown underlying mechanism that influences both the curvature of the wave and the damping separately.

4.4.3 Conclusions

Section 4.4 dealt with the shape of the free surface waves in the channel flow. It was shown that the wave's crest has a parabolic shape that can be quantified by its curvature. The curvature does not depend on the amplitude but it significantly depends on the channel width and the wavelength. Small channels cause strongly curved waves whereas in the limit of very large channel widths the curvature tends to zero which is consistent to the transition of the channel flow to the plane flow. The dependency of the curvature on the wavelength is more complex. If the wavelength is much larger than the channel width, the interaction between wave and side walls outweighs the interaction of two subsequent waves and therefore the curvature depends only on the channel width but not on the wavelength. On the other hand, if the wavelength is much smaller than the channel width the wave shape is dominated by the interaction with neighboring waves and is independent of the channel width. For intermediate wavelengths in between these two regimes, an unexpected maximum of the curvature occurs.

The frequencies of the waves with maximum curvature are very similar to the corresponding *damping frequencies* presented in section 4.3.2. That means that the waves with strongly curved crest lines are the same waves that undergo the unexpected selective damping. Yet, the frequency of the maximum curvature is always $0.5 - 1.0\,\mathrm{Hz}$ higher than the damping frequency. In other words, the length of maximally curved waves is slightly smaller than the corresponding

damping wavelength. On the basis of these observations, it can just be speculated that there is a relationship between the curvature k and the growth rate b of a wave in a channel flow. However, the exact interaction between a wave's shape and the stability of its underlying basic flow as well as the physical background of both phenomena are highly complex and require further investigations.

5 Summary and Conclusions

The present thesis provides new insights into the effects of side walls on gravity-driven viscous film flows. In particular, the primary stability of the channel flow, i.e. a film flow restrained by side walls, was experimentally investigated. Additionally, the basic steady state flow was measured as well as the properties of the emerging free surface waves. The findings were compared to the theoretical results for the plane flow of infinite extent. It was found that side walls play a much more important role in the stability of film flows than previously assumed. The aim of this thesis was to unveil the new stability phenomena, but also to provide a detailed parameter study to characterize them and to find the decisive parameters to control the stability of the channel flow.

The presence of side walls causes multiple effects on the film flow compared to the plane flow of infinite extent: First, the steady state flow is affected due to the interaction with the side walls. Second, flow is generally stabilized. In particular the critical Reynolds number is shifted to higher values, depending on the channel width and the side wall configurations. Third, the entire shape of the neutral curve is changed due to a selective damping of certain waves. And fourth, the crest line of the excited waves are curved due to the friction at the side walls. These four findings are generally not unrelated. However, the physical interaction between the side walls, the basic flow and the free surface waves are highly complex and not completely understood yet. Therefore this thesis provides some explanatory approaches to link the found effects in a consistent way.

All experimental and theoretical approaches to film flows assume a fully developed steady state flow that remains constant in the flow direction. However, with the channel used in the present experiments an inflow area, where the flow is developing until it reaches its fully developed state, is unavoidable. Therefore it had to be ensured that this inflow area is sufficiently small and the flow at the measurement position is fully developed. To this end, the film thickness was measured along the center of the channel. It was found that the film thickness shows an overshoot at the inlet of the channel caused by the inertia of the fluid. This overshoot decays after a few hundred millimeters, depending on the Reynolds number, and the film thickness asymptotically reaches its final state. Additional measurements showed that the surface velocity increases asymptotically along the center of the channel and reaches its final value in a similar distance as the film thickness. The position for all further measurements was chosen far enough away from the inlet that all inflow effects have completely decayed and the flow is fully developed.

The basic steady state flow in a channel with flat side walls is mathematically identical to the well known velocity field of a flow through a rectangular pipe where the free surface of the channel flow corresponds to the symmetry plane of the pipe flow. This is only valid since the film thickness is sufficiently high and the Kapitza number sufficiently low and therefore the capillary

elevation at the side walls is negligible. In the vicinity of the side walls the fluid is slowed down—compared to the plane flow—due to the no-slip condition, but in the center of the channel the flow profile is almost perfectly parabolic—as for the plane flow. So, the influence of the side walls on the basic flow is limited to a certain area. If corrugations are attached to the side walls, the influence of the side walls reaches further into the flow, depending on the streamwise length scale of the corrugations. In the limit of very small and very large corrugation lengths, the flow converges to the flow within flat side walls, whereas at intermediate length scales the area affected by the side walls is maximal.

Since the measured stability charts are generally quite complex, it is beneficial to extract a single essential quantity from them: in this case the critical Reynolds number was chosen at which the flow for infinite long waves becomes unstable. The critical Reynolds number strongly depends on the channel width. For very large channel widths it is only slightly higher than its value for the plane flow of infinite extent. But for decreasing channel widths the critical Reynolds number increases significantly, i.e. the flow is strongly damped. Eventually the critical Reynolds number even diverges for small channels. However, because of the strong damping in such small channels a reliable measurement was not possible. Moreover, if the channel width is of the same order of magnitude as the film thickness, the assumption of a film flow is no longer valid and the physical model itself has to be reconsidered. The stabilization of the steady state flow can be explained by the influence of the side walls. In the vicinity of the side walls waves were observed to be damped [53]. The volume of the fluid that is affected by the side walls is independent of the channel width but the whole fluid volume decreases for smaller channel widths. Therefore the fraction of the fluid affected by the side walls increases if the channel width is decreased and the excited waves are damped more strongly. In the limit of infinite wide channels the influence of the side walls vanish and so does the shift of the critical Reynolds number.

The effect of a shifted critical Reynolds number occurs for flat as well as corrugated side walls. However, for corrugated side walls the shift is significantly stronger, though the influence of the corrugations vanishes if its streamwise length scale is very small or very large. This matches the behavior of the basic flow which is affected more strongly by corrugated side walls than by flat side walls, depending on the length scale of the corrugations.

The effect of side walls on the whole stability chart is more complex. The presence of side walls causes—in comparison to the plane flow—a selective damping of waves within a small frequency range or respectively a small wavelength range. The *damping wavelength* strongly depends on the channel width but barely on other system parameters. The wider the channel, the larger the wavelength of the damped waves. However, for very wide channels, the damping itself vanishes since the channel flow transitions to the plane flow where the side walls no longer have any impact. For corrugated side walls the damping effect is in general the same as for flat side walls, yet the damping wavelength is significantly larger. This shift again vanishes for small and large corrugation lengths. The damping can be seen as an additional effect on the flow, since it is completely unrelated to the instability of the underlying plane flow. That means, the damping occurs whether the steady state plane flow is stable or unstable. Therefore it is an effect caused solely by the presence of the side walls.

Now the question is posed: Why is there a relation between a transverse length like the channel width and a longitudinal length like the damping wavelength? To this end, the shape of the

emerging wave was measured and a curved wave crest was found. The curvature of the parabolic crest line generally depends on both the channel width and the wavelength. For short waves it was found that the curvature is determined by the distance between two subsequent waves—i.e. the wavelength. The shorter the waves, the less curved they are. For long waves two subsequent wave crests are too far apart and the curvature is determined only by the channel width. For wider channels the curvature decreases. In the limit of an infinite wide channel the curvature tends to zero since the channel flow transitions to the plane flow, in which only plane waves occur. Interestingly, the curvature is not a monotonous function of the wavelength. The short wave and the long wave regime are separated by a distinct maximum in the curvature. In other words, there is an intermediate wavelength at which the wave crest is maximally curved.

The lengths of the waves with maximum curvature are very similar to the corresponding damping wavelengths. That means that the waves with strongly curved crest lines are the same waves that undergo the unexpected selective damping. Yet, the wavelength of the maximum curvature is always slightly smaller than the damping wavelength. On the basis of these observations, it can just be speculated that there is a relationship between the curvature and the growth rate of a wave in a channel flow. However, the exact interaction between a wave's shape and the stability of its underlying basic flow as well as the physical background of both phenomena are highly complex and require further investigations.

The damping effects presented in this thesis could be suitable for technical applications that require undisturbed film flows. First of all, a general damping can be achieved by adding side walls. A particularly strong damping can be obtained by using corrugated side walls with a suitable corrugation length. Second, it is possible to achieve selective damping for a certain wavelength range up to arbitrarily high Reynolds numbers—at least within the measurement range of the experiments presented in this thesis. Moreover, it is possible to tune the damping wavelength either by changing the channel width or, in case of a fixed channel width, by adding suitable side wall corrugations.

Although many new insights in the interaction of side walls and film flows were given in this thesis, various open questions remain and new questions arise. What are the exact physical reasons for the selective damping? And why is there a maximum curvature at a certain wavelength? Is the maximum curvature the cause of the damping or are both effects of an unknown mechanism? A deeper understanding of wall-fluid and in particular wall-wave interaction is needed to unveil the complex dynamics of gravity driven viscous open-channel flows.

Appendix

A.1 Transfer of the boundary conditions

For the transfer of the boundary conditions eqs. (2.24), (2.39) and (2.40) from $y^* = h^*$ to $y^* = 1$ a first order Taylor approximation of all the quantities present in the equations around $y^* = 1$ is done. Then the quantities at $y^* = h^* = 1 + \varepsilon\hat{h}$ can be expressed by quantities at $y^* = 1$.

$$\begin{aligned} U^*\Big|_{y^*=h^*} &\approx U^*\Big|_{y^*=1} + \partial_{y^*}U^*\Big|_{y^*=1}\varepsilon\hat{h} &&= U^*\Big|_{y^*=1} \\ \partial_{y^*}U^*\Big|_{y^*=h^*} &\approx \partial_{y^*}U^*\Big|_{y^*=1} + \partial^2_{y^*}U^*\Big|_{y^*=1}\varepsilon\hat{h} &&= \partial^2_{y^*}U^*\Big|_{y^*=1}\varepsilon\hat{h} \end{aligned}$$

Although the transfer has no impact on U^*, it does have an effect on its derivative $\partial_{y^*}U^*$.

$$\begin{aligned} P^*\Big|_{y^*=h^*} &\approx P^*\Big|_{y^*=1} + \partial_{y^*}P^*\Big|_{y^*=1}\varepsilon\hat{h} &&= \partial_{y^*}P^*\Big|_{y^*=1}\varepsilon\hat{h} \\ \varepsilon\hat{u}\Big|_{y^*=h^*} &\approx \varepsilon\hat{u}\Big|_{y^*=1} + \varepsilon\partial_{y^*}\hat{u}\Big|_{y^*=1}\varepsilon\hat{h} &&\approx \varepsilon\hat{u}\Big|_{y^*=1}. \end{aligned}$$

The transfer of $\varepsilon\hat{v}$ and $\varepsilon\hat{p}$ and all derivatives of them is analogous to the latter equation and has no impact on the quantities.

A.2 The dimensionless stress vector

The dimensioned stress vector is defined as

$$\begin{aligned} \vec{t} &= 2\eta E \cdot \vec{n} - p\vec{n} \\ &= \eta\left(\nabla\vec{u} + (\nabla\vec{u})^\mathsf{T}\right)\cdot\vec{n} - p\vec{n} \end{aligned}$$

where E is the strain rate tensor

$$E = \frac{1}{2}\left(\nabla\vec{u} + (\nabla\vec{u})^\mathsf{T}\right).$$

All quantities are now nondimensioned according to eqs. (2.6) through (2.9):

$$\vec{t}^* = \frac{\vec{t}}{\rho U_{\text{surf}}^2}, \qquad \nabla^* = H\nabla, \qquad \vec{u}^* = \frac{\vec{u}}{U_{\text{surf}}}, \qquad p^* = \frac{p}{\rho U_{\text{surf}}^2}.$$

Therefore

$$\vec{t}^{\,*}\rho U_{\text{surf}}^2 = \eta\frac{U_{\text{surf}}}{H}\left(\nabla^*\vec{u}^{\,*} + (\nabla^*\vec{u}^{\,*})^{\mathsf{T}}\right)\cdot\vec{n} - p^*\rho U_{\text{surf}}^2\vec{n}$$
$$\vec{t}^{\,*} = 2\frac{\eta}{\rho U_{\text{surf}}H}E^*\cdot\vec{n} - p^*\vec{n}\,.$$

With the definition of the Reynolds number eq. (2.10), the dimensionless stress vector is

$$\vec{t}^{\,*} = \frac{2}{\text{Re}}E^*\cdot\vec{n} - p^*\vec{n}\,.$$

A.3 Limiting cases for the tip distance

Fig. A.1 shows the two limits for the tip distance L. For $L \to 0$ the tip distance is reduced until the tips touch each other and therefore form a flat side wall. For this case the channel width remains B, which is the same channel width as for corrugated side walls. In the limit $L \to \infty$ the distance between the tips becomes infinitely large and therefore the tips do not longer have any influence on the stability of the flow. This also corresponds to flat side walls. In this limit, however, the real channel width is larger than in the limit $L \to 0$. The difference is two times the tip length $\Delta B = 2\,l_{\text{t}}$.

When comparing the critical Reynolds numbers $\text{Re}_{\text{crit}}(B, L)$ for different tip distances (including the two limiting cases) it is necessary to use the same definition of the Reynolds number and therefore one has to stick to the identical channel width B for all measurements. This is trivial for all cases except for the limit $L \to \infty$: In this special case a measurement with flat walls and the channel width $B + \Delta B$ was done separately (see fig. 4.9(a)), but in this case also the

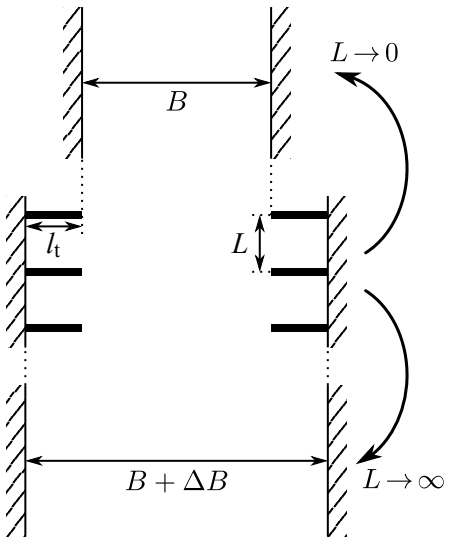

Figure A.1: Limiting cases for the tip distance $L \to 0$ and $L \to \infty$.

Table A.1: Example for the different critical Reynolds numbers for the limiting cases of L.

$B\,(\mathrm{mm})$	$B+\Delta B\,(\mathrm{mm})$	$\mathrm{Re}_{\mathrm{crit}}(B, L\to 0)$	$\mathrm{Re}_{\mathrm{crit}}(B+\Delta B, L\to 0)$	$\mathrm{Re}_{\mathrm{crit}}(B, L\to\infty)$
84	100	9.78	9.16	10.90

Table A.2: Example for the different stability shifts for the limiting cases of L.

$B\,(\mathrm{mm})$	$\epsilon(B, L\to 0)$	$\epsilon(B, L\to\infty)$	$\epsilon(B, L=20\,\mathrm{mm})$
84	0.38	0.54	1.90

calculation of the Reynolds number was done using the channel width $B+\Delta B$. This result cannot be easily compared to $\mathrm{Re}_{\mathrm{crit}}(B, L)$ since

$$\mathrm{Re}_{\mathrm{crit}}(B, L\to\infty) \neq \mathrm{Re}_{\mathrm{crit}}(B+\Delta B, L\to 0)\,.$$

Since for this measurement another definition of the Reynolds number was used, the result has to be adapted to the definition using the channel width B. From the measured critical Reynolds number $\mathrm{Re}_{\mathrm{crit}}(B+\Delta B, L\to 0)$ one can calculate the corresponding film thickness (see section 3.1.2) and therefrom the volume flux $\dot{V}$ (using the channel width $B+\Delta B$). From the so obtained volume flux one can now calculate the Reynolds number $\mathrm{Re}_{\mathrm{crit}}(B, L\to\infty)$ using the channel width B. A numerical example for the different critical Reynolds numbers is given in tab. A.1. The stability shift ϵ can now be calculated using eq. (4.2).

Table A.2 shows an example for the stability shift ϵ in the two limiting cases of L and an intermediate tip distance. The difference between $\epsilon(B, L\to 0)$ and $\varepsilon(B, L\to\infty)$ is not zero but rather small compared to the stability shift for $L=20\,\mathrm{mm}$.

List of Symbols

symbol	unit	description
α	$^\circ$	inclination angle
ϵ		instability shift
ε		magnitude of the linear disturbance
η	$\mathrm{Pa\,s}$	dynamic viscosity
κ^*		dimensionless curvature of the fluid surface
λ	m	wavelength
λ^*		dimensionless wavelength
λ_{min}	Hz	wavelength of the local minimum of the growth rate
ν	$\mathrm{m^2 s^{-1}}$	kinematic viscosity
ρ	$\mathrm{kg\,m^{-3}}$	fluid density
ρ_{P}	$\mathrm{kg\,m^{-3}}$	density of tracer particles
σ	$\mathrm{N\,m^{-1}}$	surface tension
φ_1, φ_2		phase of oscillation of laser spots
$\Delta\varphi$		real phase difference between the laser oscillations
$\Delta\varphi_0$		measured phase difference between the laser oscillations
$\Psi_0, ..., \Psi_3$		derivatives of the dimensionless stream function
$\widehat{\psi}$		dimensionless stream function
$\widehat{\psi}_0, \widehat{\psi}_1$		zeroth (first) order approximation of the dimensionless stream function
ω^*		dimensionless angular frequency
A	m	oscillation amplitude of the paddle
A_1, A_2	m	position of laser spots
A_1^0, A_2^0	m	oscillation amplitude of laser spots
$A_{2,\mathrm{corr}}^0$	m	corrected amplitude of second laser spot
B	m	channel width
b	$\mathrm{m^{-1}}$	spatial growth rate
b_{s}^*		dimensionless spatial growth rate
b_{t}	m	width of tips
b_{t}^*		dimensionless temporal growth rate
b_{3D}	$\mathrm{m^{-1}}$	growth rate of the channel flow
b_{2D}	$\mathrm{m^{-1}}$	growth rate of the plane flow
Δb	$\mathrm{m^{-1}}$	difference between b_{3D} and b_{2D}
c	$\mathrm{m\,s^{-1}}$	phase velocity
c^*		dimensionless phase velocity
c_0^*, c_1^*		zeroth (first) order approximation of the dimensionless phase velocity
$c_{\mathrm{r}}^*, c_{\mathrm{i}}^*$		real and imaginary part of the dimensionless phase velocity
d_{P}	m	median diameter of tracer particles
E	$\mathrm{m\,s^{-2}}$	strain rate tensor

symbol	unit	description
E^*		dimensionless strain rate tensor
$\vec{F}_0, \vec{F}_1$		boundary conditions for the dimensionless stream function
f	Hz	wave frequency, excitation frequency
$f_{\min}$	Hz	frequency of the local minimum of the growth rate
$\vec{e}_x, \vec{e}_y$		unit vector in x- and y-direction
g	$\mathrm{m\,s^{-2}}$	gravitational acceleration
H	m	undisturbed fully developed film thickness
h	m	film thickness
h^*		dimensionless film thickness
$\hat{h}$		dimensionless disturbance of the film thickness
$\hat{h}_0$		amplitude of the dimensionless disturbance of the film thickness
Ka		Kapitza number
k	$\mathrm{m^{-1}}$	curvature of the wave's crest line
k^*		dimensionless wave number
$k_\mathrm{r}^*, k_\mathrm{i}^*$		real and imaginary part of the dimensionless wave number
L	m	tip distance
L_cap	m	capillary length
l_t	m	length of tips
l_{50}	m	measured inflow length
$\vec{m}$		tangential vector to the fluid surface
$\vec{n}$		normal vector to the fluid surface
n		number of full waves between the two reflection spots
P	$\mathrm{N\,m^{-2}}$	undisturbed pressure of the plane flow
P^*		undisturbed dimensionless pressure of the plane flow
p	$\mathrm{N\,m^{-2}}$	pressure of the plane flow
p^*		dimensionless pressure of the plane flow
$\hat{p}$		dimensionless disturbance of the pressure
$\hat{p}_0$		amplitude of the dimensionless disturbance of the pressure
Re		Reynolds number
$\mathrm{Re_{crit}}$		critical Reynolds number
$\mathrm{Re_{crit,2D}}$		critical Reynolds number of the plane flow
$\mathrm{Re_n}$		neutral Reynolds number
$\mathrm{Re_{n,2D}}$		neutral Reynolds number of the plane flow
T	°C	fluid temperature
$\vec{t}_1^*, \vec{t}_2^*$		dimensionless stress vectors
t	s	time
t^*		dimensionless time
Δt	s	time delay of the laser oscillations
U	$\mathrm{m\,s^{-1}}$	undisturbed velocity of the plane flow in x-direction
U^*		undisturbed dimensionless velocity of the plane flow in x-direction
U_surf	$\mathrm{m\,s^{-1}}$	undisturbed surface velocity of the plane flow
$U_\mathrm{surf,center}$	$\mathrm{m\,s^{-1}}$	fully developed surface velocity in the center of the channel
$\vec{u}$	$\mathrm{m\,s^{-1}}$	fluid velocity
$\vec{u}^*$		dimensionless fluid velocity
u^*		dimensionless velocity of the plane flow in x-direction

symbol	unit	description
$\hat{u}$		dimensionless disturbance of the velocity in x-direction
$\hat{u}_0$		amplitude of the dimensionless disturbance of the velocity in x-direction
u_{sed}	$\mathrm{m\,s^{-1}}$	sedimentation speed of tracer particles
u_{surf}	$\mathrm{m\,s^{-1}}$	surface velocity
$u_{\mathrm{surf,center}}$	$\mathrm{m\,s^{-1}}$	surface velocity in the center of the channel
$\dot{V}$	$\mathrm{m^3\,s^{-1}}$	volume flux
v	$\mathrm{m\,s^{-1}}$	absolute value of the velocity in the center plane of the channel
v^*		dimensionless velocity of the plane flow in y-direction
$\hat{v}$		dimensionless disturbance of the velocity in y-direction
$\hat{v}_0$		amplitude of the dimensionless disturbance of the velocity in y-direction
We		Weber number
x	m	streamwise coordinate
x^*		dimensionless streamwise coordinate
x_1	m	distance between channel inlet and first reflection spot
Δx	m	distance between the two reflection spots
x_{s}	m	distance between the second reflection spot and the screen
x_{crest}	m	position for measuring the wave shape
y	m	coordinate perpendicular to the bottom
y^*		dimensionless coordinate perpendicular to the bottom
z	m	spanwise coordinate

List of Figures

List of Tables

References

[1] S. F. Kistler and P. M. Schweizer, *Liquid Film Coating* (Springer, Dodrecht, 1997).

[2] S. J. Weinstein and K. J. Ruschak, "Coating Flows", Annu. Rev. Fluid Mech. **36**, 29–53 (2004) 10.1146/annurev.fluid.36.050802.122049.

[3] G. Gugler, R. Beer, and M. Mauron, "Operative limits of curtain coating due to edges", Chem. Eng. Process. Process Intensif. **50**, 462–465 (2011) 10.1016/j.cep.2011.01.010.

[4] R. L. Webb, *Principles of Enhanced Heat Transfer* (John Wiley & Sons, New York, 1994).

[5] P. Vlasogiannis, G. Karagiannis, P. Argyropoulos, and V. Bontozoglou, "Air-water two-phase flow and heat transfer in a plate heat exchanger", Int. J. Multiphase Flow **28**, 757–772 (2002) 10.1016/S0301-9322(02)00010-1.

[6] R. Greve and H. Blatter, *Dynamics of Ice Sheets and Glaciers* (Springer, Berlin, Heidelberg, 2009).

[7] I. Luca, K. Hutter, Y. C. Tai, and C. Y. Kuo, "A hierarchy of avalanche models on arbitrary topography", Acta Mech. **205**, 121–149 (2009) 10.1007/s00707-009-0165-4.

[8] K. Hutter, B. Svendsen, and D. Rickenmann, "Debris flow modeling: A review", Continuum Mech. Thermodyn. **8**, 1–35 (1994) 10.1007/BF01175749.

[9] A. Kumar, D. Karig, R. Acharya, S. Neethirajan, P. P. Mukherjee, S. Retterer, and M. J. Doktycz, "Microscale confinement features can affect biofilm formation", Microfluid. Nanofluid. **14**, 895–902 (2013) 10.1007/s10404-012-1120-6.

[10] R. J. Braun, "Dynamics of the tear film", Annu. Rev. Fluid Mech. **44**, 267–297 (2012).

[11] W. Nusselt, "Die Oberflächenkondensation des Wasserdampfes", VDI Z, 541–546 (1916).

[12] M. Scholle and N. Aksel, "An exact solution of visco-capillary flow in an inclined channel", ZAMP **52**, 749–769 (2001) 10.1007/PL00001572.

[13] A. Haas, T. Pollak, and N. Aksel, "Side wall effects in thin gravity-driven film flow – steady and draining flow", Phys. Fluids **23**, 062107 (2011) 10.1063/1.3604002.

[14] M. Scholle and N. Aksel, "Thin film limit and film rupture of the visco–capillary gravity–driven channel flow", Zeitschrift für angewandte Mathematik und Physik ZAMP **54**, 517–531 (2003) 10.1007/s00033-003-2090-z.

[15] C.-Y. Wang, "Liquid film flowing slowly down a wavy incline", AIChE Journal **27**, 207–212 (1981) 10.1002/aic.690270206.

[16] A. Wierschem, M. Scholle, and N. Aksel, "Vortices in film flow over strongly undulated bottom profiles at low Reynolds numbers", Phys. Fluids **15**, 426–435 (2003) 10.1063/1.1533075.

[17] M. Scholle, A. Wierschem, and N. Aksel, "Creeping films with vortices over strongly undulated bottoms", Acta Mech. **168**, 167–193 (2004) 10.1007/s00707-004-0083-4.

[18]P.-K. Nguyen and V. Bontozoglou, “Steady solutions of inertial film flow along strongly undulated substrates”, Physics of Fluids **23**, 052103 (2011) 10.1063/1.3591154.

[19]M. Scholle, A. Rund, and N. Aksel, “Drag reduction and improvement of material transport in creeping films”, Archive of Applied Mechanics **75**, 93–112 (2006) 10.1007/s00419-005-0414-5.

[20]A. Wierschem and N. Aksel, “Influence of inertia on eddies created in films creeping over strongly undulated substrates”, Phys. Fluids **16**, 4566–4574 (2004) 10.1063/1.1811673.

[21]M. Scholle, A. Haas, N. Aksel, M. C. T. Wilson, H. M. Thompson, and P. H. Gaskell, “Competing geometric and inertial effects on local flow structure in thick gravity-driven fluid films”, Phys. Fluids **20**, 123101 (2008) 10.1063/1.3041150.

[22]Y. Trifonov, “Viscous liquid film flows over a periodic surface”, Int. J. Multiphase Flow **24**, 1139–1161 (1999) https://doi.org/10.1016/S0301-9322(98)00022-6.

[23]A. Wierschem, T. Pollak, C. Heining, and N. Aksel, “Suppression of eddies in films over topography”, Phys. Fluids **22**, 113603 (2010) 10.1063/1.3504374.

[24]M. I. Pak and G. H. Hu, “Numerical investigations on vortical structures of viscous film flows along periodic rectangular corrugations”, Int. J. Multiphase Flow **37**, 369–379 (2011) 10.1016/j.ijmultiphaseflow.2010.12.001.

[25]V. Bontozoglou and G. Papapolymerou, “Laminar film flow down a wavy incline”, Int. J. Multiphase Flow **23**, 69–79 (1997) 10.1016/S0301-9322(96)00053-5.

[26]V. Bontozoglou, “Laminar film flow along a periodic wall”, Comput. Model. Eng. Sci., 133–142 (2000).

[27]A. Wierschem, V. Bontozoglou, C. Heining, H. Uecker, and N. Aksel, “Linear resonance in viscous films on inclined wavy planes”, Int. J. Multiphase Flow **34**, 580–589 (2008) 10.1016/j.ijmultiphaseflow.2007.12.001.

[28]C. Heining, V. Bontozoglou, N. Aksel, and A. Wierschem, “Nonlinear resonance in viscous films on inclined wavy planes”, Int. J. Multiphase Flow **35**, 78–90 (2009) 10.1016/j.ijmultiphaseflow.2008.07.005.

[29]A. Wierschem and N. Aksel, “Hydraulic jumps and standing waves in gravity-driven flows of viscous liquids in wavy open channels”, Phys. Fluids **16**, 3868–3877 (2004) 10.1063/1.1789431.

[30]P. L. Kapitza, “Wavy flow of thin layers of viscous liquid”, Zh. Eksper. Teoret. Fiz., 3–28 (1948).

[31]P. L. Kapitza and S. P. Kapitza, “Wavy flow of thin layers of a viscous fluid”, Zh. Eksp. Teor. Fiz., 105–120 (1949).

[32]T. B. Benjamin, “Wave formation in laminar flow down an inclined plane”, J. Fluid Mech. **2**, 554 (1957) 10.1017/S0022112057000373.

[33]C.-S. Yih, “Stability of Liquid Flow down an Inclined Plane”, Phys. Fluids **6**, 321 (1963) 10.1063/1.1706737.

[34]W. M. Orr, “The Stability or Instability of the Steady Motions of a Perfect Liquid and of a Viscous Liquid. Part II: A Viscous Liquid”, Proc. R. Ir. Acad. A Math. Phys. Sci. **27**, 69–138 (1907).

[35]W. M. Orr, "The Stability or Instability of the Steady Motions of a Perfect Liquid and of a Viscous Liquid. Part I: A Perfect Liquid", Proc. R. Ir. Acad. A Math. Phys. Sci. **27**, 9–68 (1907).

[36]A. Sommerfeld, "Ein Beitrag zur hydrodynamischen Erklarung der turbulenten Flussigkeisbewegung", Atti Congr. Int. Math. 4th **3**, 116–124 (1908).

[37]H.-h. Chang and E. A. Demekhin, *Complex wave dynamics on thin films*, Vol. 14 (Elsevier, 2002).

[38]J. Liu, J. D. Paul, and J. P. Gollub, "Measurements of the primary instabilities of film flows", J. Fluid Mech. **250**, 69–101 (1993) 10.1017/S0022112093001387.

[39]M. Vlachogiannis and V. Bontozoglou, "Experiments on laminar film flow along a periodic wall", J. Fluid Mech. **457**, 133–156 (2002) 10.1017/S0022112001007637.

[40]A. Wierschem and N. Aksel, "Instability of a liquid film flowing down an inclined wavy plane", Physica D **186**, 221–237 (2003) 10.1016/S0167-2789(03)00242-2.

[41]S. J. D. D'Alessio, J. P. Pascal, and H. A. Jasmine, "Instability in gravity-driven flow over uneven surfaces", Phys. Fluids **21**, 062105 (2009) 10.1063/1.3155521.

[42]C. Heining and N. Aksel, "Effects of inertia and surface tension on a power-law fluid flowing down a wavy incline", Int. J. Multiphase Flow **36**, 847–857 (2010) 10.1016/j.ijmultiphaseflow.2010.07.002.

[43]T. Pollak and N. Aksel, "Crucial flow stabilization and multiple instability branches of gravity-driven films over topography", Phys. Fluids **25**, 024103 (2013) 10.1063/1.4790434.

[44]M. Schörner, D. Reck, N. Aksel, and Y. Trifonov, "Switching between different types of stability isles in films over topographies", Acta Mech. **229**, 423–436 (2018) 10.1007/s00707-017-1979-0.

[45]M. Schörner, D. Reck, and N. Aksel, "Does the topography's specific shape matter in general for the stability of film flows?", Phys. Fluids **27**, 042103 (2015) 10.1063/1.4917026.

[46]M. Schörner, "The stability of gravity-driven viscous films over topography", PhD thesis (Universität Bayreuth, Bayreuth, 2018), 124 pp.

[47]N. Aksel and M. Schörner, "Films over topography: from creeping flow to linear stability, theory, and experiments, a review", Acta Mech. **229**, 1453–1482 (2018) 10.1007/s00707-018-2146-y.

[48]G. D. Fulford, "Gas liquid flow in an inclined channel", PhD thesis (University of Birmingham, Birmingham, 1962).

[49]G. D. Fulford, "The Flow of Liquids in Thin Films", in *Advances in Chemical Engineering*, Vol. 5, edited by T. B. Drew, J. W. Hoopes, T. Vermeulen, and G. R. Cokelet (Academic Press, Jan. 1, 1964), pp. 151–236, 10.1016/S0065-2377(08)60008-3.

[50]L. Hopf, "Hydrodynamische Untersuchungen: Turbulenz bei einem Flusse; Über Schiffswellen.", PhD thesis (München, 1910).

[51]M. Vlachogiannis, A. Samandas, V. Leontidis, and V. Bontozoglou, "Effect of channel width on the primary instability of inclined film flow", Phys. Fluids **22**, 012106 (2010) 10.1063/1.3294884.

[52]A. Georgantaki, J. Vatteville, M. Vlachogiannis, and V. Bontozoglou, "Measurements of liquid film flow as a function of fluid properties and channel width: Evidence for surface-tension-induced long-range transverse coherence", Phys. Rev. E **84**, 026325 (2011).

[53]T. Pollak, A. Haas, and N. Aksel, "Side wall effects on the instability of thin gravity-driven films — From long-wave to short-wave instability", Phys. Fluids **23**, 094110 (2011) 10.1063/1.3634042.

[54]J. P. Kuehner, J. D. Mitchell, and M. R. Lee, "Experimental investigation of gravity-driven film flow inside an inclined corrugated pipe", Physics of Fluids **31**, 122104 (2019) 10.1063/1.5125432.

[55]V. Leontidis, J. Vatteville, M. Vlachogiannis, N. Andritsos, and V. Bontozoglou, "Nominally two-dimensional waves in inclined film flow in channels of finite width", Phys. Fluids **22**, 112106 (2010) 10.1063/1.3484250.

[56]L. Schiller, "Die Entwicklung der laminaren Geschwindigkeitsverteilung und ihre Bedeutung für Zähigkeitsmessungen., (Mit einem Anhang über den Druckverlust turbulenter Strömung beim Eintritt in ein Rohr.)", Z. angew. Math. Mech. **2**, 96–106 (1922) 10.1002/zamm.19220020203.

[57]S. Lynn, "The acceleration of the surface of a falling film", AIChE Journal **6**, 703–705 (1960) 10.1002/aic.690060436.

[58]D. F. Bruley, "Predicting vertical film flow characteristics in the entrance region", AIChE Journal **11**, 945–950 (1965).

[59]R. Haugen, "Laminar flow along a vertical wall", Journal of Applied Mechanics **35**, 631–633 (1968).

[60]N. A. Hassan, "Laminar flow along a vertical wall", Journal of Applied Mechanics **34**, 535–537 (1967).

[61]R. L. Cerro and S. Whitaker, "Entrance region Bows with a free surface: the falling liquid film", Chemical Engineering Science **26**, 785–798 (1971).

[62]A. Kögel and N. Aksel, "Massive stabilization of gravity-driven film flows with corrugated side walls", Physics of Fluids **30**, 114105 (2018) 10.1063/1.5055931.

[63]A. Kögel and N. Aksel, "Stability of the channel flow—new phenomena in an old problem", Acta Mechanica **231**, 1063–1082 (2020) 10.1007/s00707-019-02568-8.

[64]C. Nalluri, R. E. Featherstone, and M. Marriott, *Nalluri & Featherstone's civil engineering hydraulics : essential theory with worked examples* (John Wiley & Sons, Chichester, West Sussex, U.K., 2009).

[65]J. H. Spurk and N. Aksel, *Fluid Mechanics*, 3rd ed. (Springer, Cham, 2020), 10.1007/978-3-030-30259-7.

[66]J. Happel and H. Brenner, *Low Reynolds number hydrodynamics: with special applications to particulate media*, Vol. 1 (Springer Science & Business Media, 2012).

[67]M. Raffel, C. E. Willert, F. Scarano, C. J. Kähler, S. T. Wereley, and J. Kompenhans, *Particle image velocimetry: a practical guide* (Springer, 2018).

[68]W. Thielicke and E. J. Stamhuis, "PIVlab – Towards User-friendly, Affordable and Accurate Digital Particle Image Velocimetry in MATLAB", Journal of Open Research Software **2**, e30 (2014) http://doi.org/10.5334/jors.bl.

[69]W. Thielicke and E. J. Stamhuis, *PIVlab - Time-Resolved Digital Particle Image Velocimetry Tool for MATLAB*, version 1.50.

[70]J. C. Crocker and D. G. Grier, "Methods of Digital Video Microscopy for Colloidal Studies", J. Colloid Interface Sci. **179**, 298–310 (1996) 10.1006/jcis.1996.0217.

[71]D. Allan, T. Caswell, N. Keim, and C. van der Wel, "trackpy: Trackpy v0.3.2", Zenodo, 10.5281/zenodo.60550 (2016) 10.5281/zenodo.60550.

[72]F. E. Grubbs, "Sample Criteria for Testing Outlying Observations", Ann. Math. Statist. **21**, 27–58 (1950) 10.1214/aoms/1177729885.

[73]A. Wierschem, C. Lepski, and N. Aksel, "Effect of long undulated bottoms on thin gravity-driven films", Acta Mech. **179**, 41–66 (2005) 10.1007/s00707-005-0242-2.

[74]M. Schörner, D. Reck, and N. Aksel, "Stability phenomena far beyond the Nusselt flow – Revealed by experimental asymptotics", Phys. Fluids **28**, 022102 (2016) 10.1063/1.4941000.

[75]M. Dauth, M. Schörner, and N. Aksel, "What makes the free surface waves over topographies convex or concave? A study with Fourier analysis and particle tracking", Phys. Fluids **29**, 092108 (2017) 10.1063/1.5003574.

[76]M. Dauth and N. Aksel, "Transition of regular wave fronts to irregular wave fronts in gravity-driven thin films over topography", Acta Mechanica **230**, 2475–2490 (2019) 10.1007/s00707-019-02417-8.

Journal publications

- Kögel, A. and Aksel, N.:
"Stability of the Channel Flow—New Phenomena in an Old Problem"
Acta Mechanica **231**(3), 1063-1082 (2020). doi: 10.1007/s00707-019-02568-8

- Kögel, A. and Aksel, N.:
"Massive stabilization of gravity-driven film flows with corrugated side walls,"
Physics of Fluids **30**(11) 114105 (2018). doi: 10.1063/1.5055931

Danksagungen

Ich bedanke mich bei allen Mitarbeitern des Lehrstuhls für Technische Mechanik und Strömungsmechanik der Universität Bayreuth, die mich während meiner Promotion begleitet und tatkräftig unterstützt haben. Mein besonderer Dank gilt Professor Dr. Nuri Aksel für seine hervorragende Betreuung. Er nahm sich stets Zeit für fruchtbringende Diskussionen und sorgte dadurch für ein rasches Vorankommen, ließ mir aber auch alle wissenschaftlichen Freiheiten, um meine eigenen Forschungsschwerpunkte zu setzten. Ich möchte mich auch bei den anderen Mitgliedern des Lehrstuhls bedanken, bei Dr. Lutz Heymann, Mario Schörner und Markus Dauth für die vielen konstruktiven Gespräche und Vorschläge, besonders aber bei Marion Märkl, Stephan Eißner und Gabriele Jena für die Unterstützung im experimentellen Bereich und für die Durchführung der Messungen. Bei Mario Linz möchte ich mich zusätzlich für die wissenschaftlichen Erkenntnisse im Rahmen seiner Masterarbeit bedanken, die mir auch bei der Erstellung dieser Dissertation geholfen haben. Zudem bedanke ich mich bei Katja Helmrich und Christa Reimer für ihre Unterstützung in organisatorischen Angelegenheiten. Ich möchte mich darüber hinaus bei Professor Dr. Sesterhenn dafür bedanken, dass er mir die Fertigstellung der Dissertation am Lehrstuhl ermöglicht hat.

Bedanken möchte ich mich auch bei meinen Korrekturlesern Tino Franz, Manuel Eisentraut und Adal Sabri, die dieser Dissertation noch den Feinschliff gegeben haben.

Zum Schluss möchte ich mich bei meiner Frau Maria für ihre uneingeschränkte Unterstützung und ihr Verständnis während der letzten Jahre bedanken.

Selbstständigkeitserklärung

Hiermit versichere ich, dass ich die vorliegende Dissertation selbstständig verfasst und keine anderen als die von mir angegebenen Quellen und Hilfsmittel verwendet habe.

Ich erkläre, dass ich diese Dissertation nicht bereits zur Erlangung eines akademischen Grades eingereicht habe und dass ich nicht bereits diese oder eine gleichartige Doktorprüfung endgültig nicht bestanden habe.

Des Weiteren erkläre ich, dass ein gewerblicher Promotionsberater bzw. Promotionsvermittler weder bisher in Anspruch genommen wurde noch künftig in Anspruch genommen wird.

(Ort, Datum)	(Armin Kögel, M.Sc.)